UNIVERSITY OF ZULULAND

A Thesis presented in fulfillment of the requirement for the degree of

Doctor of Philosophy in Physics

in

University of Zululand

Comparative Study of Rare- Earth based Ferrites for Flammable and Volatile Organic Compound Gas Sensors

FACULTY OF SCIENCE AND AGRICULTURE

Candidate: Prince S'busiso Mkwae

Student number: 20022728

Supervisor: Dr S.S. Nkosi (University of Limpopo)

Co Supervisor: Dr C.L. Ndlangamandla (University of Zululand)

Date of submission

NOVEMBER 2023

DECLARATION

I, the undersigned, hereby declare that the work contained in this dissertation is my own original work and that I have not previously in its entirety or in part submitted it at any university for a degree.

Signature: ……

Date: ……

Dedicated to my late friends and family

My Father Steven Mbolwane Mkwae

Father- in- Law Vusimuzi Jaftha Mhlophe

My friend Philani T. Abel Gumede

Bheki Boya Myeni

My Cousin Nicho Mhlanga

May your souls rest in eternal peace

You are forever missed

- My first Thanks goes to the Almighty and my ancestors for giving me strength and protecting me all these years of my life.
- Dr Nkosi for his supervision, guidance, sleepless nights when doing measurements, his assistance in analysing and presentations of results.
- Dr Ndlangamandla for his supervision, organising presentations, application of ethical clearance and being there for me when I need him the most.
- Dr Ioannis Kortidis for his sleepless nights during gas sensing measurements, literature reviews search, analysis, and his guidance. Thank you Mlungu.
- The late Prof O.M Ndwandwe may your soul rest in peace Zwide….uyidlalile indima ezimpilweni zethu Ongoye.
- Prof Jili for being a good HOD to me, always encouraging junior staff to complete their degrees. Thanks, Mphephethwa
- Mr CT Thethwayo you are everything mfethu uqhubeke njalo.
- My wife Nosipho for being a smile keeper, advisor, encourager and for pushing me throughout this work. Uyathandwa Zindela.
- Prof SS Ntshangase for his assistance throughout this study and being a good example in life.
- Dr Mbatha for his friendship and encouragement.
- Mr Khoza for his friendship, encouragement, and care. Thank you, my friend you are always there, when I need you.
- Sis Futhi (Mrs Mothapo) for her kind heart and ever smiling reception.

LIST OF PUBLICATIONS AND CONFERENCES DERIVED FROM THIS THESIS

PUBLICATIONS: H-index 4 (62 Citations – Google Scholar) – 10/2023

1. **Mkwae, P.S**., Kortidis, I., Kroon, R.E., Leshabane, N., Jozela, M., Swart, H.C. and Nkosi, S.S., **2020**. Insightful acetone gas sensing behaviour of Ce substituted $MgFe_2O_4$ spinel nano-ferrites. **Journal of Materials Research and Technology, 9(6), pp.16252-16269.**
2. **Mkwae, P.S**., Ogundipe, S.A., Jozela, M., Revaprasadu, N. and Nkosi, S.S., **2022**. The heat rate kinetics on the liquefied hydrocarbon gases sensing and food quality control detecting strategy. **Materials Chemistry and Physics, 277, p.125550.**
3. Sifiso W. Gumbi, **Prince S. Mkwae**, Ioannis Kortidis, Robin E. Kroon, Hendrik C. Swart, Thomas Moyo, Steven S. Nkosi. Electronic and Simple Oscillatory Conduction in Ferrite Gas Sensors: Gas-Sensing Mechanisms, Long-Term Gas Monitoring, Heat Transfer, and Other Anomalies. **ACS Appl. Mater. Interfaces** 12, 38, (2020) 43231-43249.
4. Nolwazi N. Shozi, Ioannis Kortidis, **Prince S. Mkwae**, Nelisiwe P. Chonco, Nompumelelo Leshabane, Mudalo Jozela, Robin E. Kroon, Hendrik C. Swart, Steven S. Nkosi. Extremely sensitive and selective flammable liquefied hydrocarbon gas sensing and inter-dependence of fluctuating operating temperature and resistance: Perspective of rare-earth doped cobalt nanoferrites. **Journal of Alloys and Compounds** 859 (2021) 157846
5. Steven S. Nkosi, **Prince S. Mkwae**, Sunday A. Ogundipe, Nompumelelo Leshabane, Neerish Revaprasadu, R.E. Kroon. Abnormal p-type to n-type switching during nitric

oxide gas sensing: Ni $(OH)_2$ nanoplatelets on amorphous NiO seed layers. **Vacuum** 200 (2022) 111032.

6. Mpanza, T., Ndlangamandla, C.L., Ngom, B.D., Nkosi, S.S., Jili, T.P., Thethwayo, C.T., Biyela, P.N., Cebekhulu, N.G., **Mkwae, P.S**. and Ogundipe, S.A., 2023. Tungsten oxide thin film for room temperature nitrogen dioxide gas sensing. In MATEC Web of Conferences (Vol. 374, p. 01003). EDP Sciences.

CONFERENCES CONTRIBUTION

1. **PS Mkwae**, ON Ngubelanga, SS Nkosi, CL Ndlangamandla, Gas sensing properties of rare-earth substituted $MgFe_2O_4$ ferrite nanoparticles, **67th annual South African Institute of Physics conference held at the University of Zululand, Richards Bay, 03 – 07 July (2023)**

The monitoring of flammables and VOCs is still a challenge. In addition, acetone (CH_3CH_3CO) is a one of the toxic and harmful volatile organic compounds (VOCs) commonly used as a solvent in various laboratories and industries. Its high level of inhalation and ingestion can cause low, acute and chronic poisoning. Another commonly used highly flammable gas is liquefied petroleum gas (LPG), commonly known as a cooking gas, which is widely available in almost all communities and working environments to create fires for various uses. This gas causes many fatalities due to its nature of complexities in detection and can easily ignite. This, therefore, suggests that it is one of the main air pollutants that require constant detection and monitoring. Most studies in the chemical gas sensing community focus on just the normal sensing of these gases. In an attempt to solve the long existing problem, we have undertaken this study, where $MgCe_xFe_{2-x}O_4$ ($0 \leq x \leq 0.4$) nanoparticles have been produced by the glyco-thermal technique and characterised by X-ray diffraction, electron microscopy, X-ray photoelectron spectroscopy, Mössbauer spectroscopy and gas sensing analyses. The X-ray diffraction results indicated that a pure cubic spinel phase was formed for samples having a low concentration of Ce, but the high Ce doping ($x \geq 0.2$) of magnesium ferrite resulted in the formation of secondary phases. The crystallite size of the compounds ranged from 2.2 nm to 15.3 nm. The ^{57}Fe Mössbauer spectra showed transformation from an ordered to a paramagnetic spin state with an increase in Ce concentration. Gas sensors fabricated from the spinel ferrites were tested towards various organic compound vapours (acetone, methanol, p-xylene, ethylbenzene, toluene, and benzene) and flammable gases (LPG, Methane, Propane, Butane and Ammonia) at an operating temperature of 225 °C. The $MgCe_{0.2}Fe_{1.8}O_4$ nanoferrites proved to possess quality sensor characteristics of high sensitivity and selectivity to acetone vapour, with a response of over 500@100 ppm concentration as well as reproducibility, reversibility, and stability of over 120 days. This sensor not only displayed high responses, but

could also maintain them over 1, 3, 5, 10, 20, and 30 min of acetone exposure time. On flammable gases, the addition of cerium to magnesium ferrites proved to kill the sensing. The best performing sensor was found to be the undoped Magnesium ferrite on LPG gas. It was resilient and sensitive to an oxygen reduced, inert ambient environment. Under relative humidity, the response was reduced, but stable, due to physisorbed water molecules. In addition, this SMO sensor was tested at 200 ˚C on vegetables and fruit to evaluate their off-shelf freshness during the ripening process. These plants show a dramatic increase in the respiration rate over their maturation or ripening process over time.

Ukuqapha izinto ezivuthayo kanye nama-VOC kuseyinselelo. Ngaphezu kwalokho, i-acetone (CH_3CH_3CO) ingenye yezinhlanganisela eziphilayo ezinobuthi neziyingozi (VOCs) ezivame ukusetshenziswa njengesinyibilikisi kumalabhorethri nezimboni ezihlukahlukene. Izinga layo eliphezulu lokuhogela kanye nokumunca lingabangela ubuthi obuphansi, obunamandla futhi obungapheli. Enye igesi evame ukuvutha esetshenziswa kakhulu i-liquefied petroleum gas (LPG), eyaziwa ngokuthi igesi yokupheka, etholakala cishe kuyo yonke imiphakathi nasezindaweni zokusebenza ukuze kubase imililo esetshenziselwa ukusetshenziswa okuhlukahlukene. Le gesi idala ukufa kwabantu abaningi ngenxa yemvelo yayo yobunzima ekubonweni futhi ingavutha kalula. Ngakho-ke, lokhu kuphakamisa ukuthi ingenye yezinto ezingcolisa umoya ezidinga ukubonwa nokuqapha njalo. Ucwaningo oluningi emphakathini ozwa igesi yamakhemikhali lugxile ekuzwaneni nje okujwayelekile kwala magesi. Emzamweni wokuxazulula inkinga ende ekhona, senze lolu cwaningo, lapho i-$MgCe_xFe_{2-x}O_4$ ($0 \leq x \leq 0.4$) nanoparticles ikhiqizwe indlela ye-glyco-thermal futhi ibonakala nge-X-ray diffraction, i-electron microscopy, i-X-ray photoelectron spectroscopy, i-Mössbauer spectroscopy kanye nokuhlaziywa kokuzwa kwegesi. Imiphumela ye-X-ray diffraction ibonise ukuthi isigaba se-cubic spinel esihlanzekile sakhiwe amasampula ane-concentration ephansi ye-Ce, kodwa i-Ce doping ephezulu ($x \geq 0.2$) ye-magnesium ferrite ibangele ukwakheka kwezigaba zesibili. Ubukhulu be-crystallite bezinhlanganisela busukela ku-2.2 nm kuya ku-15.3 nm. I-spectra ye-^{57}Fe Mössbauer ibonise ukuguqulwa ukusuka ku-oda ukuya esimweni sokujikeleza kwe-paramagnetic kanye nokwenyuka kokugxila kwe-Ce. Izinzwa zegesi ezakhiwe ngama-spinel ferrites zahlolelwa ukushunqa inhlabathi ehlukahlukene (i-acetone, i-methanol, i-p-xylene, i-ethylbenzene, i-toluene, ne-benzene) namagesi avuthayo (LPG, Methane, Propane, Butane kanye ne-ammonia) ezingeni lokushisa elingu-225°C. I-$MgCe_{0.2}Fe_{1.8}O_4$ nanoferrites ibonakale inezici zezinzwa zekhwalithi zokuzwela okuphezulu nokukhetha kumhwamuko we-acetone, nempendulo yokugxila okungaphezu kuka-500@100

ppm kanye nokuphindaphindeka, ukuhlehla, nokuzinza kwezinsuku ezingaphezu kweziyi-120. Le nzwa ayizange ibonise ukusabela okuphezulu kuphela, kodwa futhi ibikwazi ukuzigcina ngaphezu kwe-1, 3, 5, 10, 20, kanye nemizuzu engama-30 yesikhathi sokuchayeka kwe-acetone. Kumagesi avuthayo, ukungezwa kwe-cerium kuma-magnesium ferrites kufakazele ukubulala inzwa. Inzwa esebenza kahle kakhulu itholwe iyi-Magnesium ferrite engafakwanga i cerium kugesi ye-LPG. Yayikwazi ukumelana nezimo futhi izwela umoya-mpilo oncishisiwe, indawo ezungezile engenzi lutho. Ngaphansi komswakama ohlobene, impendulo yancishiswa, kodwa yazinza, ngenxa yama-molecule amanzi afakwe i-physisorbed. Ukwengeza, le nzwa ye-SMO ihlolwe ku-200 ˚C ezitshalweni nasezithelweni ukuze kuhlolwe ubusha bazo obungekho eshalofini ngesikhathi sokuvuthwa. Lezi zitshalo zibonisa ukwanda okumangalisayo kwezinga lokuphefumula phezu kokuvuthwa kwazo noma inqubo yokuvuthwa ngokuhamba kwesikhathi.

a - Lattice parameter

BET- Brunauer-Emmet-Teller

Ce - Cerium

CH_3CH_3CO – Acetone

D- Crystalline size

Fe - Iron

HRTEM- High resolution transmission electron microscopy

IoT- Internet of Things

LPG - Liquified Petroleum Gas

Mg - Magnesium

PL- Photoluminescence

RH- Relative Humidity

SEM- Scanning electron microscopy

SMO- Semiconductor Metal Oxide

ß – Time delay

V - Volume

VOC- Volatile organic compound

VSM - Vibrating Sample Magnetometer

XPS- X-ray photoelectron spectroscopy

XRD- X-ray diffraction

ρ - Density

TABLE OF CONTENTS

LIST OF FIGURES

LIST OF TABLES

CHAPTER 1

INTRODUCTION OF THE STUDY

1.1 INTRODUCTION

The world has entered the fourth industrial revolution (4IR), therefore all sectors of technology are preparing and transforming themselves for this era. Nanotechnology has a crucial role to play during this transformation. Nanotechnology allows the extensive understanding of the unusual physical and chemical properties of matter at the nanometre scale, revealing a variety of possible applications in different fields such as materials science, engineering, physics, chemistry and biology **[1]**. Researchers across the globe have embarked on studying these nanomaterials to improve existing technologies, and for the development of new commercial products and devices. Nanomaterials of ferrites and semiconducting metal oxides are amongst the materials studied because of their applications in various sectors such as ceramic materials, photonics, solar cells, window coating, catalytics, drug delivery and sensors **[2]**. However, in this study we look at the gas sensing application of these materials. Semiconducting metal oxides based gas sensors are widely used in industries, mines, laboratories, and households to detect poisonous or flammable gases. Nowadays spinel ferrites are studied for different gas sensor applications. Despite their wide usage, the current commercial gas sensors suffer from several limitations such as high power consumption, high working temperature and low sensitivity **[3, 4]**. The cheap, reliable, small, and low power-consuming gas sensors are in great demand.

1.2 MOTIVATION

The monitoring of flammables and VOCs is still a challenge, including the current available techniques of breath analysis, require analytical instruments which are only available in

laboratories, and are cumbersome and expensive. In addition, acetone (CH_3CH_3CO) is a toxic and harmful volatile organic compound (VOC) commonly used as a solvent in various laboratories and industries. Its high level of inhalation and ingestion can cause low acute and chronic poisoning **[5, 6]**. Another commonly used highly flammable gas is liquefied petroleum gas (LPG), commonly known as cooking gas. This gas is widely available in almost all communities and working environments to create fires for various uses. This gas causes many fatalities due to its nature of complexities in detection and its high flammability, which suggests that it is one of the main air polluters that requires constant monitoring and detection **[5-7]**. Most studies in the chemical gas sensing community focus on just the normal sensing of these gases. The monitoring part remains neglected, possibly due to the lack of stable sensors capable of detecting over a long period. In an attempt to solve the long existing problem, we have undertaken this study. Magnesium doped with Cerium was synthesised and tested against various gases at different temperatures. These complex and smart semiconducting ferrites seem to solve the problem of short lifespan, low sensitivity, high working temperature and, finally, are shown to be more sensitive to acetone and LPG.

1.3 OBJECTIVE OF THE STUDY

This study focuses on the fabrication of gas sensors from the smart and novel materials of cerium doped magnesium ferrites capable for the detection and monitoring of the flammables, volatile organic compounds, and the benzene derivatives isomers for potential use in clinical applications in the health sector. Furthermore, this study seeks to push the frontiers of fundamental chemical gas sensing mechanisms by conducting normal sensing in an inert ambient environment.

The objectives include:

- To synthesis of $MgCe_xFe_{2-x}O_4$ ($0 \leq x \leq 0.4$) normal spinels.
- To investigate the structural, morphological, and optical characterisations of $MgCe_xFe_{2-x}O_4$ nano ferrites.

- To conduct detailed gas sensing measurements and analyses of these $MgCe_xFe_{2-x}O_4$ nano ferrites.
- To test for possible use in food quality and health applications.

1.4 THESIS ORGANISATION

Chapter one presents the introduction, motivation and the objectives of the study while chapter two focusses on the history of metal oxide based gas sensors and their characteristics. It also presents the sensing mechanism related to ferrites, important parameters of metal oxide-based gas sensors, properties of Magnesium ferrite such as structure and morphology and their effect on gas sensing properties.

Chapter three is devoted to the full description of the synthesis methods used to synthesise cerium-doped magnesium ferrites. The characterisation techniques used for the investigation of the structural, morphological, optical and gas sensing properties are also presented in detail in this chapter. The results from all the characterisation techniques are discussed extensively in chapter four, while chapter five is dedicated to gas sensing properties of the $MgCe_xFe_{2-x}O_4$ nanoferrites with various Ce substitution ($x = 0, 0.05, 0.1, \& 0.2$) in the octahedral Fe-site which were evaluated in terms of the sensors' current ratios (response/sensitiveness) to various volatile organic compounds (VOCs) and flammable gases. Chapter Six explores the possible application of Magnesium-Cerium doped nanoferrites in health and food industries, while chapter seven presents the conclusions and recommendations for future work.

1.5 REFERENCES

[1] S. Singh, B.C. Yadav, M. Singh, R. Kothari, A review Report on Nanostructured Ferrites as Liquefied Petroleum Gas Sensor, International Journal of Science, Technology & Society 1 (2015). 5-22

[2] H.-L. Chen, Y.-M. Lu, W.-S. Hwang, Characterization of sputtered NiO thin films, Surface and Coatings Technology 198 (2005) 138-142.

[3] A. Qureshi, A. Mergen, A. Altindal, Preparation and characterization of Li and Ti codoped NiO nanocomposites for gas sensors applications, Sensors and Actuators B: Chemical 135 (2009) 537-540.

[4] A.M. Soleimanpour, Y. Hou, A.H. Jayatissa, The effect of UV irradiation on nanocrysatlline zinc oxide thin films related to gas sensing characteristics, Applied Surface Science 257 (2011) 5398-5402.

[5] A. Mirzaei, S.G. Leonardi, G. Neri, Detection of hazardous volatile organic compounds (VOCs) by metal oxide nanostructures-based gas sensors., Ceramic International 42 (2016) 15119-15141.

[6] N. Tammanoon, A. Wisitsoraat, D. Phokharatkul, A. Tuantranont, S. Phanichphant, V. Yordsri, C. Liewhiran, Highly sensitive acetone sensors based on flame-spray-made La2O3-doped SnO2 nanoparticulate thick films, Sensors and Actuators B: Chemical 262 (2018) 245-262.

[7] Run Zhang, Yan Wang, Zhanying Zhang, J. Cao, Highly Sensitive Acetone Gas Sensor Based on g-C3N4 Decorated MgFe2O4 Porous Microspheres Composites., Sensors 18 (2018).2211

CHAPTER 2

BACKGROUND AND LITERATURE REVIEW OF GAS SENSORS

2.1 INTRODUCTION

Gas sensors are devices designed to detect and measure the presence and concentration of various gases in the surrounding environment. They play a crucial role in a wide range of applications, including industrial processes, environmental monitoring, and safety systems. Gas sensors are employed to identify the presence of toxic or combustible gases, monitor air quality, and enable early detection of gas leaks. The detection and monitoring remain extremely important for health and safety working and living conditions**[1-5]**. Advances in gas sensor technology continue to improve their accuracy, selectivity, response time, and efficiency. However, research focuses on developing new materials, enhancing sensor performance, and integrating sensors into smart systems for real-time monitoring and control is on-going **[6-8].** Gas sensors utilise different technologies and principles to detect and quantify gases. There are five common types of gas sensors, i.e. electrochemical, catalytic, infrared, photoionization detectors and semiconductor sensors.

Electrochemical sensors are those which operate based on the principle of a chemical reaction between the target gas and electrodes. The resulting current is proportional to the detected gas concentration, allowing for accurate measurement**[9]** . Catalytic sensors detect combustible gases by utilising a heated catalyst. The presence of combustible gases causes oxidation on the catalyst's surface, resulting in a change in temperature that is measured to determine gas concentration**[10]**. Infrared (IR) sensors measure the absorption of infrared radiation by the

target gas. Each gas has a unique absorption spectrum, enabling the identification and quantification of specific gases**[11]**. Photoionization Detectors (PID)se ultraviolet light to ionize gas molecules, creating a detectable current that indicates the presence and concentration of gases**[12],** while the Semiconductor gas sensors rely on changes in electrical conductivity when exposed to specific gases. The resistance of the sensor varies with gas concentration, providing a measurable signal**[13-15]**.

Gas sensors can detect a wide range of gases, including carbon monoxide (CO), carbon dioxide (CO_2), methane (CH_4), oxygen (O_2), volatile organic compounds (VOCs), ammonia (NH3), nitrogen dioxide (NO_2), sulfur dioxide (SO_2), Liquified Petroleum Gas (LPG) and many others**[16-20]**. Different sensors are designed to be selective to specific gases based on their operating principles and materials used. In this work our focus is on Semiconducting metal oxide-based gas sensors. Semiconducting oxide-based gas sensors provide a cost-effective and reliable solution for gas monitoring and detection in various applications. Their simplicity, low power consumption, and compatibility with efficiency make them suitable for integration into portable devices and Internet of Things (IoT) systems, enabling pervasive gas control and monitoring **[21-23]**.

The following section elaborates on Semiconducting metal oxide (SMO) gas sensors, and basic properties of magnesium ferrites and their dopants, the factors that are essential for gas detection, particularly when utilising ferrites sensors. The optimum parameters of various metal ferrites used as sensors for different gases are also discussed.

2.2 SEMICONDUCTING METAL OXIDE (SMO) GAS SENSORS

Semiconducting metal oxide gas sensors have a rich history that spans several decades. The development and understanding of these sensors started back in the early 1950s. Brattain and Bardeen, two Bell Labs scientists, were the first to demonstrate that the conductivity of some semiconductor materials, such as Ge, would change regularly due to the adsorption and desorption behaviour of gases at their surface. The change in conductivity is caused by the

adsorbed gas's reversible doping of the surface**[24]**. In 1962 Seiyama et al**[25]**, successfully prepared a gas sensing device based on ZnO thin film which was able to detect various gases at 485 °C. The sensitivity of ZnO films to propane was substantially higher than that of thermal conductivity detectors during the period when gas detection was mostly done with them.

Advances in sensing materials (1960s-1990s): Researchers explored various other metal oxides, including zinc oxide (ZnO), tin dioxide (SnO_2), tungsten oxide (WO_3), and titanium dioxide (TiO_2), as potential sensing materials**[26-29]**. These materials showed enhanced sensitivity and selectivity to different target gases**[30, 31]**. The understanding of gas-surface interactions and surface chemistry played a crucial role in improving sensor performance during this period. In the early 2000s nanotechnology and thin films came to the party**[32, 33]**. The advent of nanotechnology facilitated the development of thin film gas sensors with improved performance. Nanoscale metal oxide materials were synthesised, and techniques like chemical vapor deposition (CVD) and sputtering were used to deposit thin films on substrates. This allowed for increased surface area, better gas adsorption, and faster response times.**[34, 35]**. The research continued in the 2010s with a focus on functionalization and selective sensing. Researchers focused on enhancing the selectivity of semiconducting metal oxide gas sensors by functionalizing the sensing materials**[36-38]**. By introducing dopants or modifying the surface with catalysts or nanomaterials, the sensors became capable of detecting specific gases with high sensitivity while minimising cross-sensitivity to other gases**[39, 40]**.

Recent advances are on biomarkers, and flexible and wearable gas sensors. Currently there is a growing interest in developing flexible and wearable gas sensors using semiconducting metal oxides**[41-45]**. These sensors can be integrated into textiles or wearable devices, enabling real-time monitoring of environmental or physiological gases. They offer potential applications in healthcare, environmental monitoring, and personal safety. Throughout their history, semiconducting metal oxide gas sensors have undergone continuous improvement in terms of sensitivity, selectivity, stability, and response time. The combination of advances in materials

science, nanotechnology, surface engineering and other fields has contributed to the significant progress and diversification of gas sensing technologies using semiconducting metal oxides. There are many metal oxides that have been used as gas sensing materials to sense different gases. The most common used materials are shown in the figure below **(Fig. 2.1)**

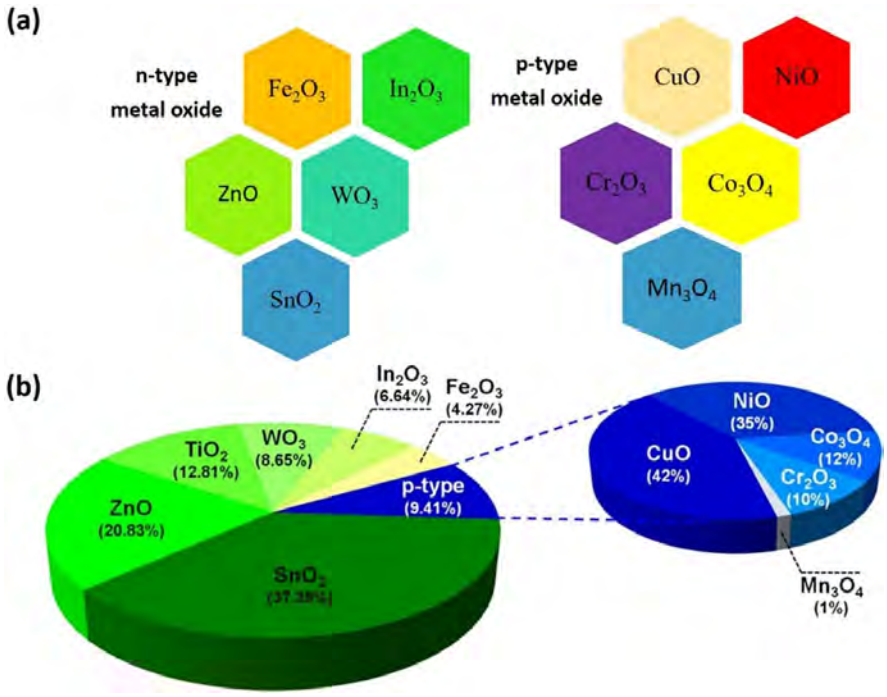

Figure 2. 1: (a) Classification of metal oxide as n-type and p-type based on their conductivity in chemical sensors; (b) shows results of a search study on metal oxide semiconductors commonly used as sensing materials for chemoresistive gas sensors. Adapted from Nurazz at al.**[46]**

Gas sensing materials can be classified as n-type or p-type depending on their majority charge carrier. (This is described in detail in the section on sensing mechanisms). From fig 2.1 it can be seen that about 90% of sensors are n-type and have been explored due to their unique properties and sensitivity to specific gases.

Tin Oxide (SnO_2): Tin oxide is one of the most popular metal oxide materials for gas sensing. It is particularly sensitive to reducing gases such as carbon monoxide (CO), methane (CH_4), and volatile organic compounds (VOCs)**[47, 48]**. Tin oxide-based gas sensors are widely used in industrial safety systems and air quality monitoring devices.

Titanium Dioxide (TiO_2): Titanium dioxide is another metal oxide used in gas sensing applications. It exhibits high sensitivity to gases like hydrogen (H_2) and nitrogen dioxide (NO_2)**[49, 50]**. TiO_2-based gas sensors find applications in automotive exhaust monitoring, environmental monitoring, and industrial safety.

Zinc Oxide (ZnO): Zinc oxide is a versatile metal oxide known for its excellent gas sensing properties. It can detect a wide range of gases, including carbon monoxide (CO), hydrogen (H2), and various volatile organic compounds (VOCs)**[51-53]**. ZnO-based gas sensors are employed in environmental monitoring, industrial process control, and as domestic gas leak detectors.

Tungsten Oxide (WO_3): Tungsten oxide is sensitive to gases such as hydrogen sulphide (H_2S), nitrogen oxides (NOx), and ozone (O_3)**[54-56]**. It finds applications in monitoring air quality, detecting toxic gases, and controlling industrial emissions.

Ferrite/Iron Oxide (Fe_2O_3): Iron oxide is commonly used in gas sensors for detecting carbon monoxide (CO), nitrogen dioxide (NO_2), and methane (CH_4)**[57]**. It is utilised in gas leak detectors, automotive exhaust monitoring, and indoor air quality systems.

Some metal oxide gas sensors still have drawbacks, such as long response times, poor selectivity, and short-term stability, which can be further reduced while operating in critical conditions, thereby limiting their practical application**[58-60]**. Spinel type oxides are one of the metal oxide sensors which have been studied **[62].** They have been studied widely for the detection of oxidizing as well as reducing gases depending upon the type of conductivity possessed by the material. Ferrites' suitability as gas sensors comes with their capability to fine tune their electrical properties**[61-63]**. In addition, ferrites have oxygen vacancies in their structure which modify the conduction properties and enhance the electrical response of the sensor**[61, 64]**. Other advantages of spinel ferrite in comparison with other sensor material involving single metal oxide semiconductors is their ability to adjust the type of conductivity

and resistance value by changing the positive ions' position, and that a variety of transition metal cations can be incorporated in the lattice of the parent magnetite structure.

2.2 SPINEL CRYSTALLINE STRUCTURE

Spinel ferrites normally crystallising as face centred cubic with eight tetrahedral and four octahedral sites per formula unit. The tetrahedral spaces are smaller than the octahedral spaces. B ions occupy half the octahedral holes, while A ions occupy one-eighth of the tetrahedral holes. They can be categorised as normal spinel and inverse spinel ferrites. The distribution of the divalent and trivalent metals among the coordinated oxygen is one of the most important factors determining whether the spinel ferrite is characterised as a normal or inverse spinel ferrite **[65-67]**. **Fig. 2. 2** shows the unit cell of spinel ferrite crystal structure.

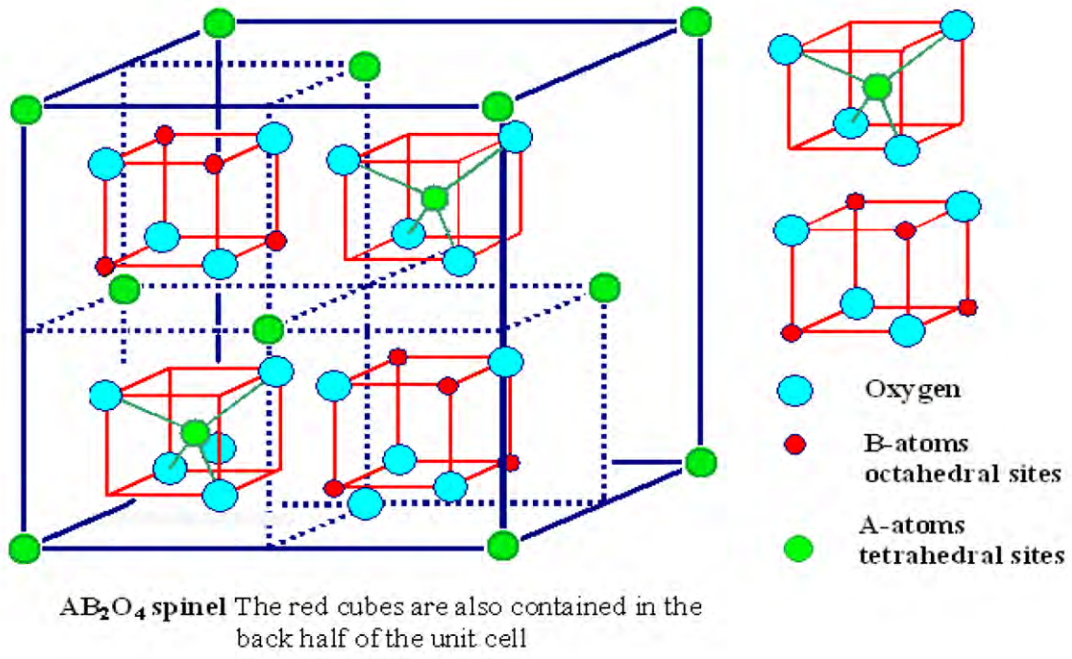

Figure 2. 2: Spinel Ferrite unit cell **[68]**. Source?

(a) Normal Spinel structure

In the Normal spinel the divalent A^{+2} ions occupy the tetrahedral sites, whereas the trivalent B^{+3} ions occupy the octahedral sites in the close packed arrangement of oxide ions**[69].** A normal spinel can be represented as follows: $(A^{+2})^{tet}(B^{+3})_2{}^{oct}O_4$. Examples of normal spinel structures are Mn_3O_4, $ZnFe_2O_4$, FeCr, $MgFe_2O_4$ etc.

(b) Inverse Spinel Structure

In an inverse spinel structure, the A^{+2} ions occupy the octahedral sites, whereas half of B^{+3} ions occupy the tetrahedral sites**[70]**. It can be represented as: $(B^{+3})^{tet}(A^{+2}B^{+3})^{oct}O_4$ E.g. Fe_3O_4 (ferrite), $CoFe_2O_4$, $NiFe_2O_4$ etc.

Recently, different kinds of ferrites have shown themselves to be good materials for semiconductor gas sensors **[71]**. For instance, the sensor based on the pure $NiFe_2O_4$ nanomaterial showed selective response towards 200 ppm of LPG at 400 °C operating temperature with a response time of few seconds and good reproducibility**[72]**. Zhang et al. **[3]** reported high acetone sensing with sensitivity (electrical current ratios) of 270.14 towards 500 ppm of acetone at 320 °C using $MgFe_2O_4$ decorated with g-C_3N_4. Meanwhile, $YbFeO_3$ doped with Ca recorded an improving acetone sensing in the presence of relative humidity up to 90 %RH at 230 °C. Their sensitivities were low, below 2 towards 100 ppb **[73]**. Another n-type $ZnFe_2O_4$ ferrite showed a sensitivity response of less than 3 towards 500 ppm of acetone at 200 °C. Bismuth based ferrite recorded an acetone response sensitivity of 1.8 towards 1 ppm at 350 °C **[74].** Ghadage at al **[75]** developed Pd loaded bismuth ferrite which showed good selectivity towards acetone, whose response was 69% at 300 °C operating temperature for 500 ppm gas concentration. By tuning the surface area and catalytic behaviour using CTAB and Pd loading, respectively, they were able to achieved a response of 95% with the response and recovery time of 75 s and 104 s. Tai et al. **[76]** published an interesting review article summarising the evolution of breath analysis on emerging wearable electronics. These wearable emerging technologies should be able to detect sensitively humidity under various subjected conditions such as excellent mechanical flexibility, low power consumption and multifunctionality. The highly humidified human breath (89-97% RH) contains a variety of gases such as nitrogen, oxygen, carbon dioxide, inert gases, and traces of biomarkers. These biomarkers are indicative of disease For example, exhaled biomarkers corresponding to certain diseases of some organs are ammonia for renal disease, hydrogen sulphide for halitosis, acetone for diabetes, pentane for heart disease, and toluene for lung cancer and helicobacter pylori **[76-**

79]. One of the well-known and utilised systems is the breath measurements for real-time ethanol monitoring for identifying driving under the influence of alcohol **[77]**. For these technologies to be utilised they need to meet certain requirements for non-evasive disease measurement. Consequently, in the quest for a good, quick, and portable chemiresistive gas sensor for disease detection and VOC monitoring, certain issues need careful attention, such as superior sensitivities, good material designability, compact size, cross-selectivity from exhaled interfering gases, and low power consumption. In this study, the magnesium ferrites doped with Ce at various percentages in the octahedral site were investigated as suitable candidates for extremely high detection and sensing of flammables, volatile compounds, and benzene related vapours both at low and high concentrations. We, therefore, investigated the effect of Ce ions on the structure, magnetic, and sensing properties of magnesium ferrite prepared by the Glyco-thermal route.

2.3 PROPERTIES OF MAGNESIUM FERRITES

Magnesium ferrite ($MgFe_2O_4$) can be characterised as an n-type semiconductor which is evident by the occupancies of Mg^{+2} ions on tetrahedral-site and or Fe^{+2} to Fe^{+3} occupancies in octahedral-site**[3, 67, 80]**. It has a narrow bandgap of 1.9 eV **[67]**. Magnesium ferrite is one of the soft magnetic materials which find extensive application in our modern technologies. In fact, it has a partially inverse spinel structure where both Mg and Fe ions occupy the tetrahedral and octahedral site. Substitution of a small amount of Fe^{+3} by rare earths ions (RE^{+3}) in their structure induces the RE-Fe super-exchange interaction which leads to modification of their electrical and magnetic properties since it is governed by the nature and cations distribution in their tetrahedral and octahedral sublattice site**[81, 82]**.

2.4 GAS SENSING MECHANISM OF FERRITES ($MgFe_2O_4$)

Gas sensing mechanisms involve the interaction of the analyte gas molecule with the semiconductor surface. As mentioned earlier sensing materials can be classified as n-type or p-

type semiconductor and ferrites (AB_2O_4) nanoparticles too. The n-type semiconductor has electrons as majority carriers while the p-type semiconductor has holes as majority carriers. When ferrite sensors are exposed to an oxygen abundant environment, the oxygen molecules adsorb on the surface of sensing layer via chemical adsorption. The electrons are transferred from gas sensing layers to adsorbed oxygen to form adsorbed oxygen ions (O_2^-, O^- or O^{2-}), following these reaction processes.

$$O_{2(gas)} \rightarrow O_{2(ads)} \quad (1)$$

$$O_{2(ads)} + e^- \xrightarrow{<100^\circ C} O^-_{2(ads)} \quad (2)$$

$$O^-_{2(ads)} + e^- \xrightarrow{100^\circ C<T<300^\circ C} 2O^-_{(ads)} \quad (3)$$

$$O^-_{(ads)} + e^- \xrightarrow{>300^\circ C} O^{-2}_{(ads)} \quad (4)$$

depending on the operating temperature**[83, 84].** When the analyte gas is allowed to enter the system the change in resistance of the sensor that is observed is chemiresistive, as shown in **Fig. 2.3**.

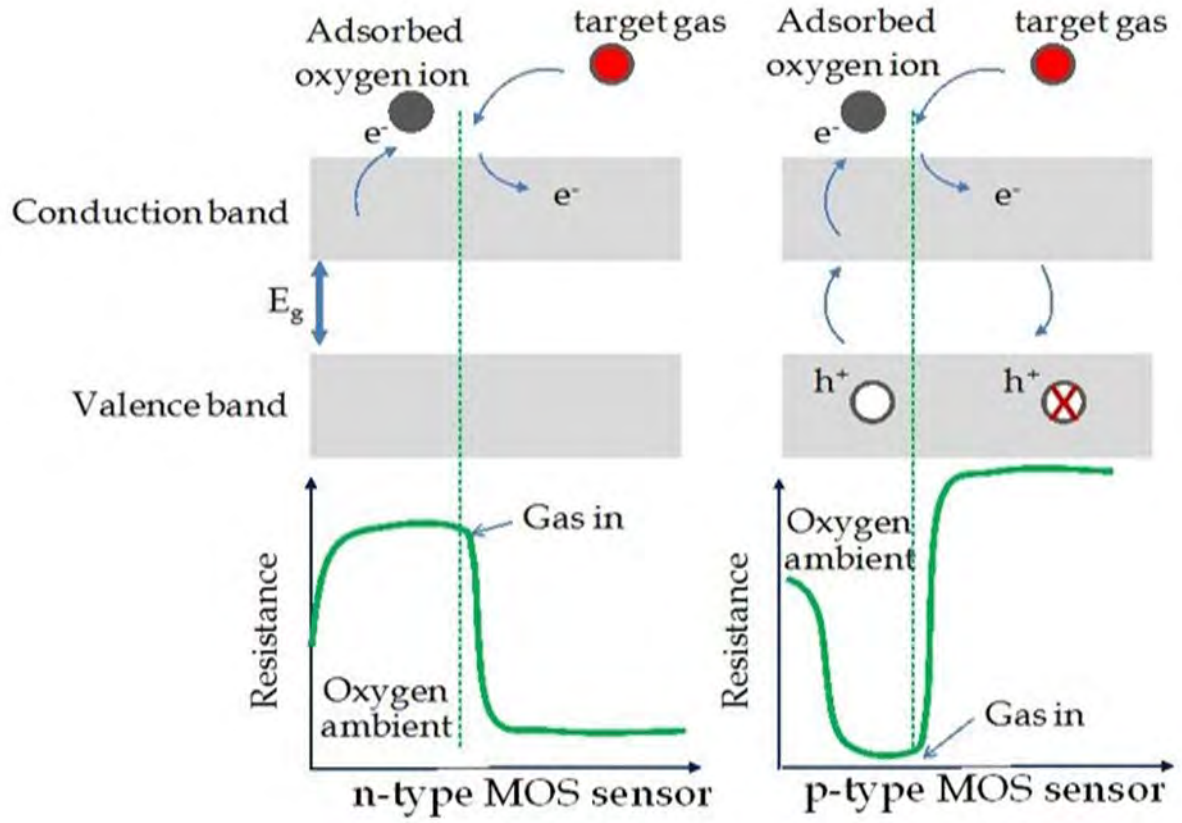

Figure 2. 3: Schematic diagram of the variation in sensor's resistance of n – and p- type MOS in the presence of an analyte gas (reducing gas)**[57]**.

The change in the resistance induced by the interaction of the gas and the sensor is considered to be the most important characteristic for the gas sensor.

2.5 PARAMETERS OF GAS SENSORS

In this subsection, we discuss the parameters that are important in gas sensing, and especially for the use of ferrites as sensors.

2.5.1 Pore structure

The vacant spaces between ceramic grains are commonly referred to as pores, and they can be further classified into three types: open passage pores, open dead-end pores, and internal or sealed pores**[85, 86]**. Depending on the cross sectional shapes, pores can be rectangular, square, split, or cylindrical. The size of these pores can be categorised as macrospores (average cross section diameter: 200 nm), mesoporous (between 2-200 mm), and microspores (approximately 2 mm). The ratio of total pores to volume is known as porosity, represented mathematically as **eq 2.1**.

$$P = \frac{V_p}{V} \qquad \text{Eq.....2. 1}$$

where Vp is the total pores volume and V is the volume of the body. Since the adsorption of the gas analyte occurs at the porous pores on the sensor's surface, porosity affects sensitivity[87]. Ferrites with open pore exhibit improved sensitivity**[88]**.

2.5.2 Surface area

Surface area plays a crucial role in gas sensing and has a significant impact on the sensitivity and performance of gas sensors**[89]**. Gas sensors are designed to detect and measure the presence and concentration of various gases in the environment. The surface area of the sensing material directly influences the sensor's ability to interact with gas molecules, thus affecting its sensitivity, response time, and selectivity**[90].** Gas molecules typically adsorb onto the surface

of the sensing material. A higher surface area provides more sites for gas molecules to adhere to, increasing the chances of interaction between the gas and the sensor. This enhances the sensitivity of the sensor and enables it to detect lower concentrations of the target gas. Specific surface area, A, refers to the ratio of total ceramic surface to its mass, as given by equation 2.2.

$$A = \frac{S}{m} \qquad \text{Eq.....2. 2}$$

where S = S_n (total surface area of ceramic body surface) and S_p (surface of internal pores). Rezlescu et al**[91]** established the specific area of ferrite using equation 2.3

$$A = \frac{S}{Vd} = \frac{6}{dD_m} \qquad \text{Eq.....2. 3}$$

where S is a particle's surface area, V is its volume, d is its bulk density, D_m is its average grain size, and 6 is a shape factor. In general, materials with smaller particle sizes and greater specific areas improve the gas sensing process**[92]**.

2.5.3 Sensitivity

Sensitivity can be defined as the slope that is calculated from the linear plot of response versus concentration. The response is the ratio of R_a, the sensor resistance in the absence of test gas analyte, and R_g, the sensor resistance in the presence of test gas analyte**[93]**. Mathematically, this is given by equation 2.4.

$$S = \frac{R_a}{R_g} \qquad \text{For a reducing gas} \qquad \text{Eq.....2. 4}$$

$$S = \frac{R_g}{R_a} \qquad \text{For an oxidising gas} \qquad \text{Eq.....2. 5}$$

It can also be expressed in terms of percentage.

$$S(\%) = \frac{(R_a - R_g)}{R_g} \times 100 \qquad \text{Eq.....2. 6}$$

It depends on the gas concentration (most frequently in a direct relationship), as well as the kind of material used. In an oxidizing gas analyte, the sensor resistance increases, but in a reducing gas analyte, it decreases. Additionally, the pore size, porosity, and specific area all affect sensitivity**[94, 95]**. Within certain limits, a large specific surface area results in high sensitivity**[96]**. The control of these variables is a significant issue in the manufacturing of ferrite sensors**[97]**. These issues are resolved by using a sufficient sintering temperature and adding appropriate additives that encourage pore development**[98]**. In the range of high concentrations, gas sensitivity tends to reach saturation**[99]**.

2.5.4 Selectivity

Selectivity is the ability of a sensor to preferentially detect a certain gas analyte in the presence of additional gases**[100]**. It is a crucial parameter since gases would typically occur in mixtures in real-world application situations. Controlling temperature, using catalysts and dopants, adding specific chemicals to the grain's surface, and using filters all increase sensitivity and selectivity**[101]**. By using the right electrode arrangement and sensing layer thickness, selectivity may also be improved. The selectivity of various gases varies amongst different sensing materials.

2.5.5 Repeatability

Repeatability is a measure of how consistently the sensor responds to the same concentration of the selected analyte gas species after measurement conditions have been changed.

2.5.6 Stability

Stability is the ability of a sensor to provide the same results. Therefore, the sensitivity, selectivity, response, and recovery time of the sensor remains unchanged.

2.5.7 Limit of detection

The limit of detection is the lowest signal, or the lowest corresponding concentration of a gas the sensor can detect or determined from the signal, that can be observed with a sufficient degree of confidence.

2.5.8 Operation Temperature

The measurement of gas response has proven that it is temperature dependent**[102]**. Temperature-dependent electrical characteristics of semiconducting metal oxides are determined by their polarisations, which include interfacial, dipolar, atomic, and electronic polarizations**[103, 104]**. The temperature has a significant impact on the dipolar and interfacial polarizations. Ceramic gas sensor sensitivity is thus determined by operating temperature**[105]**. Low sensitivity results from the gas analyte's inability to react thermally with the adsorbed oxygen species, O^{-2}, at low temperatures. As a result, sensitivity is directly related to operating temperature until the optimal temperature is reached, thereafter sensitivity drops with further increase in temperature. Since high temperatures are not conducive to the exothermic adsorption process, the sensitivity response decreases, and further increase in temperature results in a larger desorption rate compared to the adsorption rate**[106]**. The kind of test gas, chemical composition, dopants, and catalyst all affect the temperature that corresponds to maximal sensitivity**[107]**. The enhanced sensitivity at high temperatures is attributed to sufficiently high thermal energy that assists in overcoming the surface reaction's activation energy barrier as well as the conversion of adsorbed oxygen species from O^{-2} to O^{-} at higher temperatures, which increases the electron concentration after the maximum sensitivity is reached**[108, 109]**.

2.5.9 Crystalline size, Grain size/Particle size

Crystallite refers to each crystal found within a grain or particle. Numerous crystals are present in every grain. In addition to its particle size, a grain's diameter also matters. Particles of a size of smaller than 10^{-5} centimetres (1000Å) tend to improve strength and hardness with

decreasing grain size**[110]**. Chen et al.**[111]** examined the impact of grain size in their investigation of copper, zinc, cadmium, and magnesium ferrites. It was discovered that the grain size and surface area both influence gas sensitivity. Smaller grain size samples have more surface area and higher gas sensitivity than bigger grain size samples, which have less surface area. Increasing the material's surface area would be the most effective technique to increase the sensor's sensitivity.

2.5.11 Dopants/additives

Adding or replacing metal ions in ferrites can increase the sensitivity, selectivity, and response time of ferrite gas sensors. According to Sutka et al.**[61]** an increase in donor concentration results in an increase in overall sensitivity, which is explained by an increase in the amount of adsorbed oxygen species on the grain surface. Carbon monoxide (CO) and ethanol sensing characteristics of cobalt ferrite nanoparticles were examined by Joshi et al.**[112]** Working temperature was lowered from 325 °C to 225 °C, and improved sensitivity was seen. Kadu et al.**[113]** investigated how palladium inclusion affected the $Zn_{0.6}Mn_{0.4}Fe_2O_4$ ethanol sensor. It was demonstrated that when the working temperature dropped from 300 °C to 200 °C, sensitivity rose. The effect of tungsten substitution on nickel ferrite for hydrogen sensing was investigated by Pathania et al.**[114]** A minimum temperature of 80 °C caused the sensor to become more sensitive. Gadkari et al.**[115]** investigated the impact of sm^{3+} ion addition on $MgCd_xFe_2O_4$ sensing characteristics toward LPG, Cl_2, and C_2H_2OH. It was noted that the operating temperature decreased from 222 °C to 198 °C. The fundamental function of metal substitution in ferrite gas sensors is to reduce the operating temperature while also boosting sensitivity, as demonstrated by the samples above. Two different methods are used to do this. The first one involves altering the ferrite's microstructure by lowering the particle size, which increases the surface area. The ferrite's electrical conductivity is altered via the introduction of dopants, which improves sensitivity.

2.5.12 Response Characteristics

The rate at which a gas sensor can detect changes in gas concentration and produce a proportional output is known as its response characteristic. For applications needing real-time monitoring or quick responses, it is a crucial metric. The amount of time it takes a gas sensor to detect and record a change in gas concentration is referred to as the gas sensor response time**[116]**. Usually, it is determined by how long it takes for the sensor output to reach a certain percentage (such as 90% or 95%) after being exposed to a step change in gas concentration. The extrapolation of the response and recovery time from the gas sensing data/plot is shown in Fig. 2. 4. The amount of time it takes for a gas sensor to recover from exposure to the gas and resume operating at its baseline output level is known as the recovery time. The sensor may require some time to fully recover and stabilise after being exposed to a gas. When the sensor needs to be prepared to detect further changes in gas concentration, the recovery period is very important

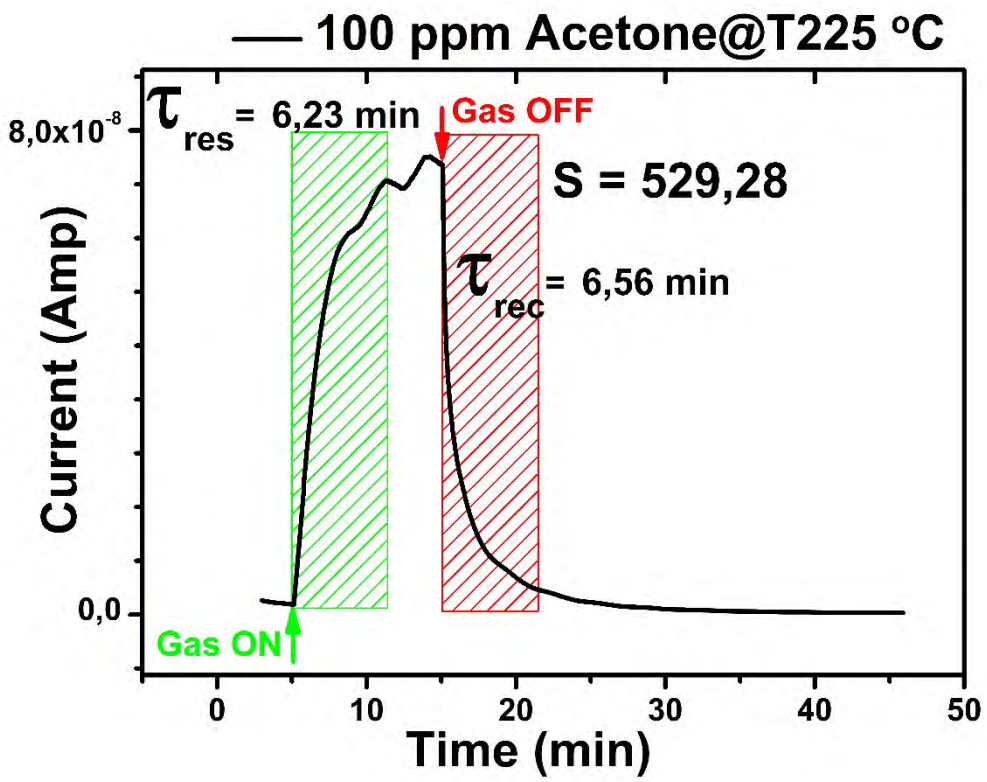

Figure 2. 4: Typical example of response and recovery times.

Other response characteristics are stability and drift. The capacity of the sensor to deliver dependable and constant performance throughout time is referred to as stability**[117]**. Drift is the term used to describe a long-term, steady shift in the sensor's output or response characteristics**[118]**. Applications requiring long-term monitoring must have high stability and little drift. The exact technology employed in the gas sensor, such as electrochemical, semiconductor, or optical-based sensors, can have a considerable impact on these parameters. Different sensor types are useful for particular applications and target gases since they each have different strengths and drawbacks

2.6 REFERENCES

[1] A. Mirzaei, S.G. Leonardi, G. Neri, Detection of hazardous volatile organic compounds (VOCs) by metal oxide nanostructures-based gas sensors., Ceramic International 42 (2016) 15119-15141.

[2] N. Tammanoon, A. Wisitsoraat, D. Phokharatkul, A. Tuantranont, S. Phanichphant, V. Yordsri, C. Liewhiran, Highly sensitive acetone sensors based on flame-spray-made La2O3-doped SnO2 nanoparticulate thick films, Sensors and Actuators B: Chemical 262 (2018) 245-262.

[3] Run Zhang, Yan Wang, Zhanying Zhang, J. Cao, Highly Sensitive Acetone Gas Sensor Based on g-C3N4 Decorated MgFe2O4 Porous Microspheres Composites., Sensors 18 (2018) 2211.

[4] A.K. Yadav, R.K. Singh, P. Singh, Fabrication of lanthanum ferrite based liquefied petroleum gas sensor, Sensors and actuators B: chemical 229 (2016) 25-30.

[5] R.K. Sonker, M. Singh, U. Kumar, B. Yadav, MWCNT doped ZnO nanocomposite thin film as LPG sensing, Journal of Inorganic and Organometallic Polymers and Materials 26 (2016) 1434-1440.

[6] T. Hübert, L. Boon-Brett, V. Palmisano, M.A. Bader, Developments in gas sensor technology for hydrogen safety, International Journal of Hydrogen Energy 39 (2014) 20474-20483.

[7] Y. Shao, Y. Ying, J. Ping, Recent advances in solid-contact ion-selective electrodes: Functional materials, transduction mechanisms, and development trends, Chemical Society Reviews 49 (2020) 4405-4465.

[8] Y. Guo, X. Wei, S. Gao, W. Yue, Y. Li, G. Shen, Recent advances in carbon material-based multifunctional sensors and their applications in electronic skin systems, Advanced Functional Materials 31 (2021) 2104288.

[9] T. Aldhafeeri, M.-K. Tran, R. Vrolyk, M. Pope, M. Fowler, A review of methane gas detection sensors: Recent developments and future perspectives, Inventions 5 (2020) 28.

[10] R.A.B. John, A.R. Kumar, A review on resistive-based gas sensors for the detection of volatile organic compounds using metal-oxide nanostructures, Inorganic Chemistry Communications 133 (2021) 108893.

[11] J. Goldschmidt, L. Nitzsche, S. Wolf, A. Lambrecht, J. Wöllenstein, Rapid quantitative analysis of IR absorption spectra for trace gas detection by artificial neural networks trained with synthetic data, Sensors 22 (2022) 857.

[12] F. Radica, G. Della Ventura, L. Malfatti, M.C. Guidi, A. D'Arco, A. Grilli, A. Marcelli, P. Innocenzi, Real-time quantitative detection of styrene in atmosphere in presence of other volatile-organic compounds using a portable device, Talanta 233 (2021) 122510.
[13] V. Baloria, A. Yadav, P. Singh, G. Gupta, Semiconductor oxide based chemiresistive gas sensors, Carbon Nanomaterials and their Nanocomposite-Based Chemiresistive Gas Sensors, Elsevier (2023), pp. 133-167.
[14] B.G. Toksha, S.E. Shirsath, Metal Oxides as Chemical Sensors, Materials for Chemical Sensors, CRC Press (2023), pp. 1-18.
[15] F. Schipani, E.A. Villegas, L.A. Ramajo, R. Parra, Zinc oxide thin films for a room temperature dual carbon dioxide and carbon monoxide sensor, Journal of Materials Science: Materials in Electronics 34 (2023) 1092.
[16] M. Dong, C. Zheng, S. Miao, Y. Zhang, Q. Du, Y. Wang, F.K. Tittel, Development and measurements of a mid-infrared multi-gas sensor system for CO, CO2 and CH4 detection, Sensors 17 (2017) 2221.
[17] A.A. Ibrahim, Carbon dioxide and carbon monoxide level detector, 2018 21st International Conference of Computer and Information Technology (ICCIT), IEEE, 2018, pp. 1-5.
[18] P. Shuk, C. McGuire, E. Brosha, Methane gas sensing technologies in combustion: Comprehensive review, Sensors & Transducers 229 (2019).
[19] Y. Deng, Y. Deng, Applications of semiconducting metal oxides gas sensors, Semiconducting Metal Oxides for Gas Sensing (2019) 195-241.
[20] P. Saxena, P. Shukla, A review on recent developments and advances in environmental gas sensors to monitor toxic gas pollutants, Environmental Progress & Sustainable Energy (2023) e14126.
[21] B. Turan, K.A. Demir, B. Soner, S.C. Ergen, Visible light communications in the industrial internet of things (IIOT), The Internet of Things in the Industrial Sector: Security and Device Connectivity, Smart Environments, and Industry 4.0, Springer (2019), pp. 163-191.
[22] M. Carminati, G. Ferrari, M. Sampietro, Emerging miniaturized technologies for airborne particulate matter pervasive monitoring, Measurement 101 (2017) 250-256.
[23] J. Zhao, S. Zhang, Y. Sun, N. Zhou, H. Yu, H. Zhang, D. Jia, Wearable optical sensing in the medical internet of things (MIoT) for pervasive medicine: Opportunities and challenges, Acs Photonics 9 (2022) 2579-2599.
[24] W.H. Brattain, J. Bardeen, Surface properties of germanium, The Bell System Technical Journal 32 (1953) 1-41.

[25] T. Seiyama, A. Kato, K. Fujiishi, M. Nagatani, A new detector for gaseous components using semiconductive thin films, Analytical Chemistry 34 (1962) 1502-1503.
[26] K. Kalyanasundaram, Photoelectrochemical cell studies with semiconductor electrodes—A classified bibliography (1975–1983), Solar Cells 15 (1985) 93-156.
[27] A. Azad, S. Akbar, S. Mhaisalkar, L. Birkefeld, K. Goto, Solid-state gas sensors: A review, Journal of the Electrochemical Society 139 (1992) 3690.
[28] A.K. Ruchika, Performance analysis of Zinc oxide based alcohol sensors, Int. J. Appl. Sci. Eng. Res 4 (2015) 428-436.
[29] A. Chatterjee, P. Bhattacharjee, N.K. Roy, Manganese doped Zinc oxide thin film hydrogen gas sensor at reduced operating temperature, 2011 4th IEEE International Workshop on Advances in Sensors and Interfaces (IWASI), IEEE, 2011, pp. 148-152.
[30] D.E. Motaung, G.H. Mhlongo, A.S. Bolokang, B.P. Dhonge, H.C. Swart, S.S. Ray, Improved sensitivity and selectivity of pristine zinc oxide nanostructures to H2S gas: Detailed study on the synthesis reaction time, Applied Surface Science 386 (2016) 210-223.
[31] L.-Y. Zhu, K. Yuan, J.-G. Yang, H.-P. Ma, T. Wang, X.-M. Ji, J.-J. Feng, A. Devi, H.-L. Lu, Fabrication of heterostructured p-CuO/n-SnO2 core-shell nanowires for enhanced sensitive and selective formaldehyde detection, Sensors and Actuators B: Chemical 290 (2019) 233-241.
[32] H. Chen, M.C. Roco, J. Son, S. Jiang, C.A. Larson, Q. Gao, Global nanotechnology development from 1991 to 2012: patents, scientific publications, and effect of NSF funding, Journal of Nanoparticle Research 15 (2013) 1-21.
[33] N.A. Ochekpe, P.O. Olorunfemi, N.C. Ngwuluka, Nanotechnology and drug delivery part 1: background and applications, Tropical Journal of Pharmaceutical Research 8 (2009).
[34] J. Creighton, P. Ho, Introduction to chemical vapor deposition (CVD), Chemical Vapor Deposition 2 (2001) 1-22.
[35] Y.M. Manawi, Ihsanullah, A. Samara, T. Al-Ansari, M.A. Atieh, A review of carbon nanomaterials' synthesis via the chemical vapor deposition (CVD) method, Materials 11 (2018) 822.
[36] Y. Deng, Y. Deng, Sensing mechanism and evaluation criteria of semiconducting metal oxides gas sensors, Springer 2019.
[37] J. Walker, P. Karnati, S.A. Akbar, P.A. Morris, Selectivity mechanisms in resistive-type metal oxide heterostructural gas sensors, Sensors and Actuators B: Chemical 355 (2022) 131242.
[38] B.-H. Jang, O. Landau, S.-J. Choi, J. Shin, A. Rothschild, I.-D. Kim, Selectivity enhancement of SnO2 nanofiber gas sensors by functionalization with Pt nanocatalysts and

manipulation of the operation temperature, Sensors and Actuators B: Chemical 188 (2013) 156-168.
[39] M.K. Sohal, A. Mahajan, S. Gasso, S.V. Nahirniak, T.A. Dontsova, R.C. Singh, Modification of SnO2 surface oxygen vacancies through Er doping for ultralow NO2 detection, Materials Research Bulletin 133 (2021) 111051.
[40] S. Das, S. Mojumder, D. Saha, M. Pal, Influence of major parameters on the sensing mechanism of semiconductor metal oxide based chemiresistive gas sensors: A review focused on personalized healthcare, Sensors and Actuators B: Chemical 352 (2022) 131066.
[41] A. Bag, N.E. Lee, Recent advancements in development of wearable gas sensors, Advanced Materials Technologies 6 (2021) 2000883.
[42] A. Sharma, G. Gupta, Recent development and prospects for metal Selenide-based gas sensors, Materials Science and Engineering: B 290 (2023) 116333.
[43] S.D. Lawaniya, S. Kumar, Y. Yu, K. Awasthi, Ammonia sensing properties of PPy nanostructures (urchins/flowers) towards low-cost and flexible gas sensors at room temperature, Sensors and Actuators B: Chemical 382 (2023) 133566.
[44] S.D. Lawaniya, S. Kumar, Y. Yu, H.-G. Rubahn, Y.K. Mishra, K. Awasthi, Functional nanomaterials in flexible gas sensors: recent progress and future prospects, Materials Today Chemistry 29 (2023) 101428.
[45] Q. Zhou, Z. Geng, L. Yang, B. Shen, Z. Kan, Y. Qi, S. Hu, B. Dong, X. Bai, L. Xu, A Wearable Healthcare Platform Integrated with Biomimetical Ions Conducted Metal–Organic Framework Composites for Gas and Strain Sensing in Non-Overlapping Mode, Advanced Science (2023) 2207663.
[46] N.M. Nurazzi, N. Abdullah, S.Z.N. Demon, N.A. Halim, A.F.M. Azmi, V.F. Knight, I.S. Mohamad, The frontiers of functionalized graphene-based nanocomposites as chemical sensors, Nanotechnology Reviews 10 (2021) 330-369.
[47] S. Ghosh, M. Narjinary, A. Sen, R. Bandyopadhyay, S. Roy, Fast detection of low concentration carbon monoxide using calcium-loaded tin oxide sensors, Sensors and Actuators B: Chemical 203 (2014) 490-496.
[48] V. Ambardekar, T. Bhowmick, P. Bandyopadhyay, Understanding on the hydrogen detection of plasma sprayed tin oxide/tungsten oxide (SnO2/WO3) sensor, International Journal of Hydrogen Energy 47 (2022) 15120-15131.
[49] J.-A. Woo, D.-T. Phan, Y.W. Jung, K.-J. Jeon, Fast response of hydrogen sensor using palladium nanocube-TiO2 nanofiber composites, International Journal of Hydrogen Energy 42 (2017) 18754-18761.

[50] S. Pawar, M. Chougule, S. Sen, V. Patil, Development of nanostructured polyaniline–titanium dioxide gas sensors for ammonia recognition, Journal of Applied Polymer Science 125 (2012) 1418-1424.
[51] K. Suematsu, K. Watanabe, A. Tou, Y. Sun, K. Shimanoe, Ultraselective toluene-gas sensor: nanosized gold loaded on zinc oxide nanoparticles, Analytical Chemistry 90 (2018) 1959-1966.
[52] Q.A. Drmosh, I. Olanrewaju Alade, M. Qamar, S. Akbar, Zinc Oxide-Based Acetone Gas Sensors for Breath Analysis: A Review, Chemistry–An Asian Journal 16 (2021) 1519-1538.
[53] S.G. Leonardi, Two-dimensional zinc oxide nanostructures for gas sensor applications, Chemosensors 5 (2017) 17.pages?
[54] A. Yadav, P. Singh, G. Gupta, Dimension dependency of tungsten oxide for efficient gas sensing, Environmental Science: Nano 9 (2022) 40-60.
[55] H. Khan, A. Zavabeti, J.Z. Ou, T. Daeneke, Y. Li, K. Kalantar-zadeh, Two dimensional tungsten oxide nanosheets with unprecedented selectivity and sensitivity to NO 2, 2017 IEEE SENSORS, IEEE, 2017, pp. 1-3.
[56] M.-T. Udristioiu, M. Osiac, Au-incorporated tungsten trioxide obtained by pulsed laser deposition, AIP Conference Proceedings, AIP Publishing LLC, 2020, pp. 030012.
[57] M.A. Njoroge, N.M. Kirimi, K.P. Kuria, Spinel ferrites gas sensors: a review of sensing parameters, mechanism and the effects of ion substitution, Critical Reviews in Solid State and Materials Sciences 47 (2022) 807-836.
[58] Y. Chao, S. Yao, W.J. Buttner, J.R. Stetter, Amperometric sensor for selective and stable hydrogen measurement, Sensors and Actuators B: Chemical 106 (2005) 784-790.
[59] J. Pang, H. Dong, K. Pang, X. Le, Z. Xu, C. Gao, J. Xie, Selective detection of CO 2 and H 2 O dual analytes through decoupling surface density and shear modulus based on single SAW resonator, IEEE Electron Device Letters 43 (2022) 450-453.
[60] X. Zeng, W. Jiang, G.I. Waterhouse, X. Jiang, Z. Zhang, L. Yu, Stable Pb (II) ion-selective electrodes with a low detection limit using silver nanoparticles/polyaniline as the solid contact, Microchimica Acta 188 (2021) 1-11.
[61] A. Šutka, K.A. Gross, Spinel ferrite oxide semiconductor gas sensors, Sensors and Actuators B: Chemical 222 (2016) 95-105.
[62] A.B. Gadkari, T.J. Shinde, P.N. Vasambekar, Ferrite gas sensors, IEEE Sensors Journal 11 (2010) 849-861.
[63] M. Miralaei, S. Salari, P. Kameli, M.T. Goodarzi, M. Ranjbar, Electrical and hydrogen gas sensing properties of Co1-xZnxFe2O4 nanoparticles; effect of the sputtered palladium thin layer, International Journal of Hydrogen Energy (2023) ^^.

[64] M. Ma, L. Chen, L. Peng, Y. Peng, J. Bi, D. Gao, J. Wu, Carrier and oxygen vacancy engineering of aliovalent ion modified BiFeO3 and their gas sensing properties, Sensors and Actuators B: Chemical 370 (2022) 132400.
[65] K. Wu, J. Li, C. Zhang, Zinc ferrite based gas sensors., Ceramic International 45 (2019) 11143-11157.
[66] Hamid Reza Ebrahimi, Mohammad Parish, Gholam Reza Amiri, Behzad Bahraminejad, S. Fatahian, Synthesis, characterization and gas sensitivity investigation of Ni0.5Zn0.5Fe2O4 nanoparticles., Journal of Magnetism and Magnetic Material 44 (2016) 55-58.
[67] Andris ˇSutka, Karlis A. Grossa, Spinel ferrite oxide semiconductor gas sensors., Sensors and Actuators B 222 (2016) 95-105.
[68] Libretext, Introduction to inorganic chemistry, https://LibreTexts.org), 2020.
[69] X. Zeng, Z. Hou, J. Ju, L. Gao, J. Zhang, Y. Peng, The cation distributions of Zn-doped normal spinel MgFe2O4 ferrite and its magnetic properties, Materials 15 (2022) 2422.
[70] C. Chinnasamy, A. Narayanasamy, N. Ponpandian, K. Chattopadhyay, K. Shinoda, B. Jeyadevan, K. Tohji, K. Nakatsuka, T. Furubayashi, I. Nakatani, Mixed spinel structure in nanocrystalline NiFe 2 O 4, Physical Review B 63 (2001) 184108.
[71] N. Rezlescu, N. Iftimie, E. Rezlescu, C. Doroftei, P.D. Popa, Semiconducting gas sensor for acetone based on the fine grained nickel ferrite, Sensors and Actuators B: Chemical 114 (2006) 427-432.
[72] S.L. Darshane, S. Suryavanshi, I. Mulla, Nanostructured nickel ferrite: a liquid petroleum gas sensor, Ceramics International 35 (2009) 1793-1797.
[73] Panpan Zhang, W.L. Hongwei Qin, Heng Zhang, Jifan Hu, Gas sensors based on ytterbium ferrites nanocrystalline powders for detecting acetone with low concentrations., Sensors and actuators B 246 (2017) 9-19.
[74] Sonam Chakraborty, M. Pal, Highly selective and stable acetone sensor based on chemically prepared bismuth ferrite nanoparticles., Journal of Alloys and Compounds 787 (2019) 1204-1211.
[75] P. Ghadage, P. Kodam, D. Nadargi, S. Patil, M. Tamboli, N. Bhandari, I. Mulla, C. Park, S. Suryavanshi, Pd loaded bismuth ferrite: A versatile perovskite for dual applications as acetone gas sensor and photocatalytic dye degradation of malachite green, Ceramics International 49 (2023) 5738-5747.
[76] Huiling Tai, Si Wang, Zaihua Duan, Y. Jiang, Evolution of breath analysis based on humidity and gas sensors Potential and challenges., Sensors and Actuators B 318 (2020).
[77] A.T. Güntner, S. Abegg, K. Königstein, P.A. Gerber, A. Schmidt-Trucksäss, S.E. Pratsinis, Breath sensors for health monitoring, ACS Sensors 4 (2019).

[78] J.-W. Yoon, J.-H. Lee, Toward breath analysis on a chip for disease diagnosis using semiconductor-based chemiresistors Recent progress and future perspectives., Lab Chip 17 (2017).
[79] M. Righettoni, A. Amann, S. E. Pratsinis, Breath analysis by nanostructured metal oxides as chemo-resistive gas sensors., Materials Today 18 (2015).
[80] Hai-Jun Zhang, Li-Zhu Liu, Xiao-Rui Zhang, Shuang Zhang, F.-N. Meng, Microwave-assisted solvothermal synthesis of shape-controlled CoFe2O4 nanoparticles for acetone sensor., Journal of Alloys and Compounds 788 (2019) 1103-1112.
[81] V. Jagadeesha Angadi, S. Matteppanavar, N. Maramu, P.M. Kumar, U. Mahaboob Pasha, P. Deepthi, K. Praveena, Reduced A–B super exchange interaction in Sm 3+–Gd 3+-doped Mn–Zn ferrites due to high energy gamma irradiation, Indian Journal of Physics 93 (2019) 169-174.
[82] B. Sahanashree, E. Melagiriyappa, M. Veena, G. Shankaramurthy, H. Somashekarappa, Influence of Neodymium and gamma rays irradiation on structural electrical and magnetic properties of Co-Zn nanoferrites, Materials Chemistry and Physics 214 (2018) 143-153.
[83] S.S. Nkosi, I. Kortidis, D.E. Motaung, R.E. Kroon, N. Leshabane, J. Tshilongo, O.M. Ndwandwe, The effect of stabilized ZnO nanostructures green luminescence towards LPG sensing capabilities, Materials Chemistry and Physics 242 (2020).
[84] N. Zahmouli, M. Hjiri, S.G. Leonardi, L. El Mir, G. Neri, D. Iannazzo, C. Espro, M.S. Aida, High performance Gd-doped γ-Fe2O3 based acetone sensor, Materials Science in Semiconductor Processing 116 (2020).
[85] F.A. Dullien, V. Batra, Determination of the structure of porous media, Industrial & Engineering Chemistry 62 (1970) 25-53.
[86] S. Lagorsse, F. Magalhaes, A. Mendes, Carbon molecular sieve membranes: Sorption, kinetic and structural characterization, Journal of Membrane Science 241 (2004) 275-287.
[87] R. Paul, B. Das, R. Ghosh, Novel approaches towards design of metal oxide based hetero-structures for room temperature gas sensor and its sensing mechanism: A recent progress, Journal of Alloys and Compounds (2023) 168943. Please check the original. The phrase highlighted is not grammatical.
[88] X. Li, W. Sun, W. Fu, H. Lv, X. Zu, Y. Guo, D. Gibson, Y.-Q. Fu, Advances in sensing mechanisms and micro/nanostructured sensing layers for surface acoustic wave-based gas sensors, Journal of Materials Chemistry A (2023).pages?
[89] S. Bilge, B. Dogan-Topal, A. Yücel, A. Sınağ, S.A. Ozkan, Recent advances in flower-like nanomaterials: Synthesis, characterization, and advantages in gas sensing applications, TrAC Trends in Analytical Chemistry (2022) 116638.

[90] M. Mittal, A. Kumar, Carbon nanotube (CNT) gas sensors for emissions from fossil fuel burning, Sensors and Actuators B: Chemical 203 (2014) 349-362.
[91] N. Rezlescu, C. Doroftei, P.D. Popa, Humidity-sensitive electrical resistivity of MgFe~ 2O~ 4 and Mg~ 0~.~ 9Sn~ 0~.~ 1Fe~ 2O~ 4 porous ceramics, Romanian Journal of Physics 52 (2007) 353.
[92] J. Xu, Q. Pan, Z. Tian, Grain size control and gas sensing properties of ZnO gas sensor, Sensors and Actuators B: Chemical 66 (2000) 277-279.
[93] Y. Liu, G. Li, R. Mi, C. Deng, P. Gao, An environment-benign method for the synthesis of p-NiO/n-ZnO heterostructure with excellent performance for gas sensing and photocatalysis, Sensors and Actuators B: Chemical 191 (2014) 537-544.
[94] Z. Liu, T. Fan, D. Zhang, X. Gong, J. Xu, Hierarchically porous ZnO with high sensitivity and selectivity to H2S derived from biotemplates, Sensors and Actuators B: Chemical 136 (2009) 499-509.
[95] W. Li, J. Tang, Z. Wang, Micro-/mesoporous fluorescent polymers and devices for visual pesticide detection with portability, high sensitivity, and ultrafast response, ACS Applied Materials & Interfaces 14 (2022) 5815-5824.
[96] S.G. Chatterjee, S. Chatterjee, A.K. Ray, A.K. Chakraborty, Graphene–metal oxide nanohybrids for toxic gas sensor: A review, Sensors and Actuators B: Chemical 221 (2015) 1170-1181.
[97] R. Godbole, P. Rao, P. Alegaonkar, S. Bhagwat, Influence of fuel to oxidizer ratio on LPG sensing performance of MgFe2O4 nanoparticles, Materials Chemistry and Physics 161 (2015) 135-141.
[98] Y. Yang, H. Zhang, J. Li, F. Xu, G. Gan, D. Wen, Effects of Bi2O3-Nb2O5 additives on microstructure and magnetic properties of low-temperature-fired NiCuZn ferrite ceramics, Ceramics International 44 (2018) 10545-10550.
[99] R. Wadhwa, A. Kumar, R. Sarkar, P.P. Mohanty, D. Kumar, S. Deswal, P. Kumar, R. Ahuja, S. Chakraborty, M. Kumar, Pt Nanoparticles on Vertically Aligned Large-Area MoS2 Flakes for Selective H2 Sensing at Room Temperature, ACS Applied Nano Materials 6 (2023) 2527-2537.
[100] N. Alzate-Carvajal, A. Luican-Mayer, Functionalized graphene surfaces for selective gas sensing, ACS omega 5 (2020) 21320-21329.
[101] J.M. Walker, S.A. Akbar, P.A. Morris, Synergistic effects in gas sensing semiconducting oxide nano-heterostructures: A review, Sensors and Actuators B: Chemical 286 (2019) 624-640.

[102] M. Kumar, V. Bhatt, A.C. Abhyankar, J.-H. Yun, H.-J. Jeong, Multifunctional dumbbell-shaped ZnO based temperature-dependent UV photodetection and selective H2 gas detection, International Journal of Hydrogen Energy 45 (2020) 15011-15025.
[103] Ö. Sevgili, Y. Azizian-Kalandaragh, Ş. Altındal, Frequency and voltage dependence of electrical and dielectric properties in metal-interfacial layer-semiconductor (MIS) type structures, Physica B: Condensed Matter 587 (2020) 412122.
[104] A.K. Bhunia, S.S. Pradhan, K. Bhunia, A.K. Pradhan, S. Saha, Study of the optical properties and frequency-dependent electrical modulus spectrum to the analysis of electric relaxation and conductivity effect in zinc oxide nanoparticles, Journal of Materials Science: Materials in Electronics 32 (2021) 22561-22578.
[105] M. Radecka, K. Zakrzewska, M. Rękas, SnO2–TiO2 solid solutions for gas sensors, Sensors and Actuators B: Chemical 47 (1998) 194-204.
[106] Y. Wang, B. Liu, S. Xiao, H. Li, L. Wang, D. Cai, D. Wang, Y. Liu, Q. Li, T. Wang, High performance and negative temperature coefficient of low temperature hydrogen gas sensors using palladium decorated tungsten oxide, Journal of Materials Chemistry A 3 (2015) 1317-1324.
[107] G. Zhang, M. Liu, Effect of particle size and dopant on properties of SnO2-based gas sensors, Sensors and Actuators B: Chemical 69 (2000) 144-152.
[108] J. Chang, H. Kuo, I. Leu, M. Hon, The effects of thickness and operation temperature on ZnO: Al thin film CO gas sensor, Sensors and actuators B: Chemical 84 (2002) 258-264.
[109] S. Wang, J. Cao, W. Cui, L. Fan, X. Li, D. Li, Oxygen vacancies and grain boundaries potential barriers modulation facilitated formaldehyde gas sensing performances for In2O3 hierarchical architectures, Sensors and Actuators B: Chemical 255 (2018) 159-165.
[110] M. Khandekar, N. Tarwal, I. Mulla, S. Suryavanshi, Nanocrystalline Ce doped CoFe2O4 as an acetone gas sensor, Ceramics International 40 (2014) 447-452.
[111] C.V.G. Reddy, S.V. Manorama, V.J. Rao, Preparation and characterisation of ferrites as gas sensor materials, Journal of Materials Science Letters 19 (2000) 775-778.
[112] S. Joshi, V.B. Kamble, M. Kumar, A.M. Umarji, G. Srivastava, Nickel substitution induced effects on gas sensing properties of cobalt ferrite nanoparticles, Journal of Alloys and Compounds 654 (2016) 460-466.
[113] A. Kadu, S. Jagtap, G. Chaudhari, Studies on the preparation and ethanol gas sensing properties of spinel Zn0. 6Mn0. 4Fe2O4 nanomaterials, Current Applied Physics 9 (2009) 1246-1251.

[114] A. Pathania, P. Thakur, A.V. Trukhanov, S.V. Trukhanov, L.V. Panina, U. Lüders, A. Thakur, Development of tungsten doped Ni-Zn nano-ferrites with fast response and recovery time for hydrogen gas sensing application, Results in Physics 15 (2019) 102531.
[115] A.B. Gadkari, T.J. Shinde, P.N. Vasambekar, Effect of Sm3+ ion addition on gas sensing properties of Mg1− xCdxFe2O4 system, Sensors and Actuators B: Chemical 178 (2013) 34-39.
[116] S. Virji, J. Huang, R.B. Kaner, B.H. Weiller, Polyaniline nanofiber gas sensors: examination of response mechanisms, Nano letters 4 (2004) 491-496.
[117] S. Wang, Y. Wu, Y. Gu, T. Li, H. Luo, L.-H. Li, Y. Bai, L. Li, L. Liu, Y. Cao, Wearable sweatband sensor platform based on gold nanodendrite array as efficient solid contact of ion-selective electrode, Analytical Chemistry 89 (2017) 10224-10231.
[118] R.A. Potyrailo, Multivariable sensors for ubiquitous monitoring of gases in the era of internet of things and industrial internet, ChemicalReviews 116 (2016) 11877-11923.

CHAPTER 3

MATERIALS, SYNTHESIS AND CHARACTERISATION TECHNIQUES

3.1 INTRODUCTION

This chapter describes the synthesis methods used to synthesise cerium-doped magnesium ferrites and the characterisation techniques. The $MgCe_xFe_{2-x}O_4$ nano ferrites where x = 0.0, 0.05, 0.1and 0.2 were synthesised by the glycothermal method using a Parr pressure reactor. They were then subjected to different characterisation techniques to study their structural, surface morphology, optical and gas sensing properties.

3.2 MATERIAL SYNTHESIS

3.2.1 Glycothermal Synthesis

The composition with the general formula $MgCe_xFe_{2-x}O_4$ where x= 0.0, 0.05, 0.1, 0.2 was prepared by the glycol-thermal method using high-purity metal chlorides as starting materials. The calculated stoichiometric ratio of $MgCl_2.6H_2O$ (98%), $CeCl_3.6H_2O$ (99%) and $FeCl_3.6H_2O$ (98%) all supplied by Aldrich were measured and mixed in 400 ml deionized water under a magnetic stirrer with constant stirring. Once all the metal chlorides were dissolved, ammonium hydroxide was used as a precipitant, and it was slowly added dropwise in a chloride solution mixture until PH$\approx$9.5 was reached. Then the precipitate was filtered and washed several times with deionized water over a Whatman glass microfiber filter (GF/F) with the aid of a suction flask operating on the vacuum pump. The removal of chloride ions in the filtrate was confirmed by the silver nitrate test. Then it was transferred to a glass lining with 250 ml of glycol-ethylene in a stainless-steel pressure vessel (Watlow series model PARR 4843). This was heated to a temperature of 200 $^{\circ}$C and maintained for 6 hours at a constant pressure of 60 psi. After 6 hours

the system was allowed to cool down slowly to room temperature. The dark brown magnetic powder was separated from glycol-ethylene by filtering. It was then washed with deionized water, and ethanol, and then dried in an infra-red lamp of 250 W for 2 hours. The product was recovered and homogenised by a pastel and agate mortar as illustrated in **Fig 3.1**.

Figure 3. 1: Illustration of the synthesis method. Source?

3.3 MATERIALS CHARACTERISATION

The samples of $MgCe_xFe_{2-x}O_4$ where x= 0.0, 0.05, 0.1, 0.2 were subjected to different characterisation methods, namely: XRD for structural properties; Mössbauer for magnetic properties; SEM to investigate surface morphology, microstructural analysis, and chemical composition; HRTEM to analyse the internal structure of materials to get detailed information regarding the structure, shape, size, and crystalline behaviour of the particle; XPS to analyse

the composition, elemental surface states, chemical and electronic states within a material; PL to study energy levels and to extract valuable information such as donor and acceptor states, purity and surface defect states and induced defect states within the band gap of the material; BET for the measurements of the specific surface area of materials. All these techniques are explained in this section.

3.3.1 X-Ray Diffraction (XRD)

An X-Ray diffractometer was employed in this study to investigate the structural properties, the orientation of a single grain, phase structure and composition, crystallite size, and lattice parameters of the synthesised nano ferrites. This method is based on recording the scattered intensity of x-ray beams hitting a sample as a function of incidence and scattering angle, polarisation, and wavelength or energy. The typical x-ray diffractometer setup is shown in **Fig. 3. 2.**

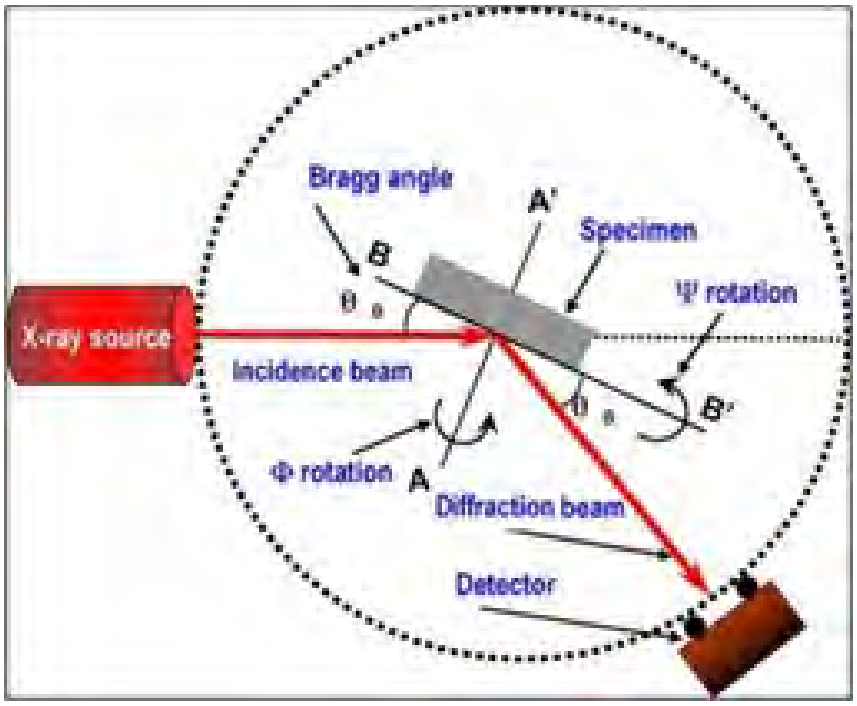

Figure 3. 2: Schematic diagram of an X-ray diffractometer **[1]**.

X-ray diffractometers comprise three essential components: an x-ray source, a sample holder, and an x-ray detector. X-rays are created in a cathode ray tube by warming up a filament to

produce electrons, then applying a large potential difference between the cathode (filament) and anode (metal target), which causes electrons to accelerate at a high speed towards the target metal and collide with it. When electrons have sufficient energy to dislodge the inner shell electrons of the target material, characteristic X-ray spectra are produced. These spectra comprise a few segments, the most widely recognised being K_α and K_β. Kα comprises $K_{\alpha 1}$ and $K_{\alpha 2}$. These K_α X-rays are collimated and directed on the sample. When the sample and detector are rotated, the intensity of the reflected X-rays is recorded. When the geometry of the incident X-rays impinging on the sample satisfies Bragg's law, the reflected X-rays from different planes in the crystal interfere with each other, as illustrated in **Fig. 3. 3**.

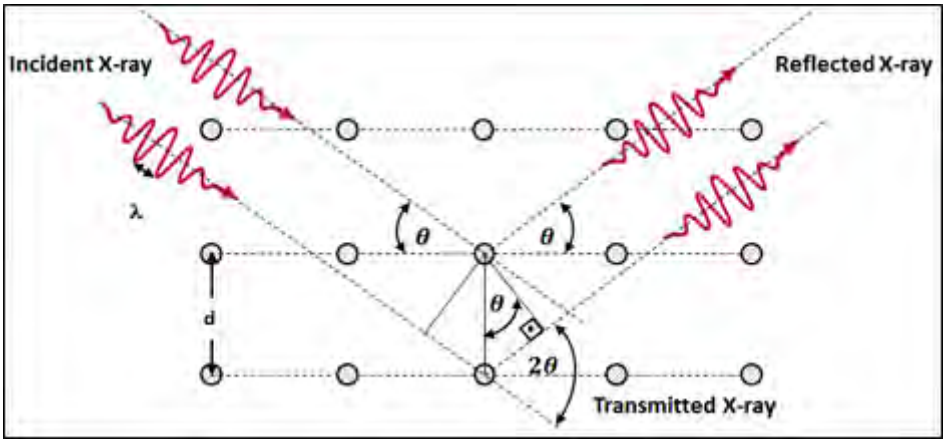

Figure 3. 3: Diffraction patterns according to Bragg's law **[2]**.

Bragg's equation describes the condition of constructive interference in x-rays scattered from atomic planes of a crystal as follows:

$$n\lambda = 2d\sin\theta \qquad \text{Eq.....3. 1}$$

where is an integer, λ is the wavelength of the characteristic x-rays, d is the lattice interplanar spacing of the crystal, and the angle between the radiation and the atomic planes, known as Bragg's angle. When the conditions for constructive interference are met, a diffraction pattern is produced. In a diffraction pattern, X-ray intensities are recorded as a function of the 2θ angle.

Plotting the intensities and positions (2θ angles) of the resultant diffracted peaks of radiation produces a pattern, which is a distinctive feature of the material being studied. In this study, measurements were performed in the range of 10° to 80° at a scan rate of 0.3° per minute and step size of 0.05° using a Bruker Advance D8 measuring instrument. The data were plotted using Origin 8.5 software. Peak analysis and indexing were done with the aid of a database of the Joint Committee on Powder Diffraction Standards (JCPDS Card No 36-0398). Then the crystalline size of nano ferrites was calculated using the Scherrer equation

$$D_{khl} = \frac{K\lambda}{\beta Cos\theta} \qquad \text{Eq.....3. 2}$$

where D_{khl} is the average crystalline size, K is the shape factor, λ is the x-ray wavelength(Cu Kα = 1.542 Å), β is the full width at half maximum in radians and θ is the Bragg's angle **[1]**

3.3.2 Scanning Electron Microscopy (SEM)

Scanning electron microscopy is the most generally used technique to investigate surface morphology, microstructural analysis, and chemical composition. The SEM scans the surface of the specimen with a highly focused beam of electrons and produces the image. The following six components are the main components of an SEM: Electron column, Scanning system, Detectors, Display, Vacuum system, and Electron beam controls.

An electron gun and at least two or more electromagnetic lenses operating in a vacuum are the components of the electron column. In an electron gun, electron beams are produced, and free electrons are excited with an energy range between 1 keV - 40 keV. The purpose is to focus and create a small electron probe on the specimen surface. The interaction of electrons with the specimen surface is determined by the probe diameter range between 1 nm - 1 μm. Scanning coils produced an image when an electron beam is focused and scanned across the specimen surface. Each point on the specimen surface that is struck by the accelerated electrons emits a signal in the form of electromagnetic radiation.

Figure 3. 4: Image of the University of Zululand's Field Emission Scanning Electron Microscope.

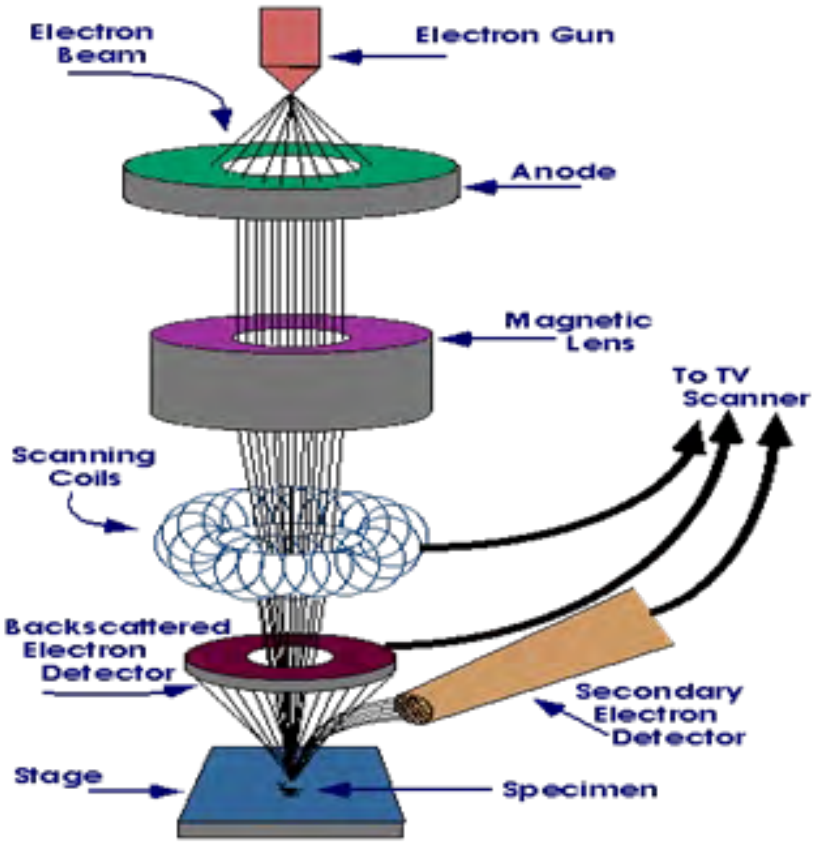

Figure 3. 5: Schematic diagram of SEM **[3]**.

Generally, the most selected signals are backscattered electrons and secondary electrons. The mentioned signals are collected in a backscattered electron detector and a secondary electron detector respectively. The collected signals are displayed on one of the TV screens in the form of an image. However, the advantage of SEM is the clear image produced like that of a normal photo. The exterior part of an SEM and the schematic diagram are shown in **Fig. 3. 4** and **Fig. 3. 5** respectively. For this study, images of the powder's surface morphology and particle size were captured using a scanning electron microscope (SEM, Carl ZEISS Sigma VP-03-67) with the Energy Dispersive X-ray Spectroscope (EDS), which detects elements' composition in a material.

3.3.3 Transmission Electron Microscopy

Transmission electron microscopy (TEM) is one of the important techniques used to analyse the internal structure of materials to get detailed information regarding the structure, shape, size, and crystalline behaviour of the particle. In the TEM instrumentation, the electron beam from the gun is transmitted via the material, creating an image on a fluorescence screen. High-resolution TEM (HRTEM) is slightly more advanced and uses a different methodology than other types of TEM. In HRTEM the transmitted electrons interact with atoms in the material through elastic and inelastic scattering. Inelastically scattered electrons have a change in energy after they are transmitted through the sample, while elastically scattered electrons maintain their initial transmitted energy. These electrons leave the sample and move through the lenses of the microscope to form a high-resolution image, that can structurally characterise samples at an atomic level **[4]**. It is, therefore, a very useful technique in the study of all nanoscale structures. **Fig. 3.6** shows a schematic diagram of the HRTEM. This study images were recorded using a high-resolution transmission electron microscope (HR-TEM) JEOL 1400 system.

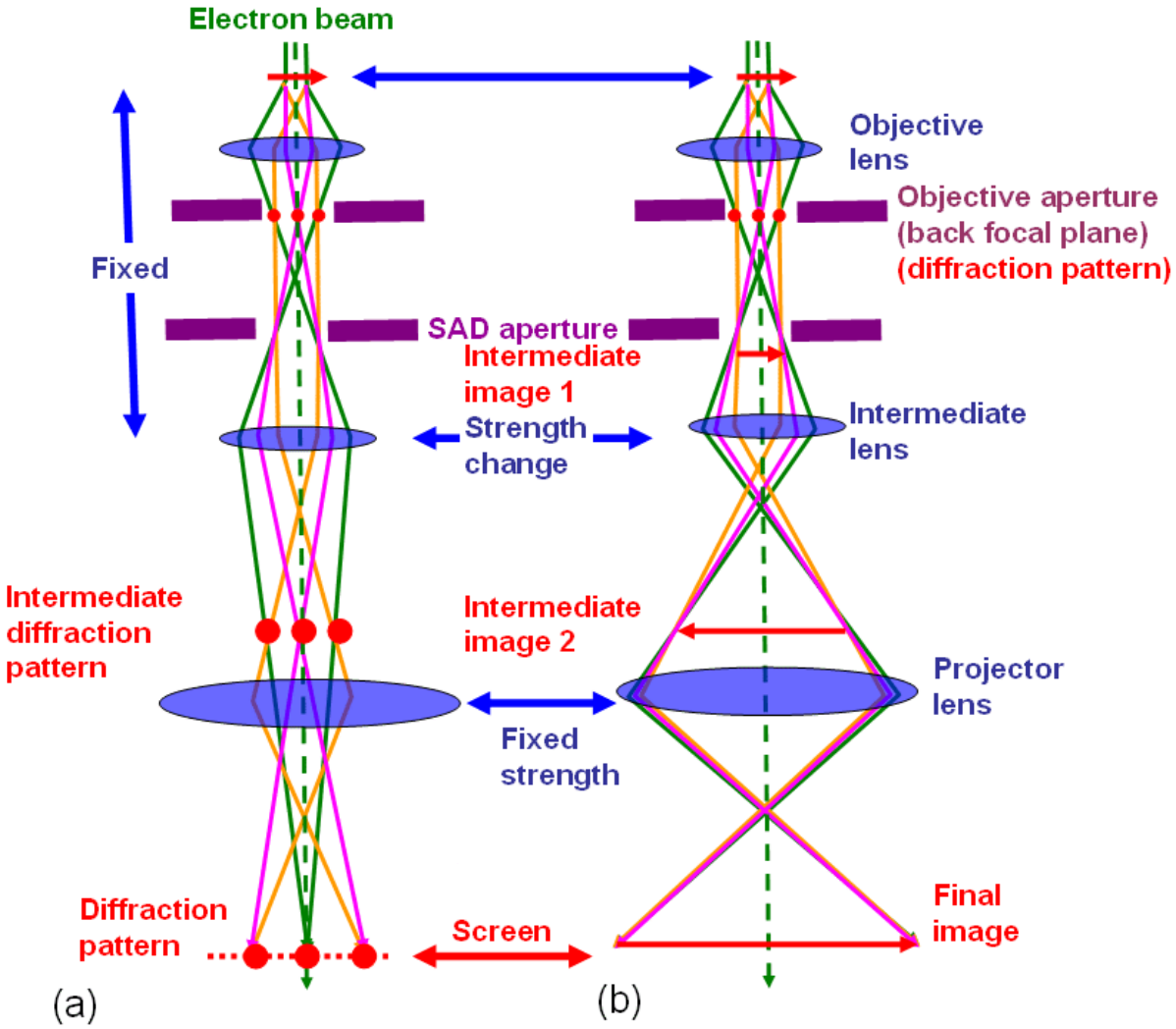

Figure 3. 6: Schematic representation of TEM, for (a) diffraction pattern viewing and (b) final image viewing **[5].**

3.3.4 X-ray Photoelectron Spectroscopy

X-ray photoelectron spectroscopy (XPS) is a technique used to analyse the composition, elemental surface states, and chemical and electronic states within a material. This technique was first reported in 1967 by Siegbahn **[6]** and this was based on the photoelectric effect, which was explained by Albert Einstein in 1905 **[7]**. The photoelectric effect is the ejection of electrons from a metal surface when it is irradiated by light. Einstein predicted that light is not a wave propagating in a space, but packets of waves related to photons with energy (E) which

is given by E = hν where h is the Planck constant and ν is the frequency. For an electron to be ejected, the photon must have an energy bigger than the work function (ϕ) of a material otherwise no electron will be ejected. Therefore, the photoelectric effect equation can be written as follows:

$$E_k = h\nu - \phi \qquad \text{Eq.....3. 3}$$

In XPS the sample is bombarded with x-rays of energies lower than 6 keV, and then the kinetic energy of ejected electrons is measured and analysed. The binding energy (BE) of electrons can be calculated as

$$BE = h\nu - E_k - \phi \qquad \text{Eq.....3. 4}$$

where $h\nu$ is the energy of photons known or measured, E_k the kinetic energy of ejected electrons as measured by the instrument and ϕ is the work function of the sample **[8]**.

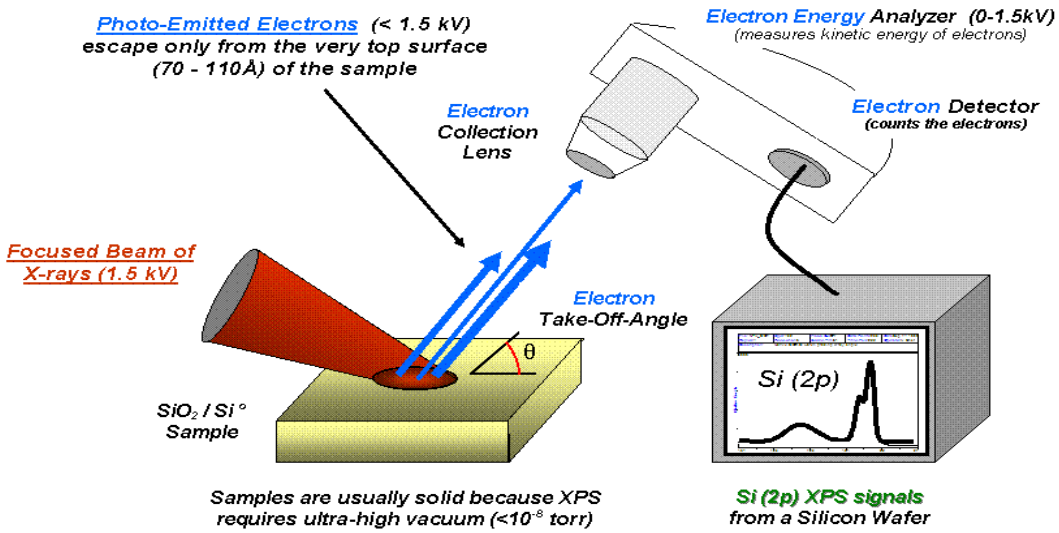

Figure 3. 7: Schematic setup of XPS **[8]**. **Source?**

The binding energy is measured with respect to the material fermi level not with respect to the vacuum, which is why the work function is included in equations. Characteristic spectral peaks observed from XPS spectra are notated by the element and orbital from which they were

ejected. For example, “O 1s” describes electrons emitted from the 1s orbital of an oxygen atom. **Fig. 3.7** shows the basic setup of XPS.

3.3.5 Photoluminescence (PL)

Photoluminescence (PL) is the spontaneous emission of light from a material after optical excitation. It is a powerful technique mainly used to study energy levels and to extract valuable information such as donor and acceptor states, purity and surface defects states and induced defects states within the band gap of the material. **Fig. 3.8** shows the PL schematic setup.

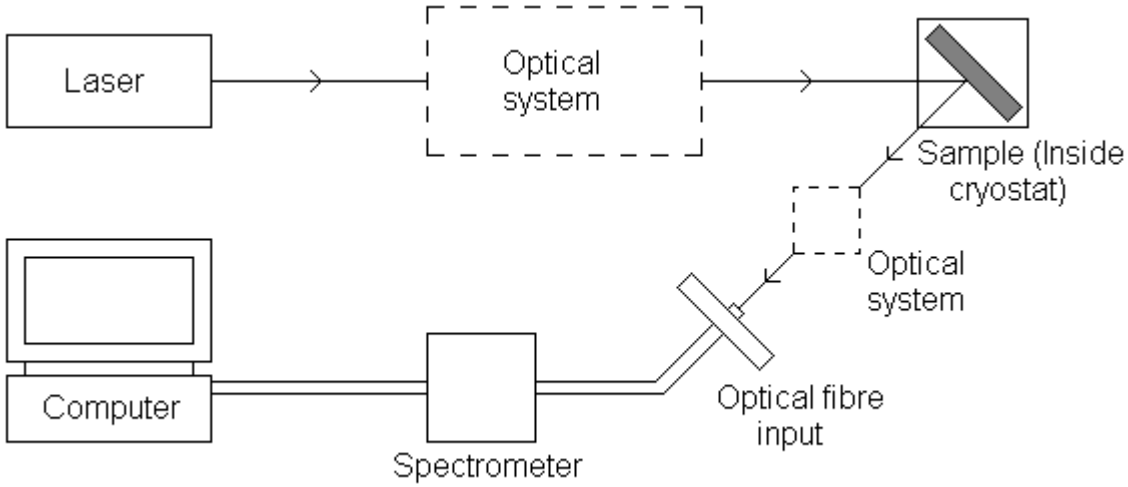

Figure 3. 8: Schematic setup of the Photoluminescence spectrometer **[9]**.

During PL measurements, a beam of light with a wavelength close to the bandgap of a sample is shone onto the sample inside the cryostat, to ensure that measurements are taken at low temperatures. The light is absorbed and directs excess energy to the material in a process called photo-excitation **[10]**. After light absorption electrons move from the valence band into the conduction band, but this only happens if the incident light has an energy greater than the bandgap energy. An electron that has been excited above the conduction band of a material will eventually fall and recombine to the hole that has been excited below the valance band after losing some energy by releasing a phonon to the lowest available non-radiative energy level. The emitted light is directed into a fibre optic cable and then into a spectrometer. A filter may

be placed in front of the fibre input to remove any incidental laser light. Inside the spectrometer, a diffraction grating diffracts different wavelengths in different directions towards an array of photodetectors that measure the intensity of each wavelength component. The digital information is interpreted by the computer, which can display a PL spectrum. The spectrum indicates the relative intensities of light of different wavelengths entering the detector. The efficiency of the photoluminescence signal is determined by the nature of optical excitation, and properties of the material, i.e., radiative, and non-radiative recontamination and defects. in this study, the photoluminescence (PL) spectra were excited at room temperature with a continuous helium cadmium laser of wavelength 325 nm chopped at 120 Hz and collected using a Horiba iHR320 spectrometer with entrance and exit slits set to 250 mm and a photomultiplier tube detector (R9943-02) operating at 1300 V, linked to a lock-in amplifier.

3.3.6 Brunauer-Emmett-Teller Spectroscopy

Brunauer-Emmett-Teller (BET) spectroscopy together with related theory aims to explain the adsorption of gas molecules on a solid surface and serves as the basis for an important analysis technique for the measurement of the specific surface area of materials. BET theory applies to systems of multilayer adsorption, and usually utilizes probing gases that do not chemically react with material surfaces as adsorbates to quantify specific surface area. Nitrogen is the most employed gaseous adsorbate used for surface probing by BET methods. For this reason, standard BET analysis is most often conducted at the boiling temperature of N_2. Further probing adsorbates are also utilised, even though with lower frequencies, allowing the measurement of surface area at different temperatures and measurement scales. These include argon, carbon dioxide, and water. Specific surface area is a scale-dependent property, with no single true value of specific surface area definable, and thus quantities of the specific surface area determined through BET theory may depend on the adsorbate molecule utilised and its adsorption cross-section**[11]**. A schematic setup of BET instrument is shown on **Fig. 3. 9.**

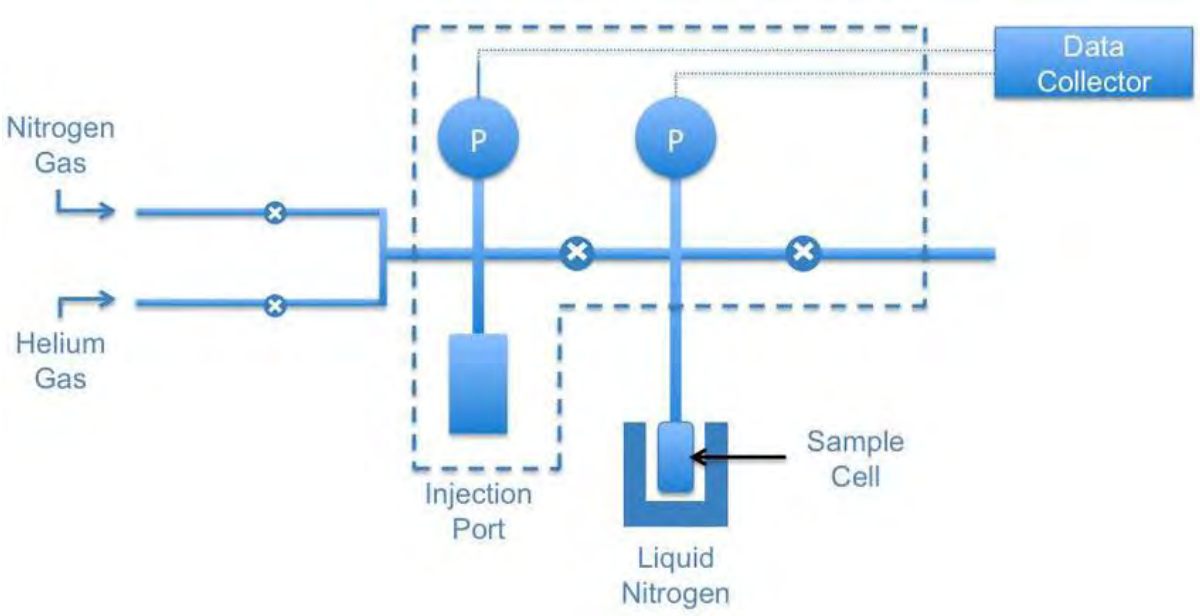

Figure 3. 9: Schematic diagram of the Brunauer-Emmett-Teller (BET) **[12]**.

In this study, Nitrogen adsorption-desorption isotherms and Brunauer-Emmett-Teller (BET) surface area studies were performed using a Micromeritics TRISTAR 3020 surface area analyser.

3.3.7 Magnetic properties measurements

Magnetic properties in ferrites make them useful in various applications. These magnetic properties are determined by the interactions between magnetic moments which are dependent on the position of metal cations in the crystal structure **[13]**. The interaction of the cations is mediated by the oxygen ions which also insulate them from each other, thus resulting in high resistivity as another important property of ferrites **[14]**. The interaction via the intermediary oxygen ions is referred to as super exchange interaction which is the source of magnetism in ferrites. Since the magnetic moments of the cations occupying the A and B sites are not equal, the strong super exchange interactions result in an anti-parallel arrangement with net non-zero magnetization**[15]**. This type of magnetic ordering is known as ferrimagnetism. This is like ferromagnetic order. Spontaneous ordering of the magnetic moments occurs below the Curie

temperature. In this study, magnetic measurements were done using a Mössbauer spectroscope and a Vibrating sample magnetometer.

(a) Mössbauer Spectroscopy

Mössbauer spectroscopy is a technique that is mainly used to detect the weak interactions between a nucleus and its surrounding materials **[16]**. Thus, scientists use these tiny energy changes to give precise information about the chemical, structural and magnetic properties of materials. Geologists use this technique in mineralogy to examine the valence states of iron atoms at lattice and interstitial sites. The technique is important for both research and applications. In 1957 Rudolf Mössbauer discovered the recoil-free emission and resonant absorption of gamma (γ) rays by atoms in a crystal **[17]**. This is known as the Mössbauer effect and serves as the basis for Mössbauer spectroscopy. The Mössbauer spectroscopy unit used for measurements in this study consisted of a 25 mCi 57Co source sealed in rhodium matrix, HALDER D 8110 transducer, LND 45431 detector, FAST ComTec pre-amplifier, CANBERRA 2011 linear amplifier, TUNNELEC TC-950 HV supply, HALDER MR-351 Mössbauer drive unit (MDU), an ORTEC model MCS-PCI card, and a desktop computer. The setup of the Mössbauer used in this study is shown in **Fig. 3.10**.

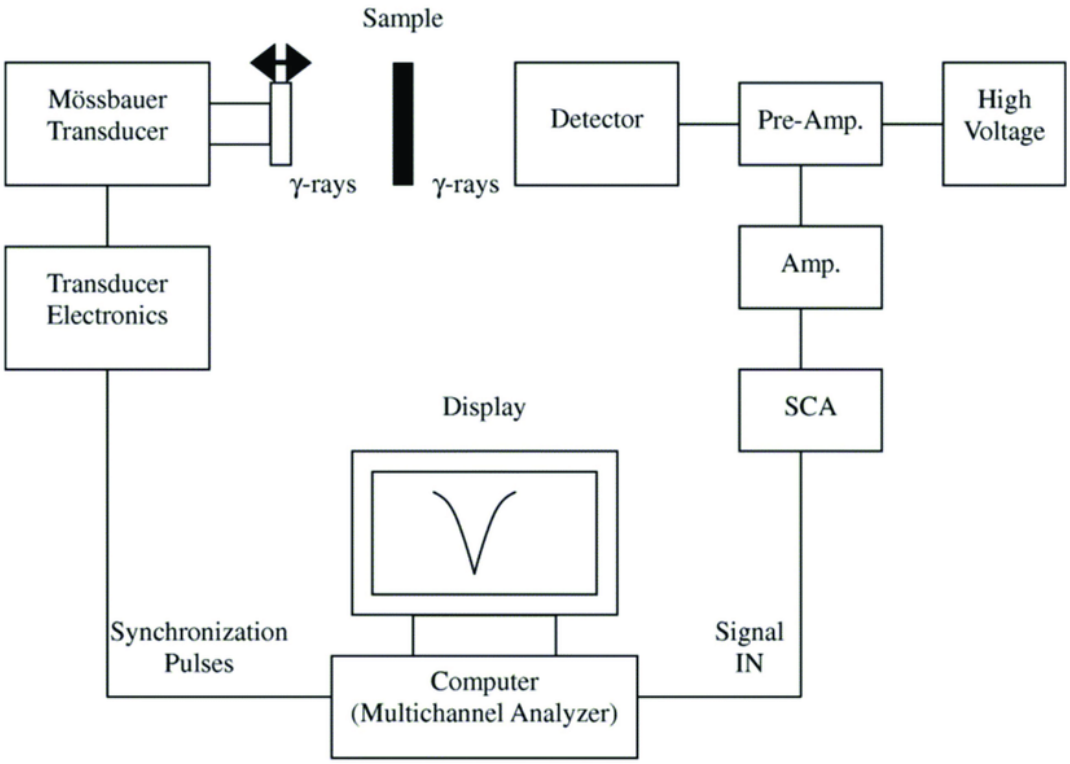

Figure 3. 10: A schematic diagram of the Mössbauer spectroscopy setup**[18]**.

(b) Vibrating Sample Magnetometer

A vibrating sample magnetometer (VSM) is commonly used to measure magnetisation. The magnetisation in materials is an important parameter to measure, as it provides crucial intrinsic information about the magnetic state of a materials. It also gives information on the nature of the interactions of the constituent magnetic moments **[19]**. The magnetisation is well determined under the influence of an external magnetic field. The role played by the external field is to align the magnetic moments of materials in the direction of the field. One important aspect is to study how the magnetisation of a material varies with temperature T or applied field B. In this study the Lakeshore VSM system consisted of an electromagnet, model 642 bipolar electromagnet power supply, model 450 gaussmeter, model 340 temperature controller, model 735 VSM controller, a NESLAB ThermoFlex 2500 chiller, National Instruments IEEE-488 interface card and a desktop computer. The components were connected to the interface

card by PCI-GPIB cables. All the components were powered through an Eaton 9355 Uninterrupted Power Supply (UPS) system to avoid data loss and abrupt shutdown of the VSM during power failure. Windows interface software was used to control the components and monitor the status of the equipment during measurement. The VSM was calibrated by a standard nickel sphere of known saturation magnetisation of 54.7 emu/g. Then measurements were done in the field of -15kOe to 15kOe.

3.4 GAS SENSING TESTING

A KENOSISTEC KSGAS6S Italy gas sensing technique set-up was used in this study to investigate gas sensing properties of the nanostructures. The instrument is shown in **Fig. 3.11.**

Figure 3. 11: KSGAS6S test system for gas sensors at UNIZULU.

The system consist of a sensing chamber with sample stages, two thermostatic baths, an air mixer and a dry air inlet carrying dry air into the mixer, four different gas inlets, and mass flow controllers to control the amounts of gases reaching the chamber (with the first supplying wet

air into the mixer during humidity measurements and the second being for volatile gas measurements), KEITHLEY heater that supplies voltage across the sample and Pico ammeter for the conductance measurement, gas inlets and outlets including a vent outlet.

3.5 SENSOR FABRICATION AND MEASUREMENTS

To study the gas sensing properties, samples were dispersed in ethanol and sonicated for 2 h. Then drop casting was performed onto alumina substrates pre-printed with platinum electrodes on the top surface. These sensors were dried at 120 °C to remove any organic residuals. One sensor at a time was placed inside an airtight chamber with electrical and gas feeds for sensing measurements using a KS026K16 (KENOSISTEC model, Italy) gas testing system at different operating temperatures (i.e. 25 °C, 75, 100, 125, 150, 175, 225 and 275 °C) under constant applied voltages (0.1, 0.5, 1.0, 3.0, 5.0, 7.0 V) across the sensor. The concentrations of the target gases which were all bought from NMISA (acetone, methanol, p-xylene, ethylbenzene, toluene, and benzene) at 5, 10, 20, 50, 80, and 100 ppm concentration and operating temperature of 225 °C within the chamber were regulated by monitoring the flow rate ratio of the dry-air and argon gas to the target gas. A dry-air atmosphere (79% N_2 and 21% O_2) was used to conduct dilution of the gas measurements and as well as a carrier gas. As for the gas sensing measurement in inert or reduced oxygen environment, argon was used as a carrier gas to dilute the acetone gas. The gas sensing measurements were conducted in dry ambient (0.1 %RH) and in the presence of relative humidity (50 %RH maximum). The change in the sensor resistance of the device was quantified using a Keithley 6487/E Pico ammeter/voltage source meter. The electrical gas response (S) of the sensor was calculated using equation 2.6.

3.5 REFERENCES

[1] Thuriot-Roukos, J., Bennis, M., Heuson, E., Roussel, P., Dumeignil, F. and Paul, S., Design of a multi-well plate for high-throughput characterization of heterogeneous catalysts by XRD, FT-IR, Raman and XRF spectroscopies. RSC advances, 2018, 8(71), pp.40912-40920.

[2] G. Artioli, X-ray Diffraction (XRD), in: A.S. Gilbert (Ed.), Encyclopedia of Geoarchaeology, Springer Netherlands, Dordrecht, 2017, pp. 1019-1025.

[3] Walock, Michael J. Nanocomposite coatings based on quaternary metal-nitrogen and nanocarbon systems. The University of Alabama at Birmingham, 2012.

[4] J. Davis, What is High-Resolution TEM (HR-TEM), AZoLifeSciences, www.azolifesciences.com, 2021.

[5] Y. Liao, Practical electron microscopy and database, An Online Book (2006).

[6] G. Axelson, U. Ericson, A. Fahlman, K. Hamrin, J. Hedman, R. Nordberg, C. Nordling, K. Siegbahn, New approach to structure studies in organic chemistry, Nature 213 (1967) 70-71.

[7] A. Einstein, The photoelectric effect, Ann. Phys 17 (1905) 4.

[8] Introduction to x-ray photoelectron spectroscopy, J. Vac. Sci. Technol A 38 (2020).

[9] Gfroerer T., H. Photoluminescence in Analysis of Surfaces and Interfaces. In Encyclopaedia of Analytical Chemistry; Meyers, R. A., Ed.; John Wiley and Sons Ltd.: Chichester,pp 9209-9231, (2000)

[10] J.A. Weil, J.R. Bolton, Electron paramagnetic resonance: elementary theory and practical applications, John Wiley & Sons2007.

[11] M. Nasrollahzadeh, M. Atarod, M. Sajjadi, S.M. Sajadi, Z. Issaabadi, Chapter 6 - Plant-Mediated Green Synthesis of Nanostructures: Mechanisms, Characterization, and Applications, in: M. Nasrollahzadeh, S.M. Sajadi, M. Sajjadi, Z. Issaabadi, M. Atarod (Eds.), Interface Science and Technology, Elsevier 2019, pp. 199-322.

[12] Majumdar, Pavel. "Development of Electrodes for Artificial Photosynthetic System." PhD diss., Indian Institute of Engineering Science and Technology, Shibpur, 2015.

[13] Pardavi-Horvath, Martha. "Microwave applications of soft ferrites." Journal of Magnetism and Magnetic Materials 215 (2000): 171-183.

[14] Chakrabarty, S., A. Dutta, and M. Pal. "Enhanced magnetic properties of doped cobalt ferrite nanoparticles by virtue of cation distribution." Journal of Alloys and Compounds 625 (2015): 216-223.

[15] P.P. Masina, Magnetic properties of Mg_{1}-xZnx$Fe_{2}O_{4}$ nanoferrites and tetracycline-ferrite nanocomposites, 2013.is this ref complete?

[16] Murad, Enver, and John Cashion. Mössbauer spectroscopy of environmental materials and their industrial utilization. Springer Science & Business Media, 2011.

[17] Potenziani, E., and John A. Kosinski. "An examination of the Mossbauer effect as the basis of a time/frequency standard." In Proceedings of the 2004 IEEE International Frequency Control Symposium and Exposition, 2004., pp. 790-794. IEEE, 2004.

[18] M.R. Zamani Kouhpanji, B. Stadler, A Guideline for Effectively Synthesizing and Characterizing Magnetic Nanoparticles for Advancing Nanobiotechnology: A Review, Sensors 20 (2020) 2554.

[19] Ruta, Sergiu, Ondrej Hovorka, Pin-Wei Huang, Kangkang Wang, Ganping Ju, and Roy Chantrell. "First order reversal curves and intrinsic parameter determination for magnetic materials; limitations of hysteron-based approaches in correlated systems." Scientific Reports 7, no. 1 (2017): 45218.

CHAPTER 4

STRUCTURAL AND SURFACE ANALYSIS

4.1 INTRODUCTION

This chapter deals with the structure and magnetic, optical, and surface properties of the Cerium substituted Magnesium Nano-ferrites prepared by the pressurised hydrothermal chemical process. The above mentioned materials' properties were conducted by X-ray diffraction, Scanning Electron Microscopy, High-Resolution Transmission Electron Microscopy, X-ray Photoelectron Spectroscopy, Brunauer-Emmett-Teller, Vibrating Sample Magnetometer, Photoluminescence Spectroscopy and Mössbauer.

4.2. RESULTS AND DISCUSSION

4.2.1 X-Ray Diffraction

The X-ray diffraction (XRD) patterns of the as-synthesised $MgCe_xFe_{2-x}O_4$ with $x \leq 0.4$ are presented in **Fig. 4.1**. The observed hkl diffraction peaks, (220), (311), (400), (422), (511), (440), and (533) accord well with the formation of spinel with a cubic crystallographic structure. They match well with JCPDS card no. 36-0398, confirming the formation of pure face-centred cubic structure of $MgFe_2O_4$ phase with space group Fd3m **[1, 2]**.

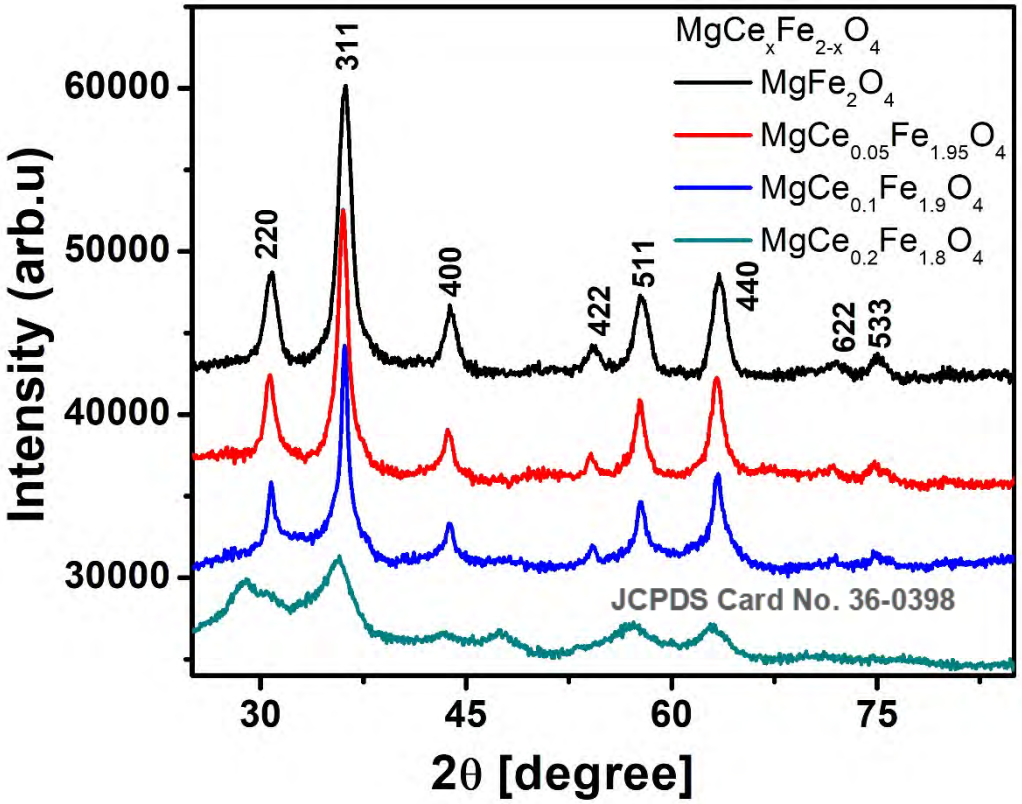

Figure 4. 1: The X-ray diffraction patterns of the Ce substituted (x = 0, 0.05, 0.1, 0.2) Magnesium Ferrites doped with Ce in the octahedral site.

At lower *x* content of Ce, no other foreign peak/s was detected, which indicates the high phase purity of $MgFe_2O_4$ ferrite up to $x = 0.1$. However, at $x = 0.2$, a peak at about $2\theta = 28°$ was observed and the spinel high purity is significantly reduced. This suggests the formation of secondary phases probably corresponding to CeO_2. The average crystallite size (D_{311}) of $MgCe_xFe_{2-x}O_4$ nanoferrites was estimated using Scherer's equation **[3]** and the dominant peak (311). The crystallite sizes of 7, 10, 15 and 3 nm were recorded for Ce composition of $x = 0$, 0.05, 0.10, and 0.2, respectively. The estimated crystallite size showed an initially increasing trend upon the addition of Ce in the octahedral site substituting Fe atom but decreased significantly for the sample having $x = 0.2$, as shown in **Fig. 4.2(a)**. It should be noted that the (311) dominant plane did not have any significant shift during Ce substitution, as observed on the enlarged view of XRD in **Fig. 4.2(b)**. This trend of increasing $D_{(311)}$ could be attributed to the decreasing of the full-width-at-half-maximum (FWHM) of the peaks, particularly the (311)

peak. This is more prominent for the x = 0.2 sample. Elayakumar et al. **[4]** observed a general decreasing trend in the crystallite sizes of $CuCe_xFe_{2-x}O_4$ upon increasing the cerium ions ($0 \leq x \leq 0.5$). The 311 dominant peaks shifted to higher 2θ values because of cerium substitution. However, the spinel maintained its crystalline purity and no reduction of XRD intensity was observed. The cell volume, lattice dislocation and strain were reduced with the cerium element substitution up to x = 0.1, thereafter a significant increase was observed at x = 0.2. In contrast, the opposite was observed for $CoNd_xCe_xFe_{2-x}O_4$ spinel ferrites for $0 \leq x \leq 0.2$ range **[5]**. All parameters deduced from XRD results are presented in **Table 4.2**.

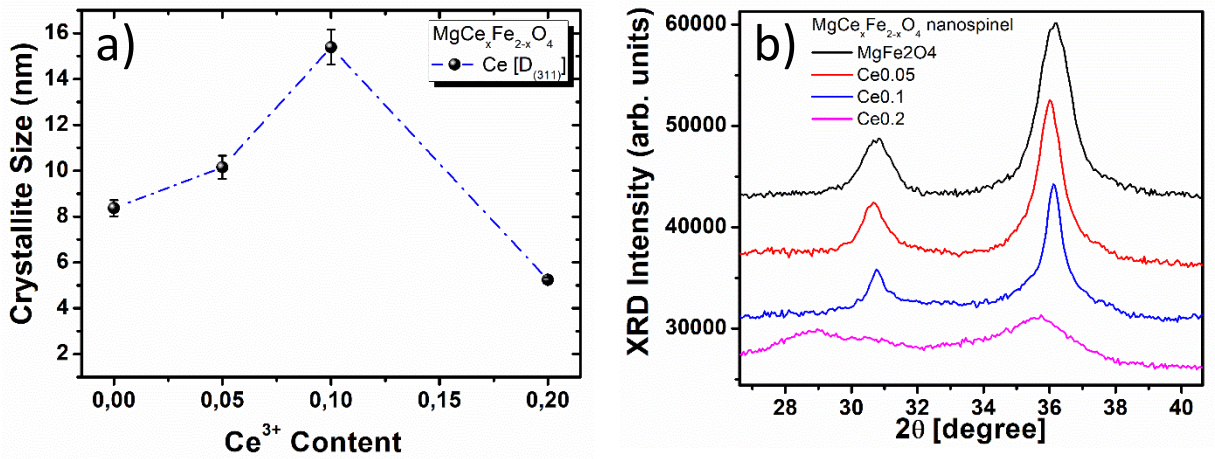

Figure 4. 2: (a) Crystallite sizes estimated from the 311 dominant peak and (b) enlarge XRD view of 311 peaks of $MgCe_xFe_{2-x}O_4$ Nano ferrites.

Table 4. 1: Summary of Crystallite Size (D), Lattice parameter (a), Unit Cell Volume (V), X-ray diffraction density (ρ), Dislocation density (δ) and Lattice strain (ε)

Sample	**Crystallite size (D_{311}) nm**	**Lattice parameter (a) Å**	**Unit cell volume $(Å)^3$**	**XRD density (ρ) g/cm^3**	**Dislocation density (δ) $(x10^{-3}/nm^{-2})$**	**Lattice strain (ε) $x10^{-3}$**
$MgFe_2O_4$	8.37±0.35	8.320	575.9	4.61	14.3	3.0
$MgCe_{0.05}Fe_{1.95}O_4$	10.15±0.51	8.392	591.1	4.59	9.70	2.8
$MgCe_{0.1}Fe_{1.9}O_4$	15.39±0.70	8.351	582.6	4.75	4.21	2.3
$MgCe_{0.2}Fe_{1.8}O_4$	5.24±0.10	8.339	579.9	4.97	36.4	5.9

4.2.2 High Resolution Transmission Electron Microscopy

As part of internal structural analysis, High-Resolution Transmission Electron Microscope (HR-TEM) measurements were performed on as-prepared magnesium doped Nano-Ferrites. **Fig 4.3(a-h)** shows HR-TEM images of $MgCe_xFe_{2-x}O_4$ nano-ferrites with different Ce dopant concentrations. The insets of **Fig 4.3** are the corresponding selected area electron diffraction patterns (SAED). The inter-planar d-spacings could be calculated from the diffraction fringes and the value of 0.249 nm for the most prominent ring could be indexed to the (311) crystalline planes of the $MgFe_2O_4$ spinel ferrite. The series of the SAED spots in the rings of Fig. 4.3 insets confirmed the crystalline structure of the magnesium-based spinel ferrite samples. However, the more diffuse rings of the highly substituted $MgCe_{0.2}Fe_{1.8}O_4$ nano-ferrite (see **Fig. 4.2(g)**) suggests poor crystallinity and that the Ce atoms could no longer be incorporated into the $MgFe_2O_4$ structural matrix, instead forming secondary islands corresponding to other phases. **Fig. 4.3(h)** shows different lattice fringes with d-spacing that could be indexed to CeO_2 and α-Fe_2O_3 phases. This is consistent with the XRD analysis **(see Fig. 4.1)** showing poor single crystalline corresponding to the magnesium spinel ferrite as the Ce is increased.

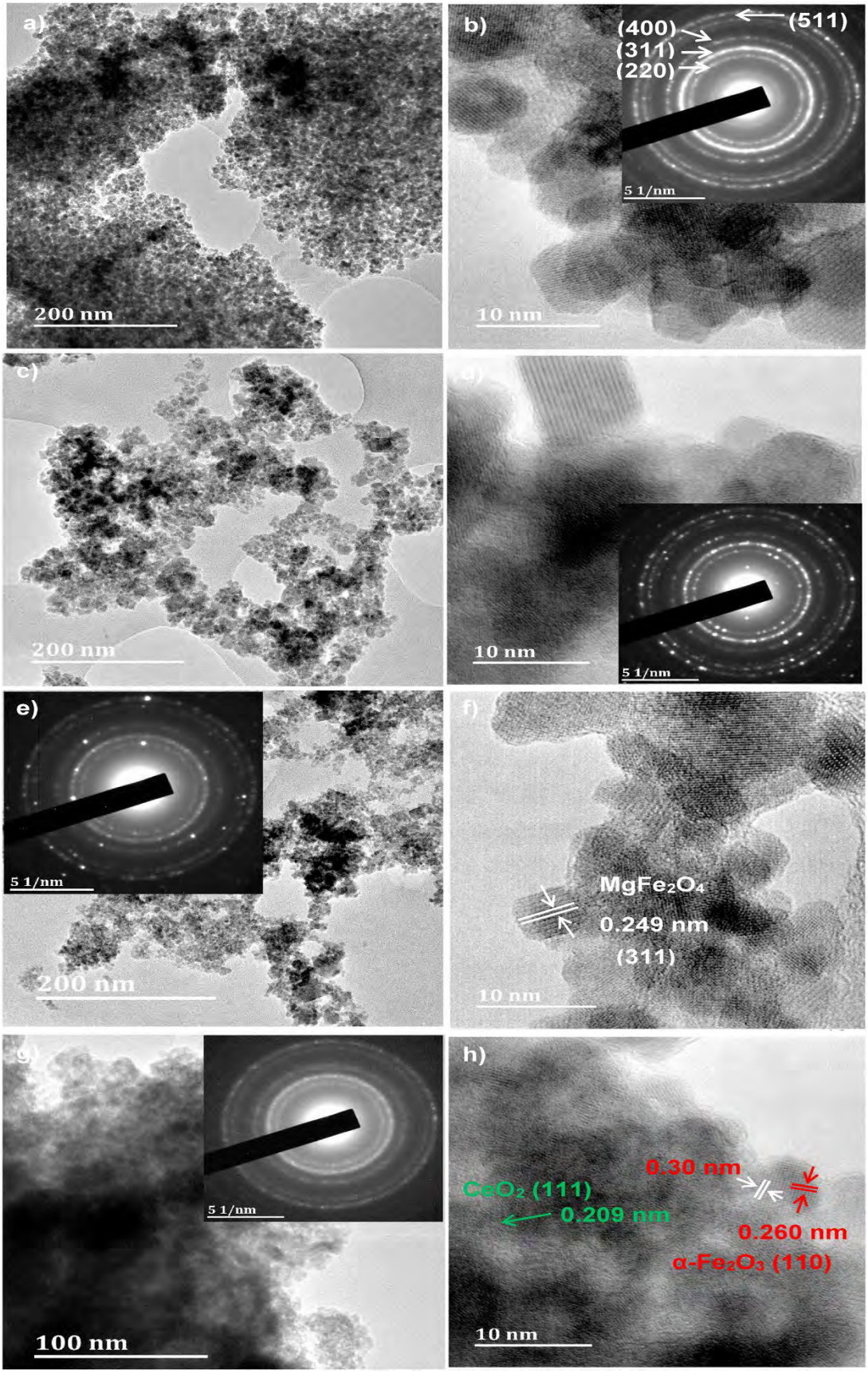

Figure 4. 3: HRTEM images of $MgCe_xFe_{2-x}O_4$ nano-ferrites with different Ce dopant concentrations **(a - b)** x=0, **(c - d)** x=0.05, **(e - f)** x=0.1, and **(g - h)** x=0.2. The insets are the corresponding selected area electron diffraction patterns.

4.2.3 Scanning Electron Microscopy

The surface morphologies of these MgCexFe2-xO4 Nanoferrites are presented in **Fig. 4.4(a-d)**. where **(a)** is an undoped magnesium ferrite ($MgFe_2O_4$), **(b)** $MgCe_{0.05}Fe_{1.95}O_4$, **(c)** $MgCe_{0.1}Fe_{1.9}O_4$ and **(d)** $MgCe_{0.2}Fe_{1.8}O_4$.

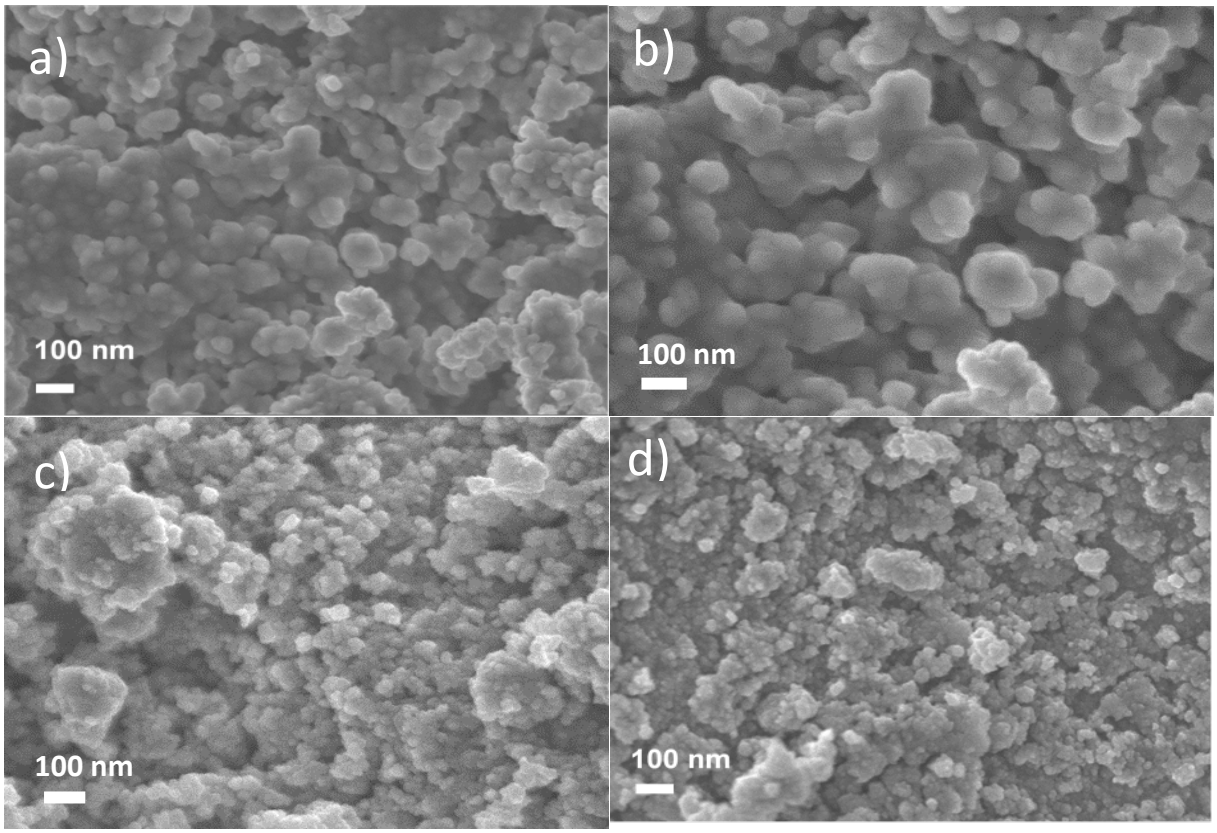

Figure 4. 4: SEM images of the $MgCe_xFe_{2-x}O_4$ samples with **(a)** x=0, **(b)** x=0.0.5, **(c)** x=0.1 and **(d)** x=0.2.

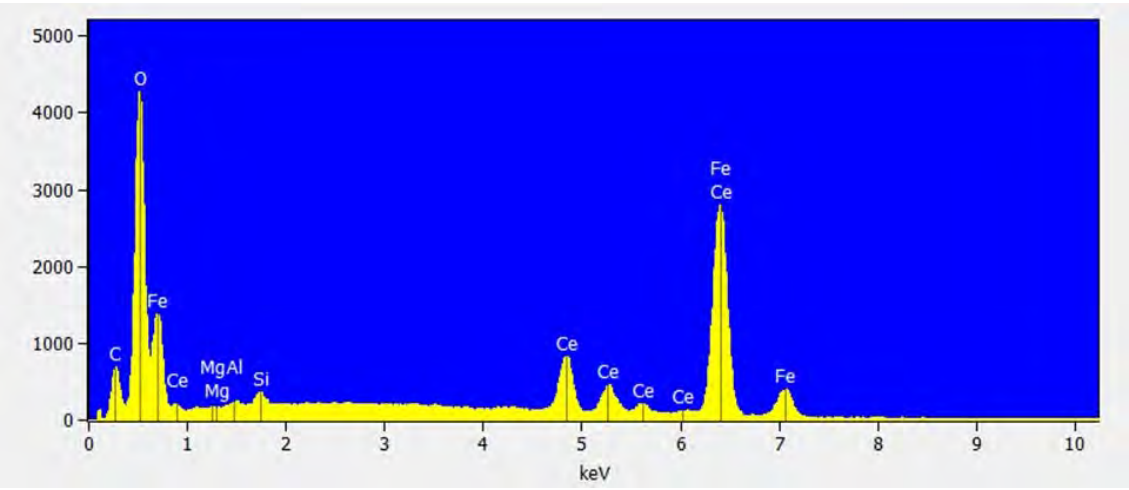

Figure 4. 5: The energy dispersive X-ray (EDX) measurements performed on $MgCe_{0.2}Fe_{1.8}O_4$ nanoferrites.

Both the undoped or unsubstituted and less Ce doped, $MgFe_2O_4$ (**Fig. 4.4a**) and $MgCe_{0.05}Fe_{1.95}O_4$ (**Fig. 4.4b**), respectively, show small spherical nanoparticles that appear compact and inter-connected. Increasing the Ce doping by x = 0.1 and 0.2 (see **Fig. 4.4(c &d)**) changed the morphology to small spherical particles that look fine and separated. The Ce doping therefore had a significant effect on the morphology and size of the particles. The quantitative measurements were performed on the samples using the Energy Dispersive X-ray (EDX). The elemental composition spectrum of $MgCe_{0.2}Fe_{1.8}O_4$ sample is presented in **Fig. 4.5**. The figure confirms the presence of Iron (Fe), Oxygen (O), Cerium (Ce) and Magnesium (Mg) as expected.

4.2.4 X-ray Photoelectron Spectroscopy Measurements

To investigate the sensor's surface composition and valence/oxidation state of the elements, X-ray Photoelectron Spectroscopy measurements for the Ce-doped magnesium Nano-ferrites were performed. Firstly, the survey measurements were conducted to identify the elemental composition present in each sample (spinel ferrites). Indeed, the survey spectra confirm the existence of C, Mg, Fe, and O elements in the pure undoped spinel ($MgFe_2O_4$). However, introducing Ce in the spinels was confirmed by the existence of C, Mg, Ce, Fe, and O elements in the doped or substituted spinels. The C element was present in all the XPS measurements due to the adventitious C in the atmosphere and acted as a reference. The survey spectrum of undoped $MgFe_2O_4$ showing the existence of Mg, Ce, Fe, and O elements on the surface shown in **Fig. 4.6(a)** and **Fig. 4.6(b) – (e)** are the XPS spectra of Fe 2p, Mg 2p, O 1s and Ce 3d respectively. It should be noted that for undoped magnesium there is no cerium spectrum, therefore **Fig. 4.6** has **(a)** to **(d)** then the other with cerium has **(a)** to **(e)**. **Fig 4.7** present the XPS spectra for $MgCe_{0.05}Fe_{1.95}O_4$, **Fig. 4.8** spectra for $MgCe_{0.1}Fe_{1.9}O_4$ and **Fig. 4.9** spectra for $MgCe_{0.2}Fe_{1.8}O_4$

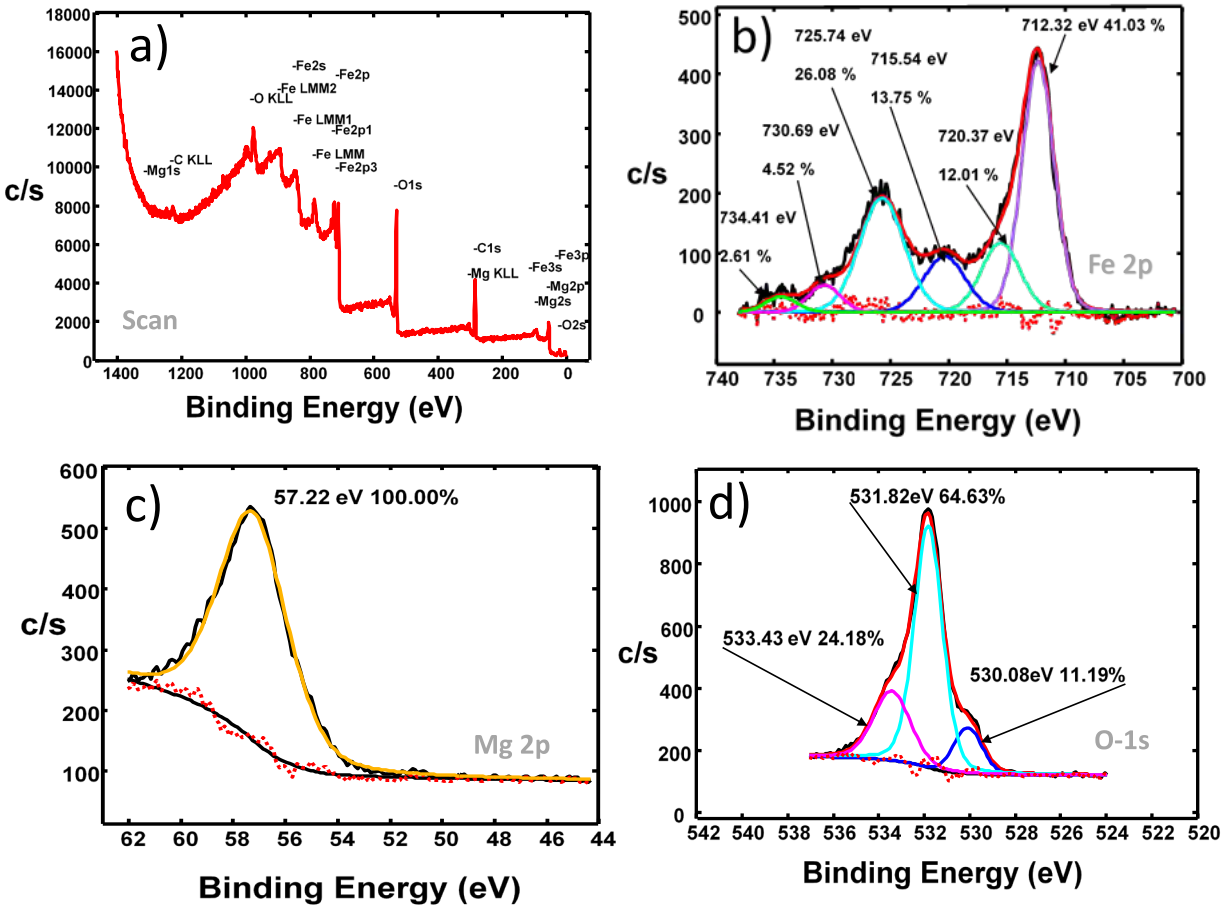

Figure 4. 6: An XPS spectra **(a)** Survey spectrum, **(b)** Fe 2d spectrum, **(c)** Mg 2p spectrum, and **(d)** O 1s spectrum for the $MgFe_2O_4$ nano-ferrite.

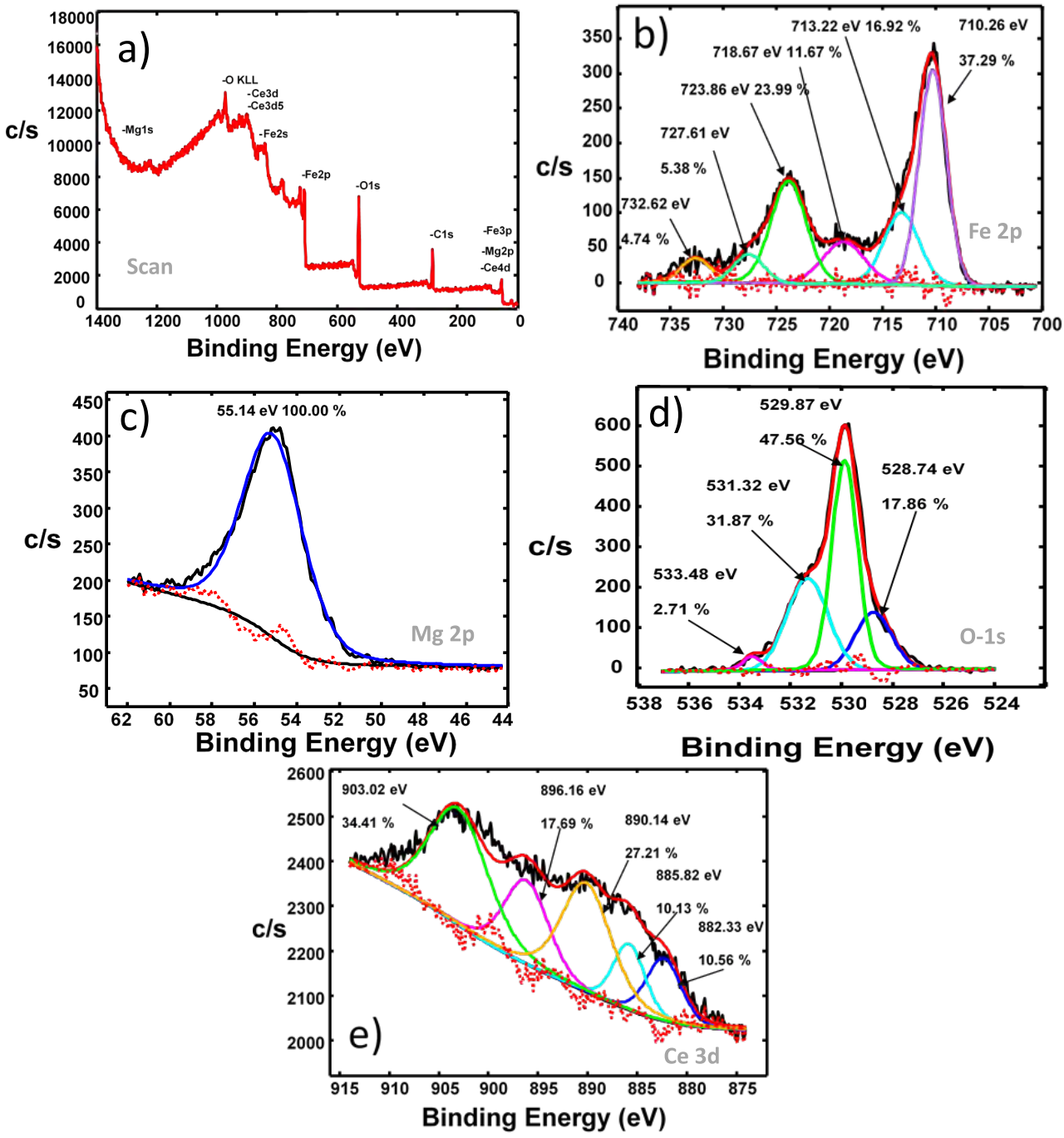

Figure 4. 7: An XPS spectra **(a)** Survey spectrum, **(b)** Fe 2d spectrum, **(c)** Mg 2p spectrum, **(d)** O 1s spectrum and **(e)** Ce 3d spectrum for the $MgCe_{0.05}Fe_{1.95}O_4$ nano-ferrite.

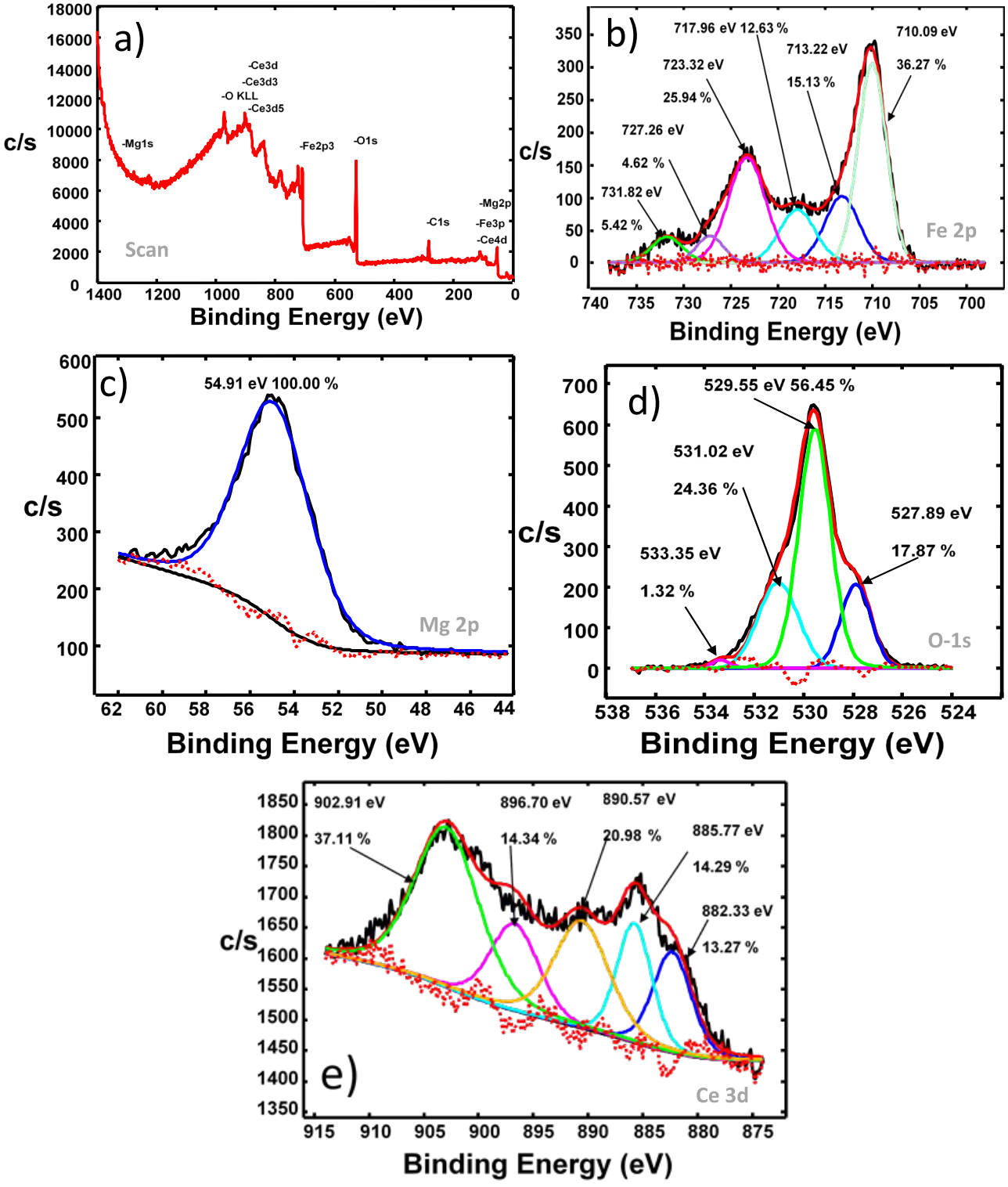

Figure 4. 8: An XPS spectra **(a)** Survey spectrum, **(b)** Fe 2d spectrum, **(c)** Mg 2p spectrum, **(d)** O 1s spectrum and **(e)** Ce 3d spectrum for the $MgCe_{0.1}Fe_{1.9}O_4$ nano-ferrite.

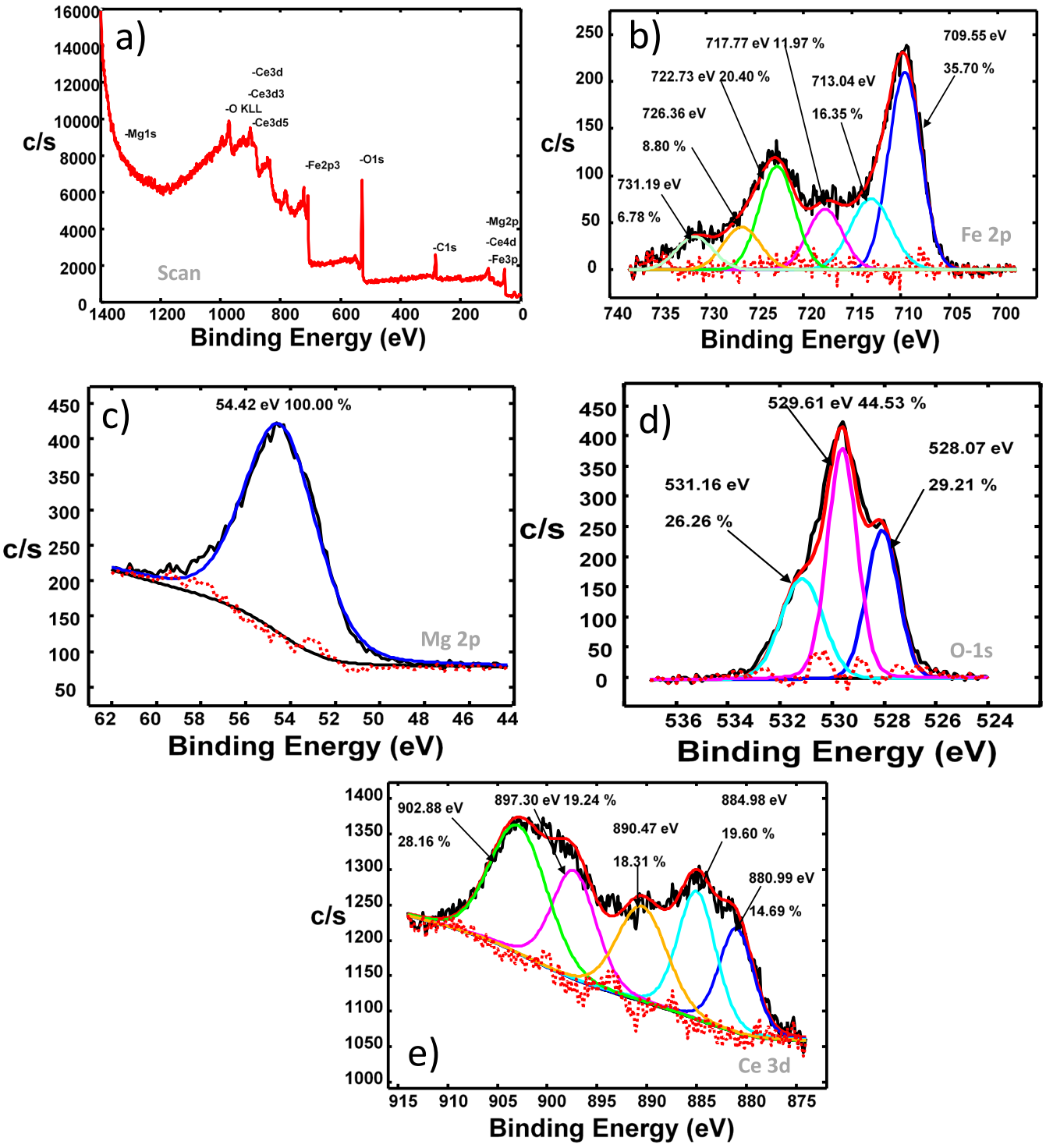

Figure 4. 9: An XPS spectra **(a)** Survey spectrum, **(b)** Fe 2d spectrum, **(c)** Mg 2p spectrum, **(d)** O 1s spectrum and **(e)** Ce 3d spectrum for the $MgCe_{0.2}Fe_{1.8}O_4$ nano-ferrite.

The $MgCe_{0.2}Fe_{1.8}O_4$ nano-ferrite, **Fig. 4.9(c)** exhibits a high-resolution XPS spectrum for the Mg 2p core level at 54.4 eV binding energy **[6]**. The broad and asymmetric peak of the high-resolution O 1s spectrum is presented in **Fig. 4.9(d)** falling between 526 and 534 eV. This can be fitted with several oxygen components corresponding to lattice oxygen (O_L), oxygen near a vacancy (O_V), and chemisorbed oxygen (O_C) with binding energies of (528.1 ± 0.1) eV (529.6 ± 0.1) eV, and (531.2 ± 0.1) eV, respectively **[7-12]**. It is unusual that the O_V (44.5%) component contributes such a large portion of the integral area as compared to the O_L (29.2%) and O_C (26.3%). This could be due to the formation of these secondary phases, i.e., CeO_2. Some oxygen compensated the CeO_2 or FeO phases. **Fig. 4.9(b)** shows a high-resolution Fe 2p spectrum consisting of characteristic peaks of Fe $2p_{3/2}$ (709.6 ± 0.1) eV and Fe $2p_{1/2}$ (722.7 ± 0.1) eV in octahedral Fe^{3+} ions. These latter minor spin-orbit doublets come with two shakeup satellites at (717.8 ± 0.1) eV and (731.2 ± 0.1) eV. The minor peaks at (713.0 ± 0.1) eV and (726.4 ± 0.1) eV were attributed to the Fe^{3+} in the tetrahedral sites **[9, 10, 13]**. There is more than double Fe^{3+} in the octahedral than in the tetrahedral sites, 0.56 in the octahedral and 0.25 in the tetrahedral sites, by comparing the areas under the peaks. This suggests that Fe^{2+} accounts for 0.19 using the inversion rule. The fitting suggests that Fe^{3+} (0.81) was reduced to Fe^{2+} (0.19). The Fe^{2+} was less than 0.2 (integral area) for all these magnesium ferrites. There is strong evidence in the normal spinel suggesting this chemical formula:

$$[Mg^{2+}_{1-\rho}Fe^{2+}_{\rho}]_A\,[Fe^{3+}_{2-\rho}Ce^{3+}]_{2B}O_{4-\delta} \qquad \text{Eq.....4. 1}$$

The lattice oxygen responsible for the chemical bonding between A-site (tetrahedral) and B-site (octahedral) cations was greatly compromised and associated with the formation of oxygen vacancies. The nature of the Mg^{+2} being charge static and the high substitution of Ce results in the formation of secondary phases evident from the XRD and HR-TEM. Finally, **Fig. 4.9(e)** presents the XPS spectrum of the Ce 3d core level consisting of double peak spin–orbits belonging to Ce $3d_{5/2}$ and Ce $3d_{3/2}$ separated by ΔE = 16.3 eV and satellite. The latter Ce 3d

spectra are typical of Ce^{3+} and Ce^{4+} oxidation states **[14-17]**. It is highly possible to see more than one Ce oxidation state.

Table 4. 2: A summary of the oxygen integral-area components and Fe ratios.

Spinel Ferrites	**O_L (528.1 eV)**	**O_V (529.9 eV)**	**O_C (531.2 eV)**	**Fe^{+3}/Fe^{+2}**
$MgFe_2O_4$	11.2 %	64.6 %	24.2 %	5.8
$MgCe_{0.05}Fe_{1.95}O_4$	17.9 %	47.6 %	31.9 + #2.7 %	4.4
$MgCe_{0.1}Fe_{1.9}O_4$	17.9 %	56.5 %	24.4 + #1.3 %	5.2
$MgCe_{0.2}Fe_{1.8}O_4$	29.2 %	44.5 %	26.3 %	2.32

Represents extra hydroxylic group

Table 4.2 shows a summary of the integral area of the oxygen components and the two Fe ratios. It is clear from the table that the O_V dominates in these magnesium ferrites. The $MgCe_{0.2}Fe_{1.8}O_4$ nano ferrites are ifferent, containing more of the O_L and less O_V , and the ratio of Fe^{3+}(B)/Fe^{3+}(A) is much greater compared to the other magnesium ferrites. The O_c (531.2 ± 0.1 eV) peak can further be deconvoluted, fitted with two peaks containing both the O_c part and hydroxylic group (#) belonging to –OH group. It is only the $MgCe_{0.05}Fe_{1.95}O_4$ and $MgCe_{0.1}Fe_{1.9}O_4$ that contain the –OH part with 0.3 and 0.1, respectively.

4.2.5 Brunauer-Emmett-Teller (BET) Measurements

The nitrogen adsorption–desorption measurements were performed to investigate the surface texture properties and whether the samples are meso-porous or macro-porous. **Fig. 4.10** indicates that the nitrogen adsorption–desorption isotherm curves of all $MgCe_xFe_{2-x}O_4$ belong to type IV **[18, 19]**. The hysteresis loop does not exhibit any limiting adsorption at high relative pressures, P/P_0.

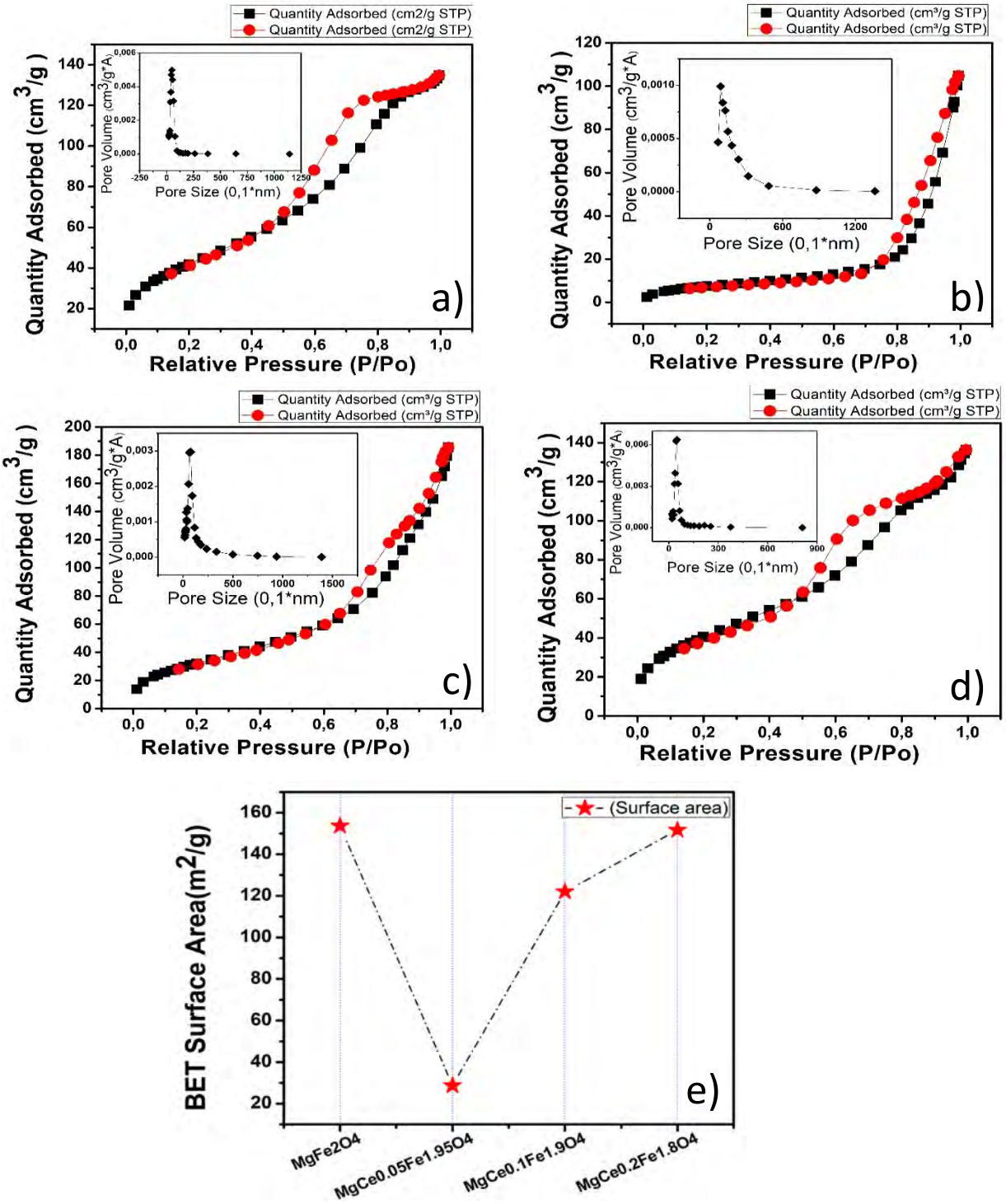

Figure 4. 10: Nitrogen adsorption-desorption isotherms of the Ce-doped magnesium ferrites, **(a)** $MgFe_2O_4$, **(b)** $MgCe_{0.05}Fe_{1.95}O_4$, **(c)** $MgCe_{0.1}Fe_{1.9}O_4$ and **(d)** $MgCe_{0.2}Fe_{1.8}O_4$ spinel ferrite. **Inset:** The corresponding pore size distribution. **(e)** represents the BET surface area as a function of Cerium content.

The calculated desorption path of the nitrogen isotherm by the Barrette-Joynere-Halenda method suggests that the pore size distribution of these Ce doped magnesium ferrites is in the smaller range of 5 - 9 nm. **Table 4.3** gives a summary of the BET surface areas, and the pore

size distribution of these magnesium ferrites. It is clearly demonstrated that the pore size distributions follow the average crystallite size trend, whereas the surface areas are not correlated. The pore size distributions and the crystallite sizes of these magnesium ferrites increase with the increase of the Ce composition but reach a maximum threshold and then decrease when the Ce concentration reaches x = 0.2 load.

Table 4. 3: Summary of the BET specific surface areas, and pore size distributions of the Ce-doped magnesium based ferrites.

Spinel Ferrites	**Spec. surf. Area (m^2/g) ± 2.85**	**Pore Size (nm) ± 1**
$MgFe_2O_4$	153.63	5
$MgCe_{0.05}Fe_{1.95}O_4$	28.70	9
$MgCe_{0.1}Fe_{1.9}O_4$	122.03	8
$MgCe_{0.2}Fe_{1.8}O_4$	151.66	5

4.2.6 Vibrating Sample Magnetometer

The vibrating sample magnetometer is the instrument commonly used to study magnetisation of materials in the presence of changing temperature and applied magnetic field. In the current study, the lakeshore 735 model was used to acquire results at room temperature using a field of -15 to +15kOe. **Fig. 4.11** shows the hysteresis loop of cerium doped magnesium ferrite. Saturation magnetisation (M_S), Maximum magnetisation (M_M), Remnant magnetisation (M_R) and Coercive field (H_C) are presented in **Table 5.1**. Saturation magnetisation was deduced by fitting the initial magnetisation with equation $M = M_s\left(1 - \frac{a}{H} - \frac{b}{H^2} - \cdots\right) + \kappa_o H$ where M_s is the saturation magnetisation which corresponds to fitting parameter P1 in **Fig. 4.12**, H is the applied field, and $\kappa_o H$ is a force magnetisation, while a and b are fit parameters **[20-22]**. Experimental magneton number (n_B) was calculated from the formula, $n_B = \frac{M_w \times M_s}{5585}$ where M_w is the molecular mass of the sample in grams and the squareness ratio of the magnetisation curves were calculated by $= \frac{M_r}{M_s}$. Saturation magnetisation and coercive field was plotted

against cerium content as shown in **Fig. 4.13**. The results show a decrease in saturation magnetisation with an increase in cerium content, while an increase in coercivity was observed.

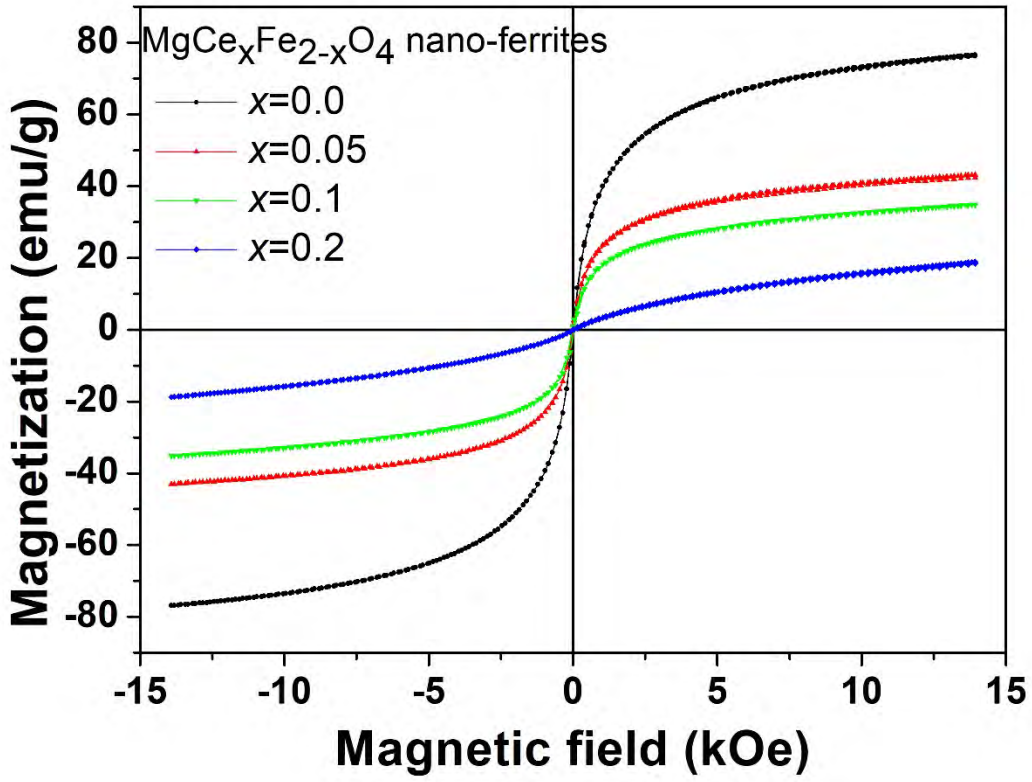

Figure 4. 11: Magnetic hysteresis loops for $MgCe_xFe_{2-x}O_4$.

Table 4. 4: Crystallite size (D_{311}), Saturation magnetisation (M_S), Remnant Magnetisation (M_R), Squareness of the loop (M_R/M_S), Maximum Magnetisation (M_M), Coercivity (H_C) and experimental magneton number (n_B).

Spinel Ferrites	D (311)	M_S (emu/g)	M_R (emu/g)	SQR (M_R/M_S)	Mm (emu/g)	H_C (Oe)	n_B (μ_B)
	± 0.41	± 0.2	± 0.05		± 0.1	± 1.4	
$MgFe_2O_4$	8.37	72.9	2.726	0.0374	76.7	8.3	2.60
$MgCe_{0.05}Fe_{1.95}O4$	10.15	39.6	0.730	0.0184	43.3	16.3	1.45
$MgCe_{0.1}Fe_{1.9}O4$	15.39	27.9	1.269	0.0455	35.0	26.8	1.04
$MgCe_{0.2}Fe_{1.8}O4$	5.24	8.6	0.242	0.0281	18.4	52.0	0.33

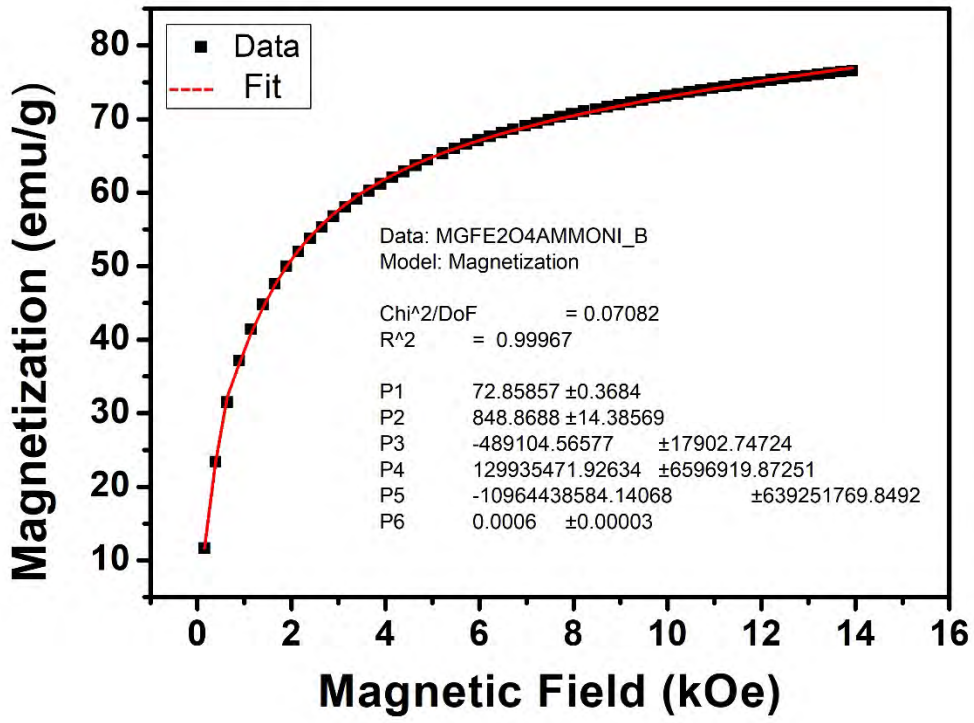

Figure 4. 12: Fitted initial magnetisation curve of $MgFe_2O_4$ for saturation magnetisation calculation.

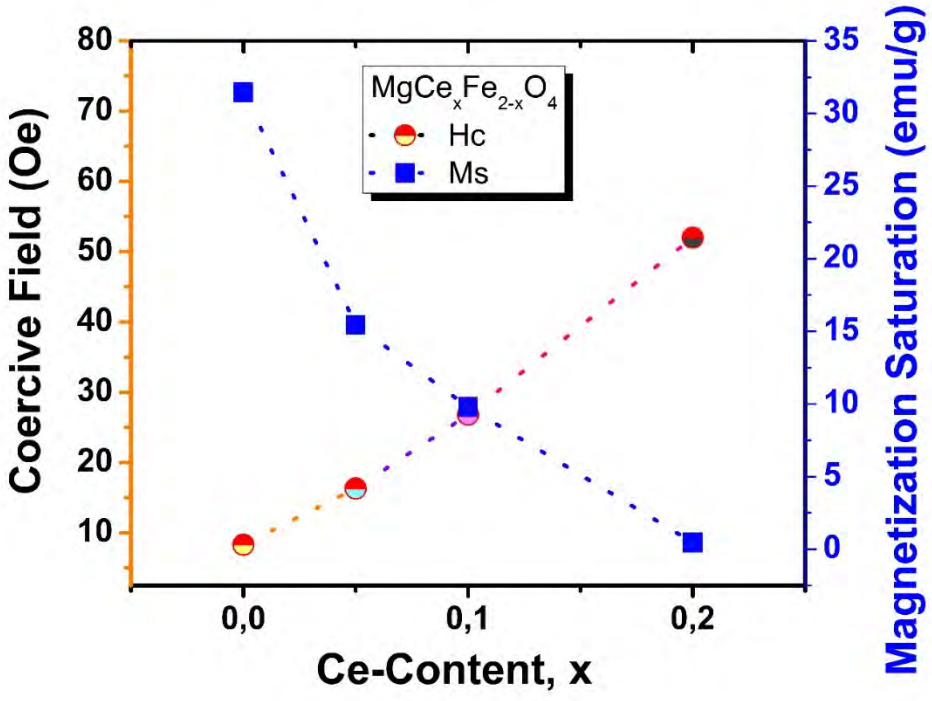

Figure 4. 13: Variation of Saturation magnetisation and Coercive field with an increase in Cerium content of $MgCe_xFe_{2-x}O_4$(x= 0.0, 0,05, 0.1, 0.2).

This may be due to the substitution of a small quantity of Fe^{3+} ions by Ce^{3+} ions on the B-site, since the effective magnetic moment of Ce^{3+} ions is less than that of Fe^{3+} ions. The Ce^{3+}-Fe^{3+} interactions are weaker than Fe^{3+}-Fe^{3+} interactions, therefore magnetisation is expected to decrease with a decrease in super-exchange interactions because of a decrease in Fe^{3+} content. An increase in the content of Ce^{3+} leads to the formation of a secondary phase at grain boundaries which cause the movement of domain walls to be more difficult, therefore the coercivity increases. It should be noted that lowering the magneton number, n_B, suggests a weak super-exchange coupling among the lattice sites **[2, 23-25]**. The maximum saturation magnetisation (M_s) and magneton moment (n_B) values were observed for $MgFe_2O_4$ without Ce^{3+} at $x = 0$, (see **Table 4.4**). The (M_s) and (M_R) values together with (n_B) revealed a trend to lower values as the concentration of Ce^{3+}ions was increased. This implied deteriorating super-exchange interactions in the particles, as mentioned earlier.

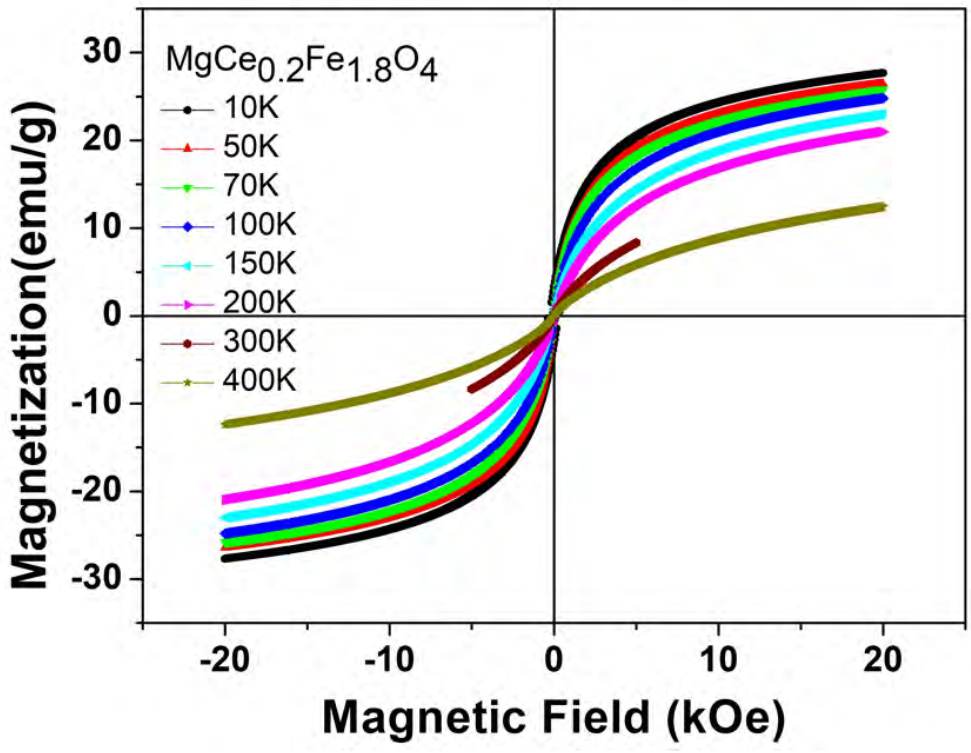

Figure 4. 14: Magnetic hysteresis loops for $MgCe_{0.2}Fe_{1.8}O_4$ at different temperatures.

Another significant indicator of either hard or soft magnetic properties is the Squareness ratio (SQR) of the loops, $\frac{M_r}{M_s}$. If SQR ≥ 0.5, it implies that the nanoparticles contain multiple magnetic domains (MMD), whereas if SQR ≤ 0.5 these nanoparticles consist of a single magnetic domain (SMD) **[5, 23, 25, 26]**. Magnetisation measurements at lower temperatures (10 – 400K) were performed for the $MgFe_{1.8}O_4$ sample using a SQUID. Hysteresis loops at different temperatures in an applied field of up to 20 kOe are presented in **Fig. 4.14**. Coercivity (H_C), Maximum saturation (M_S), Remnant Magnetisation (M_R), Maximum Magnetisation (M_m), Squareness of the loop (M_R/M_S), and magneton number (n_B) for $MgCe_{0.2}Fe_{1.8}O_4$ were calculated and presented in **Table 4.5**. In the current work the SQR values of these magnetism nano-ferrites, both at room temperature and lower temperatures were very small, suggesting their uniaxially anisotropic single magnetic domain character.

Table 4. 5: Coercivity (H_C), Maximum saturation (M_S), Remnant Magnetisation (M_R), Maximum Magnetisation (M_m), Squareness of the loop (M_R/M_S), and magneton number (n_B) for $MgCe_{0.2}Fe_{1.8}O_4$

T (K)	H_C (emu/g)	M_S (emu/g)	M_R (emu/g)	M_M (emu/g)	SQR	n_B (μ_B)
10	339.2	24.6	3.293	27.7	0.134	0.955
50	52.5	22.7	0.609	26.4	0.027	0.881
70	27.8	22.2	0.345	25.8	0.016	0.862
100	24.5	21.9	0.296	24.8	0.014	0.850
150	20.3	18.2	0.205	22.9	0.011	0.707
200	15.5	16.1	0.117	21.0	0.007	0.625
400	6.2	6.0	0.016	12.4	0.003	0.233

It should also be noted that the SQR values in the temperature range 10-400 K were very small, as shown in **Table 4. 5**. This is further suggestive of a strong surface spin disordering [23]. Therefore, an increase in the content of Ce^{3+} leads to the formation of a secondary phase at

grain boundaries which causes the movement of domain walls to be more difficult, therefore the coercivity increases. It should be noted that the magnetisation of spinel ferrites is the difference between the magnetisation at B-site and A-site. The substitution of Ce into the B-site seems to suggest superparamagnetic to paramagnetic behaviour.

4.2.7 Mössbauer Spectroscopy Results

Room temperature Mössbauer spectra for as-prepared samples of $MgCe_xFe_{2-x}O_4$ where $0 \leq x \leq 0.2$ are shown in **Fig. 4.15**.

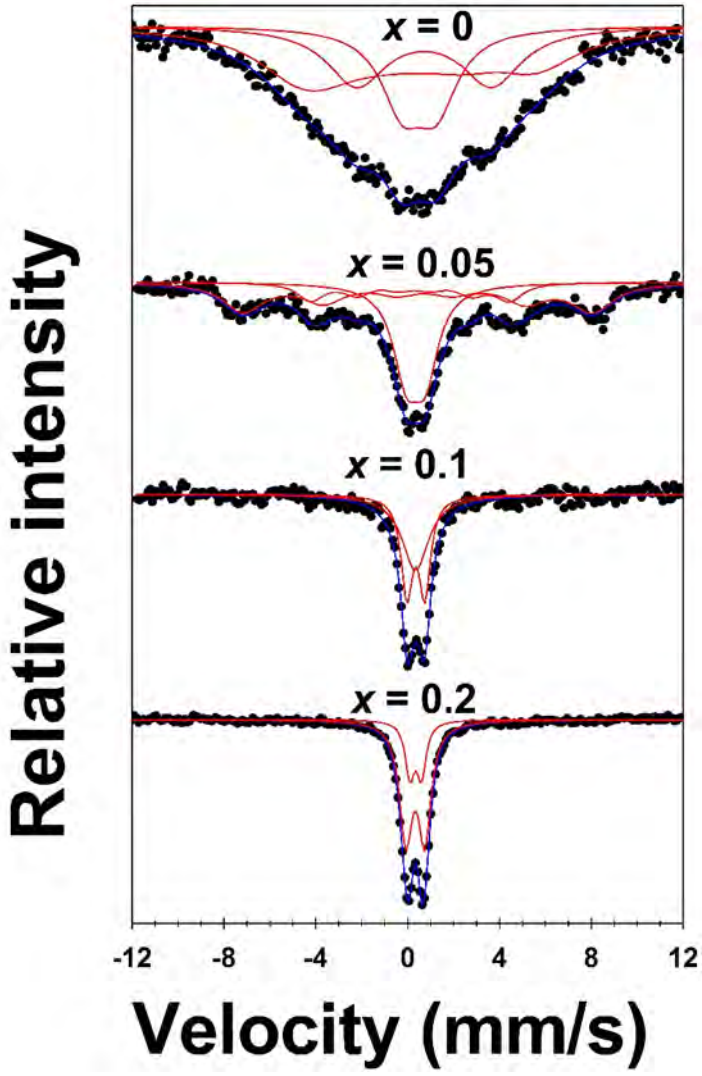

Figure 4. 15: Mössbauer spectra for the $MgCe_xFe_{2-x}O_4$ Nano ferrites measured at room temperature.

The scattered data points correspond to the experimental data while the solid lines connecting data points represent the fitting. The data points were fitted based on Lorentzian site analysis with the aid of Recoil Mössbauer analysis software. The spectra show transformation from ordered to paramagnetic spin state with an increase in Ce ions concentration. The spectrum for $x = 0$ and 0.05 shows ordered and paramagnetic behavior at room temperature while for $x = 0.1$ and 0.2 shows only paramagnetic behaviour. The Mössbauer spectrum for ordered sample could be fitted with two sextets attributed to fraction of ordered Fe^{3+} ions at the A- and B-sites of the spinel structure **[21, 22],** and one doublet was fitted. showing that there are iron ions (Fe^{+2}) which are in a paramagnetic state **[27]**. For samples ($x = 0.1$ and 0.2) two doublets were used to fit the Mössbauer data. This shows that the samples are completely paramagnetic, which is due to unordered magnetic spins and small particle size. The transition from ordered to paramagnetic tends to increase gas sensitivity, as observed in Dlamini et al **[28]**. The direct link between Mossbauer data and gas sensing is not yet well established. The Mössbauer parameters, variation of isomer shifts (δ), hyperfine fields (H), quadruple splitting (QS), line widths (W) and Fe fractions (f) extracted from the fit are presented in **Table 4. 6**. To assign the sextet or doublet to A and B site, the isomer shift criterion was used. The isomer shift for the tetrahedral (A) site is always lower than that of the Octahedral (B) site due to the high symmetry at the A-site **[21]**.

Table 4. 6: Variation of isomer shift (δ), hyperfine fields (H), quadruple splitting (Qs), line widths (W), and Fe fractions (f) on A and B sites with Ce-substitution in $MgCe_xFe_{2-x}O_4$.

$MgCe_xFe_{2-x}O_4$	δ_A (mm/s)	δ_B (mm/s)	H_A (kOe)	H_B (kOe)	O_{SA} (mm/s)	O_{SB} (mm/s)	W_A (mm/s)	W_B (mm/s)	F_A (%)	F_B (%)
Error	± 0.04	± 0.14	± 2	± 8	± 0.10	± 0.3	± 0.06	± 0.02	-	-
x = 0.0	0.50	0.71	297	-	1.5	5.52	1.18	1.18	26.5	13.1
x = 0.05	0.19	0.56	253	444	-	-	0.65	1.0	17.2	43.2
x = 0.1	0.32	0.33	-	-	0.001	0.74	0.66	0.29	47.9	52.1
x = 0.2	0.33	0.34	-	-	0.82	0.51	0.34	0.24	74.8	25.2

4.2.8 Photoluminescence Spectroscopy Measurements

To investigate light emission properties of magnesium-cerium doped ferrites, photoluminescence (PL) optical measurements were conducted at room-temperature. PL emission measurements were performed using a continuous helium cadmium laser excited with 325 nm wavelength chopped at 120 Hz and the exit slits were 250 μm, as described in the experimental section in chapter 3. These normal spinel ferrites emit continuous visible electromagnetic waves in the 400 – 500 nm range. These range from violet/deep blue to green lights. The peak intensities are centred at 415 (3.0 eV) and 435 nm (2.85 eV), as shown in **Fig. 4. 16.**

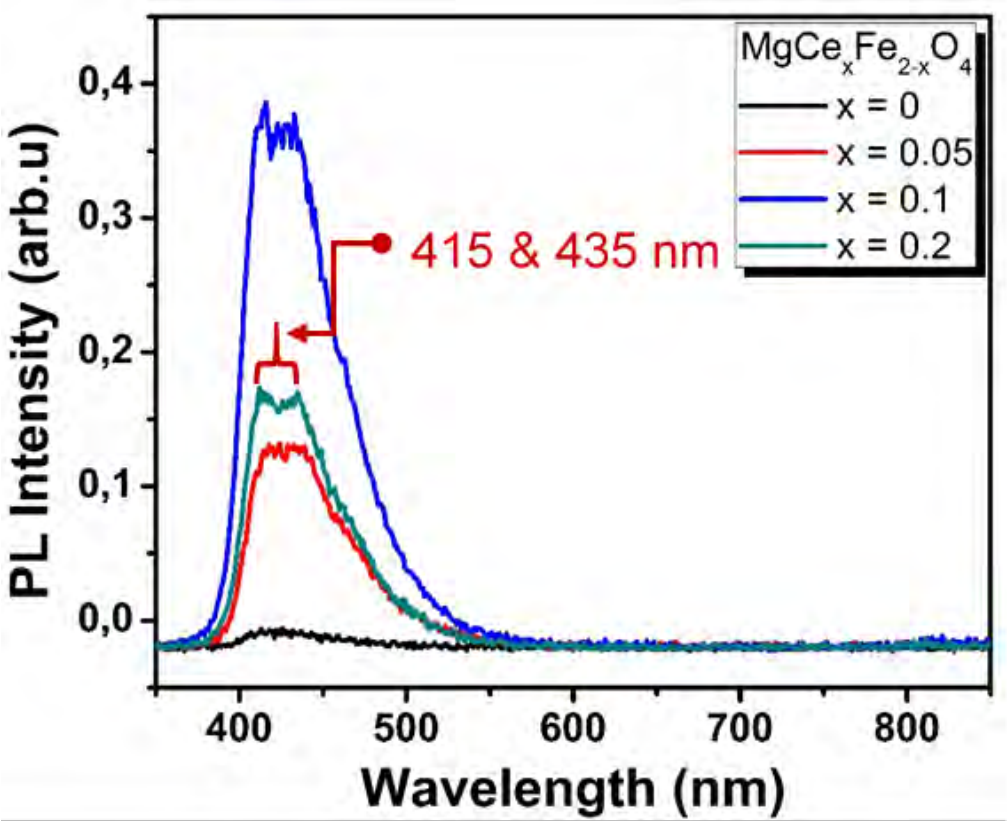

Figure 4. 16: Photoluminescence spectra at room-temperature of the $MgCe_xFe_{2-x}O_4$ at various Ce compositions.

These light emissions are attributed to exciton recombination, cations interstitials, and oxygen interstitials and vacancies **[29, 30]**. The unsubstituted spinel ferrite, $MgFe_2O_4$ had the lowest PL intensity. Increasing the Ce substitution (by $x = 0.05$) in the octahedral site of Fe resulted in

better enhancement of the emission intensity. Further increasing the Ce (by x = 0.1) led to a significant rise in the intensity to the highest of these magnesium ferrites. This Ce composition substitution seems to be the optimal incorporation into the octahedral sites of the Fe. Two possibilities should be considered for the luminescence, namely emission from Ce^{3+} ions or from host defects which resulted from the Ce doping. The emission wavelength of the f-d transitions from Ce^{3+} ions is host dependent and often occurs in the blue visible range, e.g., centred at 490 nm for Ce doped MgAl2O4 spinel annealed in a reducing atmosphere **[30]**. However, similar luminescence to that observed in this study was also found previously from undoped $MgFe_2O_4$ as well from $CoFe_2O_4$ doped with either Ce or Sm **[30]**. This very strongly implies that the luminescence in **Fig. 4.16** must be attributed to host defects rather than to Ce^{3+} ions. Therefore, luminescence from the Ce^{3+} ions may not be effectively excited at the laser wavelength of 325 nm or may have been quenched. It should also be noted the Fe ions or iron group elements are generally considered to act as quenching centres for phosphor luminescence **[31]**. The similar PL emissions **[32]** were attributed to host defect centres such as oxygen vacancies, interstitials, cation vacancies and charge transfer electronic transitions between the oxygen anions and metal cations. The doping of $MgFe_2O_4$ with Ce clearly had a strong influence on the formation of host defects, while the formation of secondary phases and the loss of crystalline quality of the spinel ferrite with high Ce doping (x = 0.2), as demonstrated from the XRD and HRTEM analyses is expected to be coupled with a change in the defect's concentrations or increased quenching of luminescence from existing defects.

4.3 REFERENCES

[1] Run Zhang, Yan Wang, Zhanying Zhang, J. Cao, Highly Sensitive Acetone Gas Sensor Based on g-C_3N_4 Decorated $MgFe_2O_4$ Porous Microspheres Composites., Sensors 18 (2018) 2211.

[2] Y. Slimani, M.A. Almessiere, A.D. Korkmaz, S. Guner, H. Güngüneş, M. Sertkol, A. Manikandan, A. Yildiz, S. Akhtar, S.E. Shirsath, A. Baykal, $Ni_{0.4}Cu_{0.2}Zn_{0.4}Tb_xFe_{2-x}O_4$ nanospinel ferrites: Ultrasonic synthesis and physical properties, Ultrasonics Sonochemistry 59 (2019) 104757.

[3] P. Scherrer, Nachrichten von der Gesellschaft der Wissenschaften zu Göttingen (1918) 98-100. Just asking. Is 1918 correct?

[4] K. Elayakumar, A. Manikandan, A. Dinesh, K. Thanrasu, K. Kanmani Raja, R. Thilak Kumar, Y. Slimani, S.K. Jaganathan, A. Baykal, Enhanced magnetic property and antibacterial biomedical activity of Ce^{3+} doped $CuFe_2O_4$ spinel nanoparticles synthesized by sol-gel method, Journal of Magnetism and Magnetic Materials 478 (2019) 140-147.

[5] M.A. Almessiere, Y. Slimani, M. Sertkol, F.A. Khan, M. Nawaz, H. Tombuloglu, E.A. Al-Suhaimi, A. Baykal, Ce–Nd Co-substituted nanospinel cobalt ferrites: An investigation of their structural, magnetic, optical, and apoptotic properties, Ceramics International 45 (2019) 16147-16156.

[6] V. Rheinheimer, C. Unluer, J. Liu, S. Ruan, J. Pan, P.J.M. Monteiro, XPS Study on the Stability and Transformation of Hydrate and Carbonate Phases within MgO Systems, Materials 10 (2017).pages?

[7] K. Shingange, H.C. Swart, G.H. Mhlongo, Design of porous p-type $LaCoO_3$ nanofibers with remarkable response and selectivity to ethanol at low operating temperature, Sensors and Actuators B: Chemical 308 (2020) 127670.

[8] R. Zhang, S. Cao, T. Zhou, T. Fei, R. Wang, T. Zhang, Rational design and tunable synthesis of Co_3O_4 nanoparticle-incorporating into In_2O_3 one-dimensional ribbon as effective sensing material for gas detection, Sensors and Actuators B: Chemical 310 (2020) 127695.

[9] T. Zhou, T. Zhang, Y. Zeng, R. Zhang, Z. Lou, J. Deng, L. Wang, Structure-driven efficient $NiFe_2O_4$ materials for ultra-fast response electronic sensing platform, Sensors and Actuators B: Chemical 255 (2018) 1436-1444.

[10] P. Hao, P. Song, Z. Yang, Q. Wang, Synthesis of novel RuO_2/$LaFeO_3$ porous microspheres its gas sensing performances towards triethylamine, Journal of Alloys and Compounds 806 (2019) 960-967.This title is not grammatical. Please check the original for punctuation.

[11] K. Ding, X. Zhang, J. Li, P. Yang, X. Cheng, Formation of Dandelion-Like Co_3O_4/$CoWO_4$ Heterojunctions for Enhanced Supercapacitive Performance, ChemElectroChem 4 (2017) 3011-3017.

[12] T. Meng, H. Jia, H. Ye, T. Zeng, X. Yang, H. Wang, Y. Zhang, Facile preparation of $CoMoO_4$ nanorods at macroporous carbon hybrid electrocatalyst for non-enzymatic glucose detection, Journal of Colloid and Interface Science 560 (2020) 1-10.

[13] S. Wu, X. Li, Y. Xu, J. Wu, Z. Wang, Y. Han, X. Zhang, Hierarchical spinel $Ni_xCo_{1-x}Fe_2O_4$ microcubes derived from Fe-based MOF for high-sensitive acetone sensor, Ceramics International 44 (2018) 19390-19396.Please check original title.

[14] C. Suchomski, B. Breitung, R. Witte, M. Knapp, S. Bauer, T. Baumbach, C. Reitz, T. Brezesinski, Microwave synthesis of high-quality and uniform 4 nm $ZnFe_2O_4$ nanocrystals for application in energy storage and nanomagnetics, Beilstein Journal of Nanotechnology 7 (2016) 1350-1360.

[15] C.L. Campos, C. Roldán, M. Aponte, Y. Ishikawa, C.R. Cabrera, Preparation and methanol oxidation catalysis of Pt-CeO_2 electrode, Journal of Electroanalytical Chemistry 581 (2005) 206-215.

[16] C.M. Sims, R.A. Maier, A.C. Johnston-Peck, J.M. Gorham, V.A. Hackley, B.C. Nelson, Approaches for the quantitative analysis of oxidation state in cerium oxide nanomaterials, Nanotechnology 30 (2018) 085703.

[17] M.K. Kesarla, M.O. Fuentez-Torres, M.A. Alcudia-Ramos, F. Ortiz-Chi, C.G. Espinosa-González, M. Aleman, J.G. Torres-Torres, S. Godavarthi, Synthesis of g-C_3N_4/N-doped CeO_2 composite for photocatalytic degradation of an herbicide, Journal of Materials Research and Technology 8 (2019) 1628-1635.

[18] Z. Jing, J. Zhan, Fabrication and Gas-Sensing Properties of Porous ZnO Nanoplates, Advanced Materials 20 (2008) 4547-4551.

[19] R.G. Motsoeneng, I. Kortidis, R. Rikhotso, H.C. Swart, S.S. Ray, D.E. Motaung, Temperature-dependent response to C_3H_7OH and C_2H_5OH vapors induced by deposition of Au nanoparticles on SnO_2/NiO hollow sphere-based conductometric sensors, Sensors and Actuators B: Chemical 316 (2020) 128041.

[20] Y. Li, L. Shi, J. Zhao, S. Zhou, C. Xie, J. Guo, The effect of charge transfer on the transport and magnetic properties induced by Ca substitution in $La_{0.3}Ce_{0.2}Sr_{0.5}MnO_3$, Journal of Alloys and Compounds 725 (2017) 349-354.

[21] B. Ndlovu, J.Z. Msomi, T. Moyo, Mössbauer and electrical studies of $Ni_xCo_{1-x}Fe_2O_4$ nanoparticles, Journal of Alloys and Compounds 745 (2018) 187-195.

[22] J.Z. Msomi, T. Moyo, H.M.I. Abdallah, Magnetic Properties of Mg_x $Mn_{1-x}Fe_2O_4$ Nanoferrites, Journal of Superconductivity and Novel Magnetism 25 (2011) 2643-2646.

[23] M.A. Almessiere, Y. Slimani, S. Guner, M. Sertkol, A. Demir Korkmaz, S.E. Shirsath, A. Baykal, Sonochemical synthesis and physical properties of $Co_{0.3}Ni_{0.5}Mn_{0.2}Eu_xFe_{2-x}O_4$ nano-spinel ferrites, Ultrasonics Sonochemistry 58 (2019) 104654.

[24] M.A. Almessiere, Y. Slimani, A.D. Korkmaz, A. Baykal, H. Güngüneş, H. Sözeri, S.E. Shirsath, S. Güner, S. Akhtar, A. Manikandan, Impact of La^{3+} and Y^{3+} ion substitutions on structural, magnetic and microwave properties of $Ni_{0.3}Cu_{0.3}Zn_{0.4}Fe_2O_4$ nanospinel ferrites synthesized via sonochemical route, RSC Advances 9 (2019) 30671-30684.

[25] M.A. Almessiere, Y. Slimani, A. Demir Korkmaz, S. Güner, A. Baykal, S.E. Shirsath, I. Ercan, P. Kögerler, Sonochemical synthesis of Dy^{3+} substituted $Mn_{0.5}Zn_{0.5}Fe_{2-x}O_4$ nanoparticles: Structural, magnetic and optical characterizations, Ultrasonics Sonochemistry 61 (2020) 104836.

[26] M.A. Almessiere, Y. Slimani, A. Baykal, Synthesis and characterization of $Co_{1-2x}Ni_xMn_xCe_yFe_{2-y}O_4$ nanoparticles, Journal of Rare Earths 38 (2020) 188-194.

[27] Bonanni, Alberta, Michał Kiecana, Clemens Simbrunner, Tian Li, Maciej Sawicki, Matthias Wegscheider, Martin Quast et al. "Paramagnetic GaN: Fe and ferromagnetic (Ga, Fe) N: The relationship between structural, electronic, and magnetic properties." Physical Review B 75, no. 12 (2007): 125210.

[28] Dlamini, Sanele, Steven Nkosi, Thomas Moyo, and Amos Nhlapo. "Structural and magnetic characterization of Co2+ substituted Ni-Zn ferrite nanoparticles synthesized by refluxing co-precipitation and their potential application as gas sensors." Materials Science and Engineering: B 294 (2023): 116554.

[29] Andris ˇSutka, Karlis A. Grossa, Spinel ferrite oxide semiconductor gas sensors., Sensors and Actuators B 222 (2016) 95-105.

[30] A.E. Abbass, H.C. Swart, R.E. Kroon, Effect of silver ions on the energy transfer from host defects to Tb ions in sol–gel silica glass, Journal of Luminescence 160 (2015) 22-26.

[31] Tabaza, W. A. I., H. C. Swart, and R. E. Kroon. "Luminescence of Ce doped MgAl2O4 prepared by the combustion method." Physica B: Condensed Matter 439 (2014): 109-114.

[32] Gumbi, Sifiso W., Prince S. Mkwae, Ioannis Kortidis, Robin E. Kroon, Hendrik C. Swart, Thomas Moyo, and Steven S. Nkosi. "Electronic and simple oscillatory conduction in ferrite gas sensors: Gas-sensing mechanisms, long-term gas monitoring, heat transfer, and other anomalies." ACS Applied Materials & Interfaces 12, no. 38 (2020): 43231-43249.

CHAPTER 5

GAS SENSING PROPERTIES OF $MgCe_xFe_{2-x}O_4$ NANOFERRITES

5.1 INTRODUCTION

This chapter presents the gas and vapour sensing properties of the $MgCe_xFe_{2-x}O_4$ nanoferrites with various Ce substitution (x = 0, 0.05, 0.1, & 0.2) in the octahedral Fe-site. These nanoferrites were evaluated in terms of the sensors' current ratios (response/sensitiveness) to various volatile organic compounds (VOCs) and flammable gases.

5.2 GAS SENSING PROPERTIES OF $MgCe_xFe_{2-x}O_4$ NANOFERRITES TOWARDS VOLATILE ORGANIC COMPOUNDS (VOC'S)

Gas sensing measurements were performed on $MgCe_xFe_{2-x}O_4$ nanoferrites using a KS026K16 (KENOSISTEC model, Italy) gas testing system. The sensor was fabricated as described in chapter 3. The activation energy/ operation temperature of a sensor was determined by exposing the sensor to 100 ppm of acetone while changing the operating temperature. **Fig. 5.1** demonstrates how the operating temperature was varied (25 – 275 °C) towards the acetone vapour at 100 ppm concentration. It can be seen from the blue line in **Fig. 5.1** that acetone response increased to maximum and decreased thereafter, making the 225 °C operating temperature to be the optimal. The current in air (black line) follows the response increase-maximum-decrease trend. On the other hand, the current in the presence of acetone gas (red line) increased exponentially.

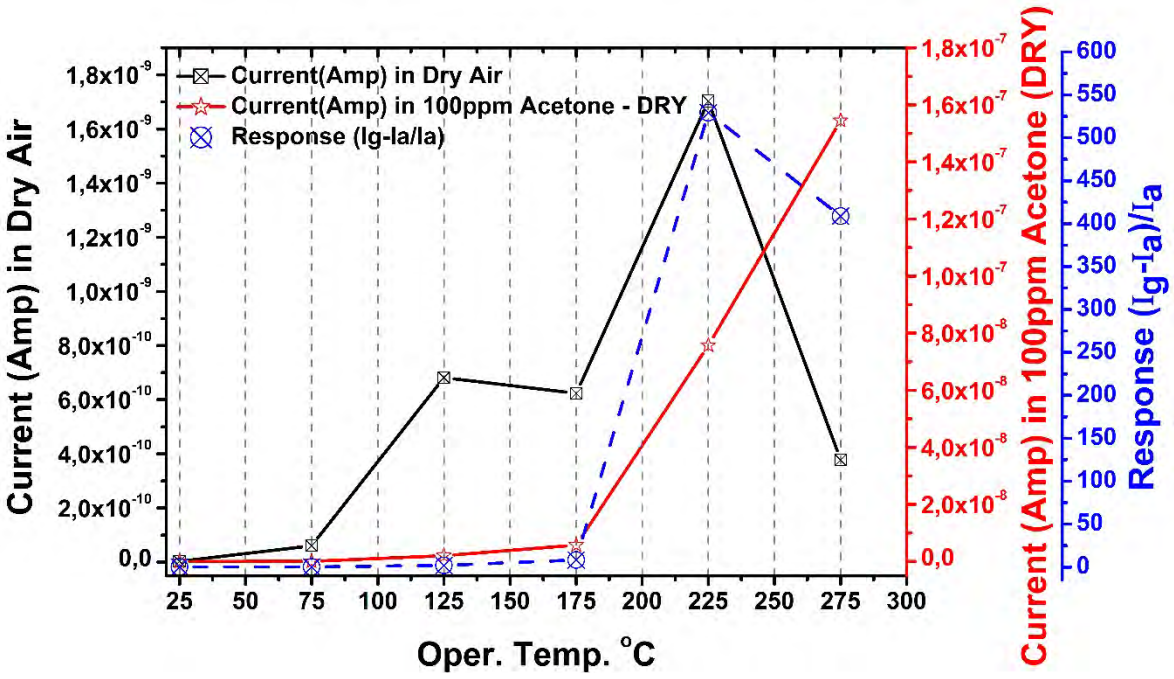

Figure 5. 1: Activation temperature (25 – 275 °C) plots of $MgCe_{0.2}Fe_{1.8}O_4$ ferrite over 100 ppm acetone.

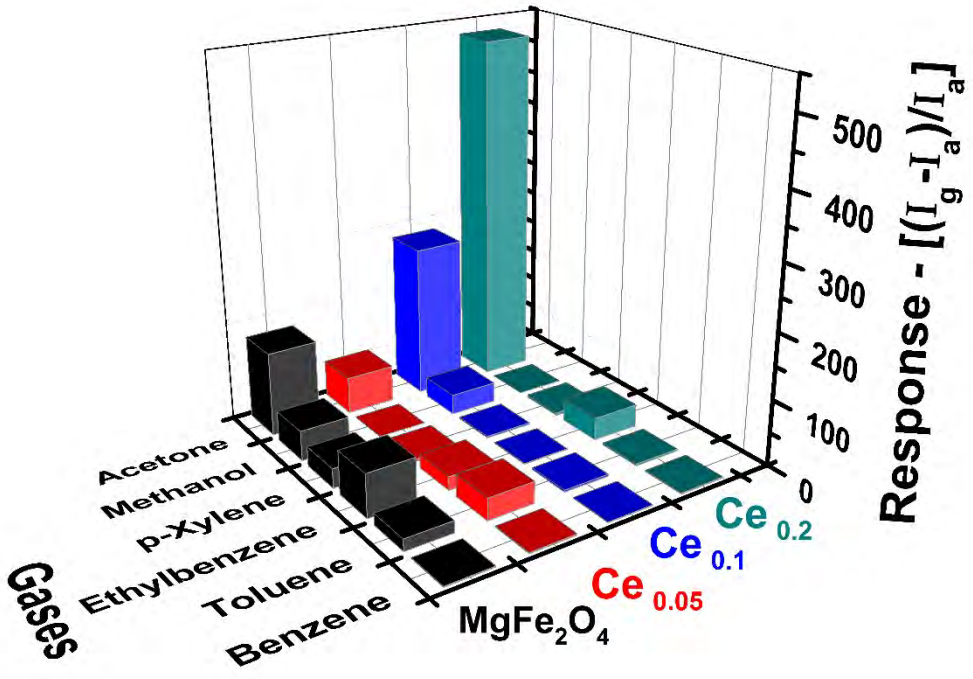

Figure 5. 2: Responses of $MgCe_xFe_{2-x}O_4$ nanoferrites (x = 0, 0.05, 0.1, & 0.2) to acetone, methanol, xylene, ethylbenzene, toluene, and benzene at 100 ppm.

Then all samples of $MgCe_xFe_{2-x}O_4$ (x= 0.0, 0.05, 0.1 and 0.2) nanoferrites were evaluated against different volatile organic compounds (VOCs) such as acetone, methanol, p-xylene, ethylbenzene, toluene, and benzene at their pronounced concentrations and operating temperature of 225 °C as shown in **Fig. 5.2**. It is clearly seen from **Fig. 5.2** that the $MgCe_{0.2}Fe_{1.8}O_4$ (x = 0.2) nanoferrites display the highest response of about 529.28 to acetone vapour at 100 ppm over the other interfering gases/vapours exhibiting low response. This suggests the $MgCe_{0.2}Fe_{1.8}O_4$ nanoferrites are selective and permanence to acetone vapour detection. The ability of a sensor to respond to a particular gas analyte as compared to others is called selectivity. Meanwhile, the selectivity coefficient is more specific comparing acetone selectivity to each specific tested gas. The selectivity coefficient is the response ratio $S_{acetone}/S_{gas} = K_{coefficient}$, where $S_{acetone}$ and S_{gas} are the responses of the sensor in acetone and other gases tested. The selectivity coefficients, $K_{coefficient}$, for the $MgCe_{0.2}Fe_{1.8}O_4$ nanoferrites sensor were $529.28_{acetone}/S_{gas}$, 392.1 to benzene, 182.5 to toluene, 15.5 to ethylbenzene, 140.0 to p-xylene, and 5292.8 to methanol. The $MgCe_{0.2}Fe_{1.8}O_4$ based sensor showed an excellent selectivity for acetone against methanol, benzene, toluene, p-xylene, and ethylbenzene, in descending order.

Then the best performing sample ($MgCe_{0.2}Fe_{1.8}O_4$) was exposed to various acetone concentrations. **Fig. 5.3** shows the transient current curves of the $MgCe_{0.2}Fe_{1.8}O_4$ nanoferrites sensor towards various concentrations of acetone (5, 10, 20, 50, 80, & 100 ppm) at 225 °C operating temperature. Upon the exposure of acetone, a reducing gas, the sensor's transient current increases in step with the concentration increment. This, therefore, suggests that the $MgCe_xFe_{2-x}O_4$ is an n-type semiconductor. The sensor shows two linear regressions between 5 – 20 ppm and 50 – 100 ppm of acetone concentration. The inset in **Fig. 5.3** exhibits clear transient curves of the 5 and 10 ppm concentrations.

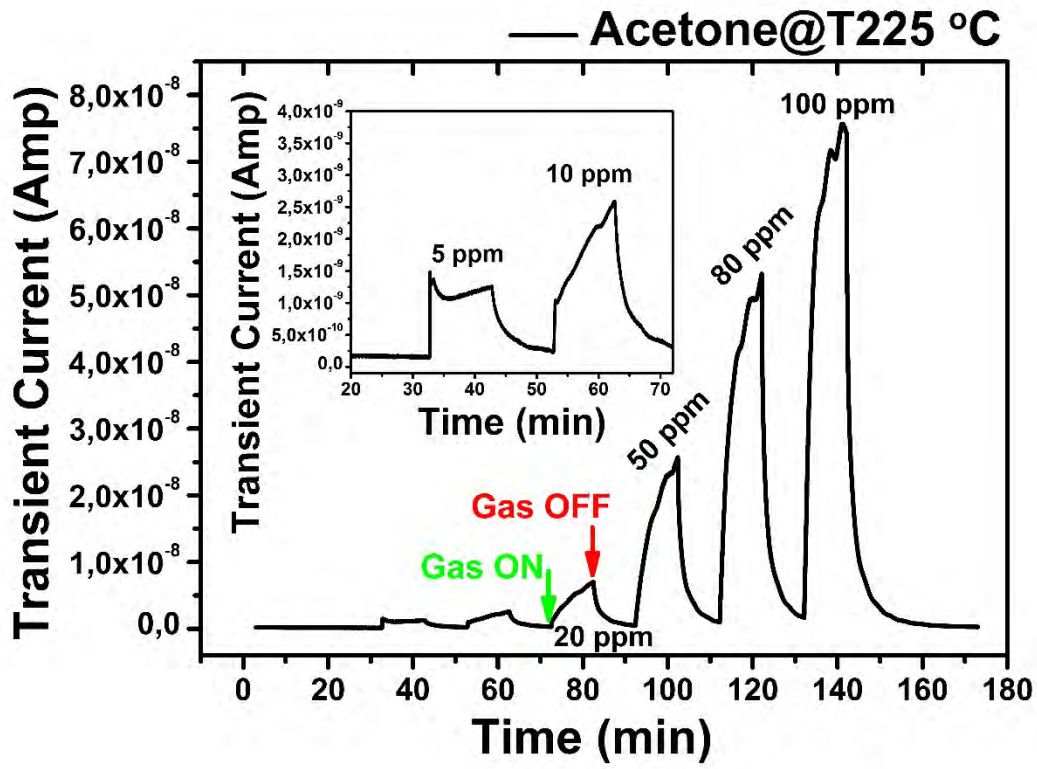

Figure 5. 3: Transient current curves of acetone to various concentrations (5-100 ppm) and the inset zoom-in of 5 & 10 ppm.

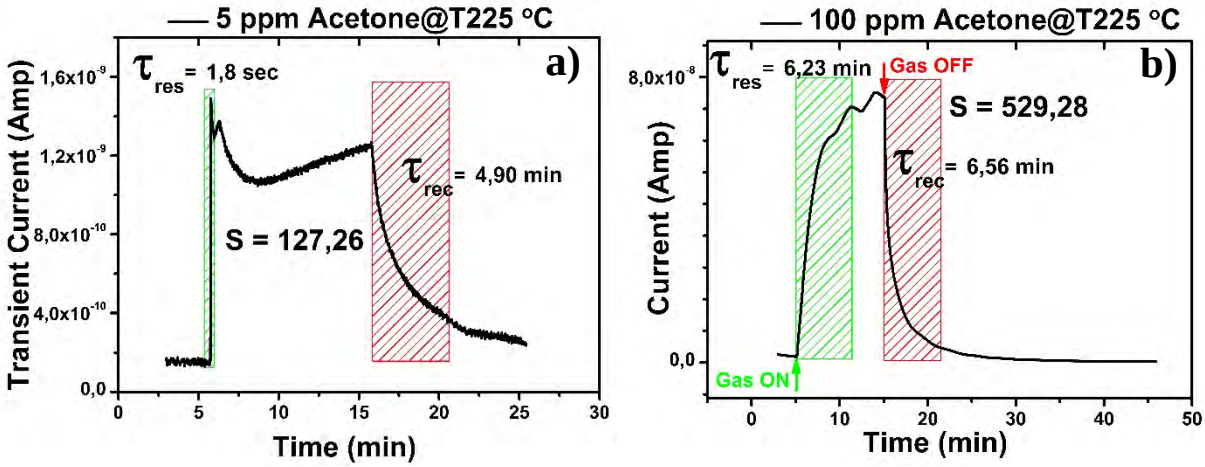

Figure 5. 4: Transient current curve showing the response- and recovery-times towards **(a)** 5 ppm and **(b)** 100 ppm acetone at 225 ℃.

The response- and recovery-times are shown in **Fig. 5. 4(a)** towards the 5 ppm concentration. The sensor recorded a quick response-time of 1.8 s is followed by a recovery-time of 4.9 min.

However, both the response- and recovery-times increased with increasing of the acetone concentration from 5 to 100 ppm. The response- and recovery-times at 100 ppm were 6.23 and 6.56 min, respectively, as shown in **Fig. 5. 4(b).** This response- and recovery-times trend agrees with the work of Zhang et al **[1]**. on a $CoFe_2O_4$ sensor towards acetone. However, these trends are in contradiction to authors elsewhere **[2-4]**.

The dependence of the acetone response to the bias voltage was investigated. The applied bias voltage to the $MgCe_{0.2}Fe_{1.8}O_4$ sensor was varied from 0.1, 1, 2, 3, 5, and 7 V. **Fig. 5. 5 (a)** shows a plot of acetone response versus bias voltage. From the plot two bias voltages of 0.1 and 5 V showed the highest acetone responses of 360 and 529, respectively.

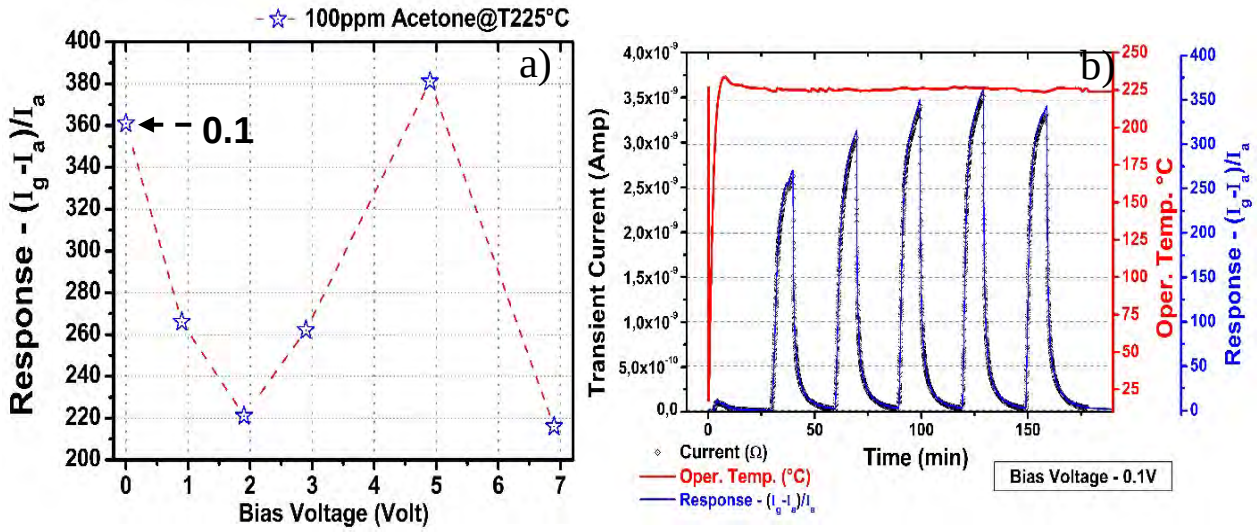

Figure 5. 5: (a) Activation bias voltage of the $MgCe_{0.2}Fe_{1.8}O_4$ nanoferrites and **(b)** repeatable (0.1 V) 100 ppm towards acetone.

The sensor showed a strong dependence on the applied bias voltage. Therefore, the bias voltage of 5V was chosen to optimise the sensor. All the applied bias voltages were repeatable, as shown in **Fig. 5. 5 (b).** The activation energy for the electron hopping (since it is an n-type) can be calculated using the Arrhenius plot of the resistance:

$$R = R_0 e^{-\Delta E_A / k_B T} \qquad \text{Eq.....5. 1}$$

$$LnR = LnR_0 - \Delta E_A / k_B T \qquad \text{Eq.....5. 2}$$

where R is the sensor's resistance, k_B is the Boltzmann's constant, T is the absolute temperature, and ΔE_A is the activation energy **[5-8]**. The plot of LnR vs. 1/T shown in **Fig. 5. 6(a)** allow us to extract the slope (-3597) of **Eq. 5.2** which is equal to $-\Delta E_A/k_B$ and to calculate ΔE_A. The calculated activation energy for this sensor, $MgCe_{0.2}Fe_{1,8}O_4$ nanoferrites, was found to be ΔE_A = 0.31±0.08 eV. This activation energy extrapolated at 25 °C shows a semiconducting behaviour.

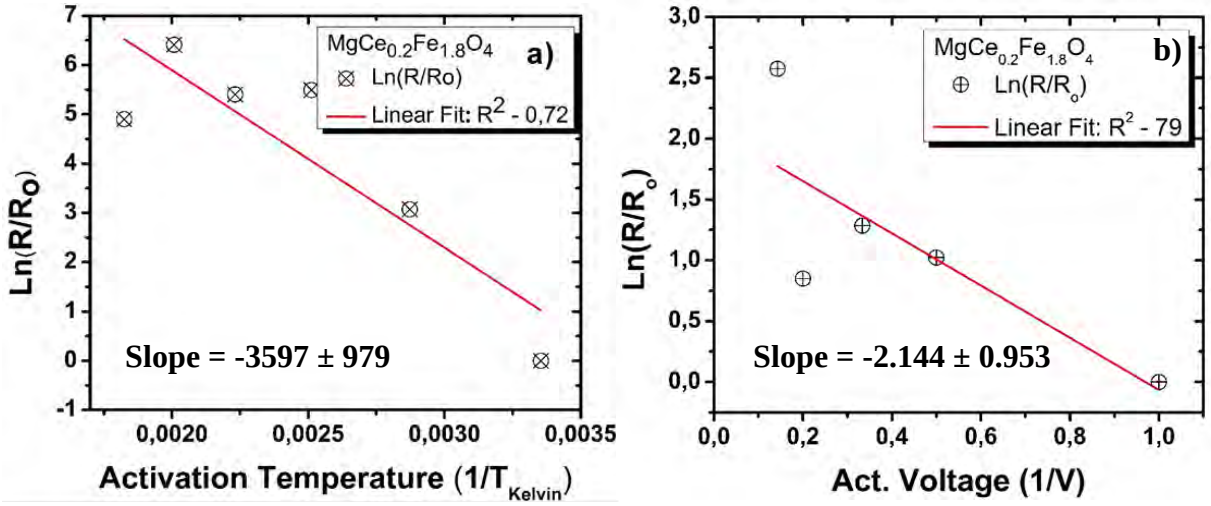

Figure 5. 6: (a) Activation temperature and **(b)** bias voltage for the $MgCe_{0.2}Fe_{1.8}O_4$ nanoferrites sensor.

There is a close relationship between temperature and electric potential, $V = k_B T / q$, where k_B represents the Boltzmann constant, T is the absolute temperature in Kelvin, and q is the electric charge. This suggests that as the thermal voltage is applied to the carrier-charges forcing them to begin movement; their internal temperature increases due to their many collisions and friction, or Joule heating **[9]** or the working temperature invoke thermal voltage. Consequently, we can have activation energy from the applied voltage to increase the conductivity. The part in the exponent of **Eq. 5.2** is just energy ratio, $\Delta E_A/k_B T$. Instead of the temperature we can have the potential difference, ΔV, which again is $\Delta E_A/k_B \Delta V$, another energy ratio now due to the

applied bias voltage. The activation energy due to the applied bias voltage is given by the following relation:

$$R = R_0 e^{-\Delta E_A / k_B \Delta V} \qquad \text{Eq.....5. 3}$$

$$LnR = LnR_0 - \Delta E_A / k_B \Delta V \qquad \text{Eq.....5. 4}$$

where ΔV is the minimum electric potential difference needed to move a charge and increase the conductivity. Again, the plot of LnR vs. $1/\Delta V$ is shown in **Fig. 5. 6(b)**. From the extrapolated slope (-2.144), the minimum activation energy due to applied bias voltage was calculated to be ΔE_A = 0.000185 ± 0.000001 eV (1.85×10^{-4} eV). This activation energy is much smaller than the earlier energy due to a temperature which is over 1600 times more.

Another important property to introduce in the chemical gas sensors is reversibility. It is the ability of a sensor to recall its previous gas concentration even if the order of concentrations is changed to a reverse order. It is not given and clear that any order of gas concentration introduced inside the sensing chamber can yield the same response corresponding to its concentration. **Fig. 5. 7(a-b)** demonstrates the repeatability and reversibility order of 5 and 100 ppm and 100 and 5 ppm concentrations towards the acetone vapours operated at sensor's temperature of 225 °C. Dry-air and argon (Ar) gas was used as carrier gases and for dilution.

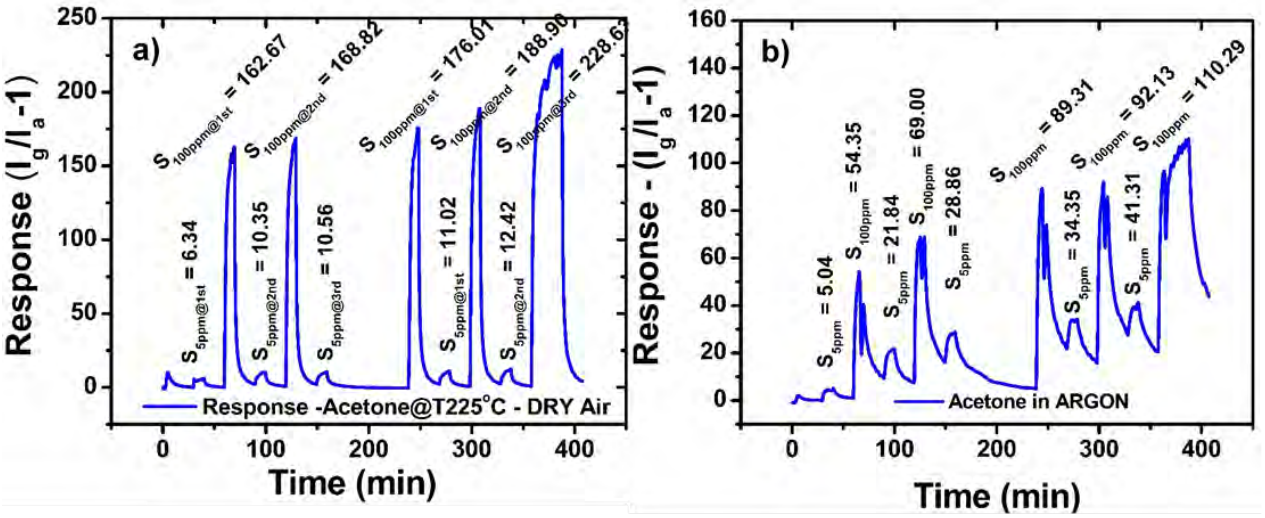

Figure 5. 7: Repeatability and reversibility of 5 & 100 ppm and 100 & 5 ppm cycles of acetone concentration of the Ce-doped magnesium ferrite at 225 °C under **(a)** dry-air and **(b)** argon-gas.

The first set of acetone concentrations consists of 5, 100, 5, 100, and 5 ppm repeatability followed by 30 minutes break under dry-air as shown in **Fig. 5. 7(a)**. Again, in a reverse order of the second set of concentrations was the 100, 5, 100, 5, and 100 ppm concentrations to test the reversibility of the magnesium ferrite based sensor of the same figure. The average response on the 5 ppm and 100 ppm from the 1st sets of concentrations was $\mathbf{S_{5ppm} = 9.1}$ and $\mathbf{S_{100ppm} = 165.7}$. The 2nd sets of concentrations 100 and 5 ppm in a reverse order recorded average responses of $\mathbf{S_{100ppm} = 197.9}$ and $\mathbf{S_{5ppm} = 11.7}$, respectively (**Fig. 5. 7(a)**). There appeared to be an increasing trend of the response from the 1st to the 2nd set, both in the 5 and 100 ppm concentrations. This overall response increase could be due to more reactive sites activated on the surface of the sensor after each acetone gas exposure. However, the sensor showed a very good reversibility and excellent repeatability. It should be noted that these measurements were conducted long (60 days) after the initial measurements. The same set of measurements presented in electrical current instead of response is shown in **Fig. 5. 8**.

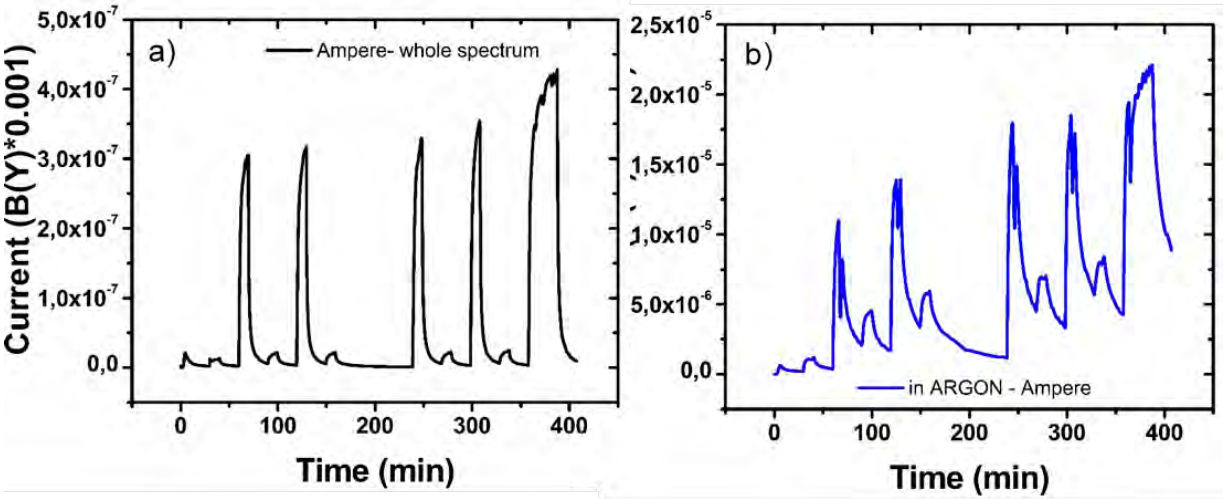

Figure 5. 8: Transient current curves of the repeatability & reversibility of 5 & 100 ppm of acetone concentration in **(a)** dry-air and **(b)** Argon-gas.

Fig. 5. 7(b) shows a similar type of experiment now using argon as carrier gas and for dilution. This demonstrates the sensor functionality and capability under oxygen reduced environments to test the same repeatability and reversibility. Generally, the acetone responses are low both in the 5 and 100 ppm concentration. The sample, again, showed excellent reversibility and repeatability even under oxygen reduced environment. The low responses can be attributed to the fewer chemisorbed oxygen species on the sensor's surface to interact with the acetone gas molecules. The slightly higher values of the 5 ppm concentration responses could be due to the drifting and longer recovery times after 100 ppm concentration. Therefore, the sensor could not fully recover to its initial electrical current or resistance. The necessity of longer time breaks in between the acetone exposure cycles is demonstrated in the observed drifting of the transient current of the sensor. The transient electrical current curves are shown in **Fig. 5. 8(b)**. There was a difference in the electrical current in dry-air and argon (oxygen reduced environment), $\mathbf{I_{DRY\text{-}AIR} = 1.32 \times 10^{-9}/2.47 \times 10^{-9}}$ Ampère (ratio 0.5) and $\mathbf{I_{AR} = 1.24 \times 10^{-6}/2.42 \times 10^{-7}}$ Ampère (ratio of 5.1), respectively. These numbers suggest that the sensor in dry-air behaves as a semiconductor with high resistance, while when argon was used the sensor is metallic. The depletion layer is greater in dry-air than in argon. This is the reason the response is much higher

in dry-air than in argon. The depletion layer is caused by the oxygen species chemi-adsorbed on the surface responsible for the sensing. There is a noticeable dip in the response or transient current curve during the saturation stage for the 100 ppm concentration. This sharp dip always appeared at about 6 minutes of the acetone exposure. This was not the case when dry-air was used as carrier gas and dilution. This could be attributed to the physisorbed self-dissociation of water molecules on the surface. The reaction between acetone and the chemisorbed oxygen species leads to carbon dioxide and water molecules, and possibly some electrons are also released back into the conduction band. However, this will be discussed later in the sensing mechanism section.

The electrical current increased upon exposure to the acetone reducing gas. This, therefore, suggests that the Ce-doped magnesium ferrites are n-type majority charge-carrier semiconductors. This n-type confirmation further suggests that these Ce-doped magnesium ferrites are normal spinels. The spinel ferrites, as discussed earlier in the introduction, consist of tetrahedral and octahedral cation sites. For normal spinels the tetrahedral site contains 2+ electronic charge which is Mg in our case and the octahedral site has 3+ cations which is Fe and substituted by Ce. Under the current environment, gases exposure, Ce substitution and temperature variation, the spinel maintained its normality.

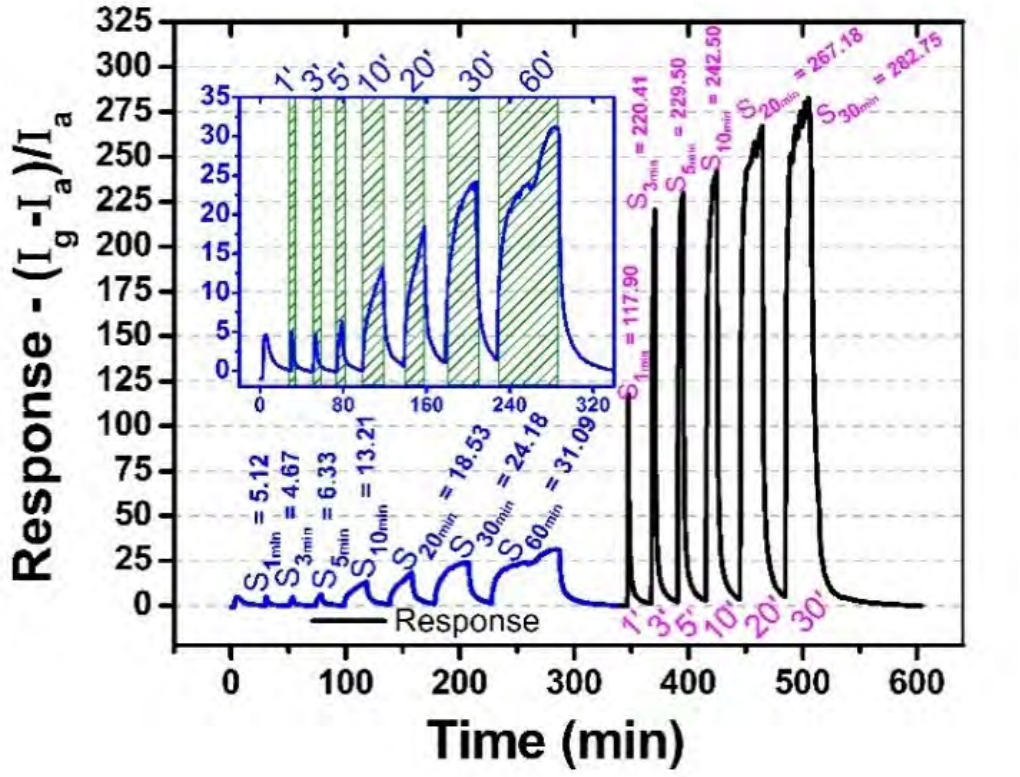

Figure 5. 9: Dependence of response to different exposure-times of acetone vapours of 5 & 100 ppm concentrations.

In a quest to have a deeper insight on the properties of the sensor, we performed exposure time measurements to test our magnesium based ferrite sensor during acetone monitoring. **Fig. 5. 9** shows 5 and 100 ppm concentrations of acetone at 225 °C towards various exposure times (1, 3, 5, 10, 20, 30, and 60 min). The $MgCe_{0.2}Fe_{1.8}O_4$ nanoferrites based sensor exhibits a linearity on the response and exposure times. The 5 ppm recorded a high response of **S_{1min} = 5. 12**, exposed to 1 min acetone. The response continues to rise with increasing the acetone exposure times up to 60 min. The responses at 30 and 60 min were **S = 24.18** and **31.09**, respectively. Similarly, the response at 100 ppm against the acetone exposure times shows a very high response of **S_{1min} = 117.90** at 1 min. The response increases linearly above 200 from the exposure time of 3 min. This suggests that the sensor contains many active sites on the surface that require sufficient time to be accessed. This demonstrates good signs that these normal spinel ferrites possess great capability to be utilised as acetone detection and monitoring even

in a reduced oxygen environment. **Fig. 5. 10** and **5. 11** show the electrical current values in dry-air, acetone, and responses at 5 and 100 ppm concentrations, respectively.

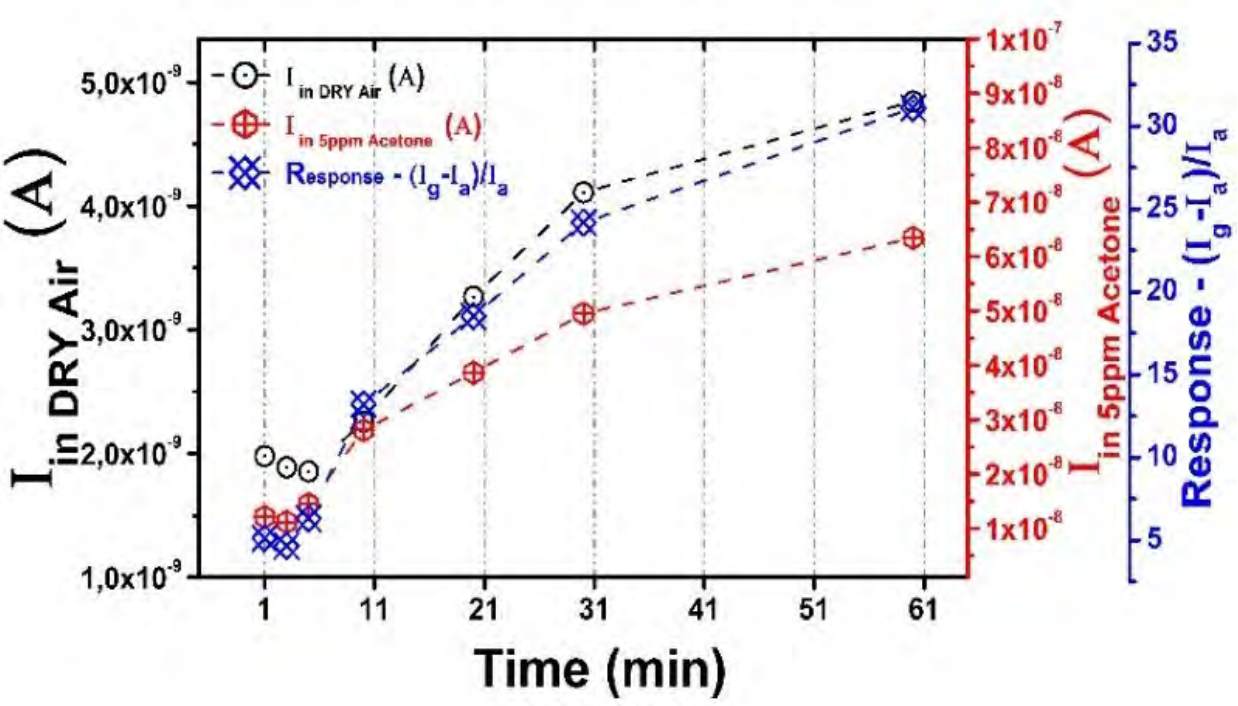

Figure 5. 10: Current of the sensor in dry-air, acetone, and response with different exposure-times for the 5 ppm concentration.

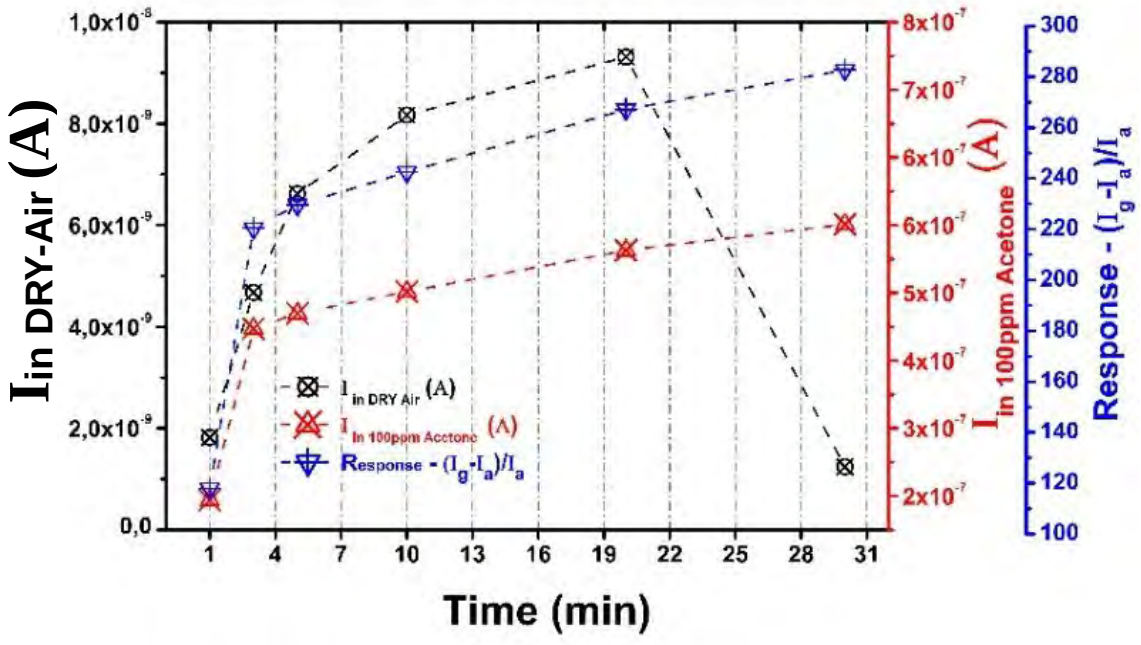

Figure 5. 11: Current of the sensor in dry-air, acetone, and response with different exposure-times for the 100 ppm concentration.

There exists a general increase in the current values in both dry-air and acetone for both the concentrations, 5 and 100 ppm. The electrical currents for the 5 ppm concentration are in the nano-Amperes range and increase with the acetone exposure to the micro-Amperes range (see **Fig. 5. 10**). Whereas, for the 100 ppm concentration, the currents are slightly higher near 10-8 A (see **Fig. 5. 11**). The current in dry-air at 30 min of acetone exposure time showed a drastic drop. **Fig. 5. 12** demonstrates the sensor's working sustainability over a long-term period to acetone gas over 100 ppm concentration. **Fig. 5. 12** not only shows the acetone's response over a period of 120 days, but also the evolution of both electrical currents in air and acetone. These latter two parameters are the main contributors to the sensor's response. The electrical current in acetone increased significantly over time after 40 days. Meanwhile, the current of the sensor in air is not stable but fluctuating over the time in a disordered manner. The magnesium ferrite-based sensor still maintains a very high response of over 200 from the initial response of above 500 even after 120 days.

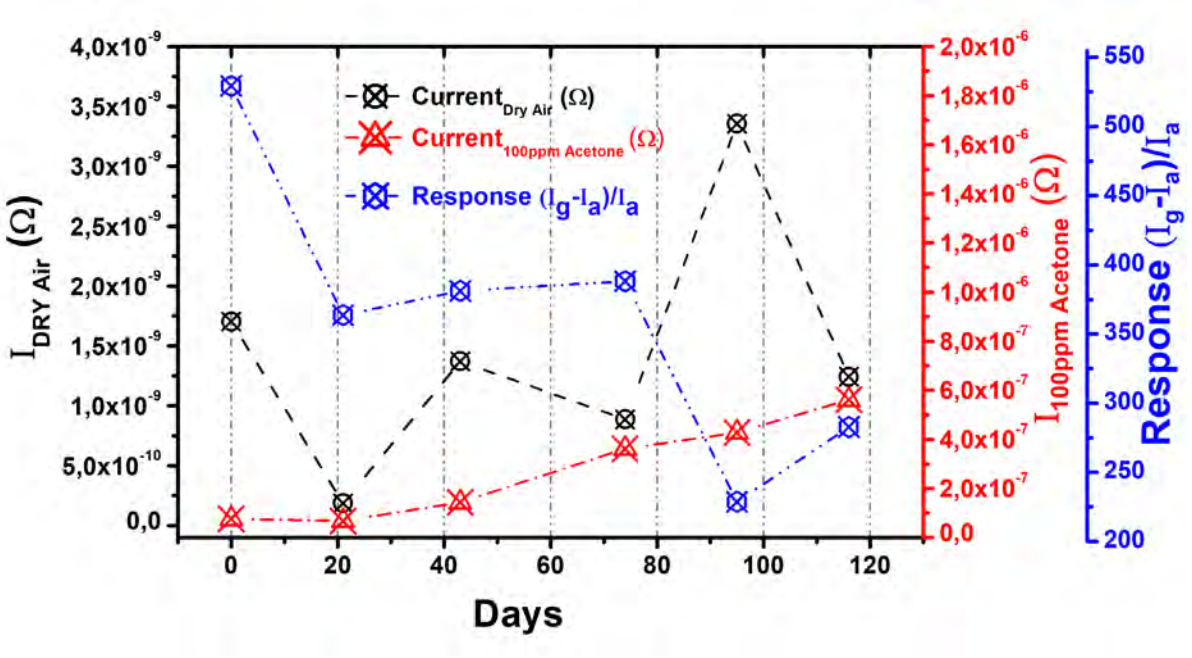

Figure 5. 12: Long-term sustainability of the Ce-doped magnesium ferrite at its optimal working temperature of 225 °C.

This magnesium ferrite based sensor compares very well with other acetone sensors over a wide range of concentrations. **Table 5.1** and **Fig. 5. 13** show acetone's response over a wide

range of concentrations, up to 50 ppm. **Table 5.2** and **Fig 5. 14** show the response for 50 to 500 ppm. Our sensor over 100 ppm concentration was still the highest compared to other acetone sensors over the same concentrations range. Again, our sensor compares very well over 5 and 50 ppm concentrations with responses of 9 and 48, respectively. Literature comparisons of extremely high acetone responses of over higher concentrations above 500 ppm are shown in **Fig. 5. 15** and **Table 5.3**.

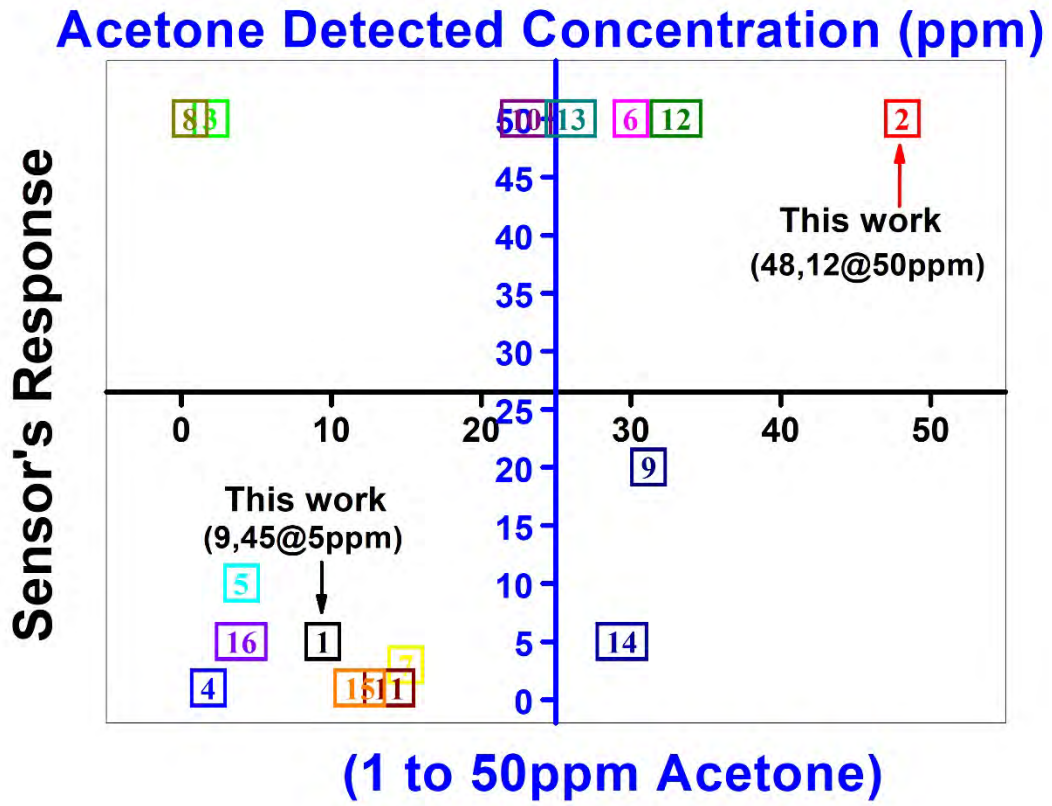

Figure 5. 13: A comparison of present work with reported data for 1 up to 50 ppm concentration.

Table 5. 1: Reference List for Literature Survey – Up to 50 ppm Acetone Concentrations.

Number	Sensor's response	Detected concentration	Operating temperature	References

1	9,45	5	225	**This work [10]**
2	48,12	50	225	**This work [10]**
3	1,96	50	35	**[11]**
4	1,8	1	350	**[12]**
5	4	10	160	**[13]**
6	30	50	240	**[14]**
7	15	3	230	**[15]**
8	0,6	50	375	**[16]**
9	31,2	20	200	**[17]**
10	23	50	280	**[18]**
11	13,86	1	220	**[19]**
12	33	50	240	**[20]**
13	26	50	240	**[21]**
14	29,4	5	350	**[6]**
15	11,92	1	220	**[22]**
16	4	5	25	**[23]**

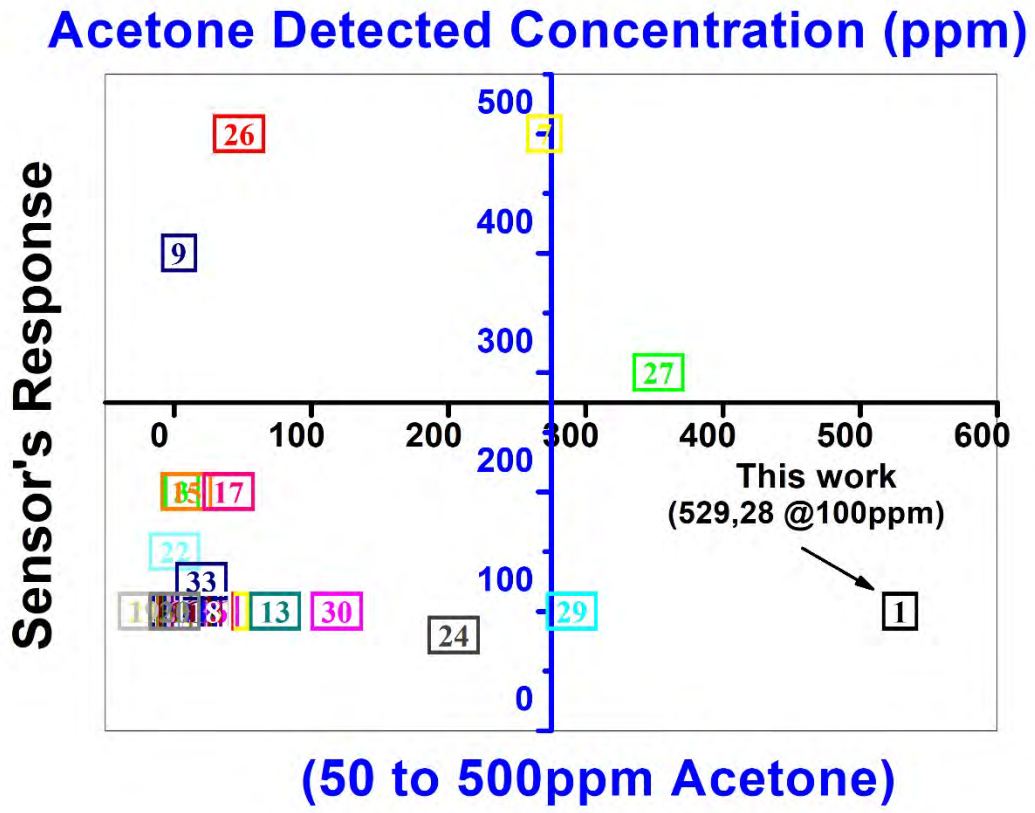

Figure 5. 14: A comparison of present work with reported data for 50 to 500 ppm acetone concentration.

Table 5. 2: Reference List for Literature Survey – 50 to 500 ppm Acetone Concentrations.

Number	Sensor's response	Detected concentration	Operating temperature	References
1	529,28	100	225	**This work [10]**
2	18,9	100	275	**[24]**
3	5,8	200	240	**[25]**
4	17,3	100	220	**[1]**
5	16	100	350	**[26]**
6	33,8	100	175	**[27]**
7	270	500	320	**[3]**

8	0,19	100	25	**[28]**
9	3,626	400	350	**[2]**
10	16,5	100	300	**[29]**
11	18,8	100	120	**[30]**
12	10,6	100	280	**[31]**
13	73,8	100	180	**[32]**
14	2,74	100	200	**[33]**
15	9	200	350	**[34]**
16	0,25	100	350	**[35]**
17	39,5	200	200	**[36]**
18	0,6	100	350	**[37]**
19	0,5	100	325	**[38]**
20	0,55	100	350	**[39]**
21	0,26	100	500	**[40]**
22	0,4	150	300	**[41]**
23	7,61	100	300	**[42]**
24	204	80	400	**[43]**
25	11,4	100	150	**[44]**
26	47,51	500	247	**[45]**
27	353	300	260	**[5]**
28	12,5	100	240	**[46]**
29	290	100	280	**[47]**
30	118,8	100	200	**[48]**
31	35,6	100	150	**[49]**
32	0,35	100	25	**[50]**
33	20	125	450	**[51]**

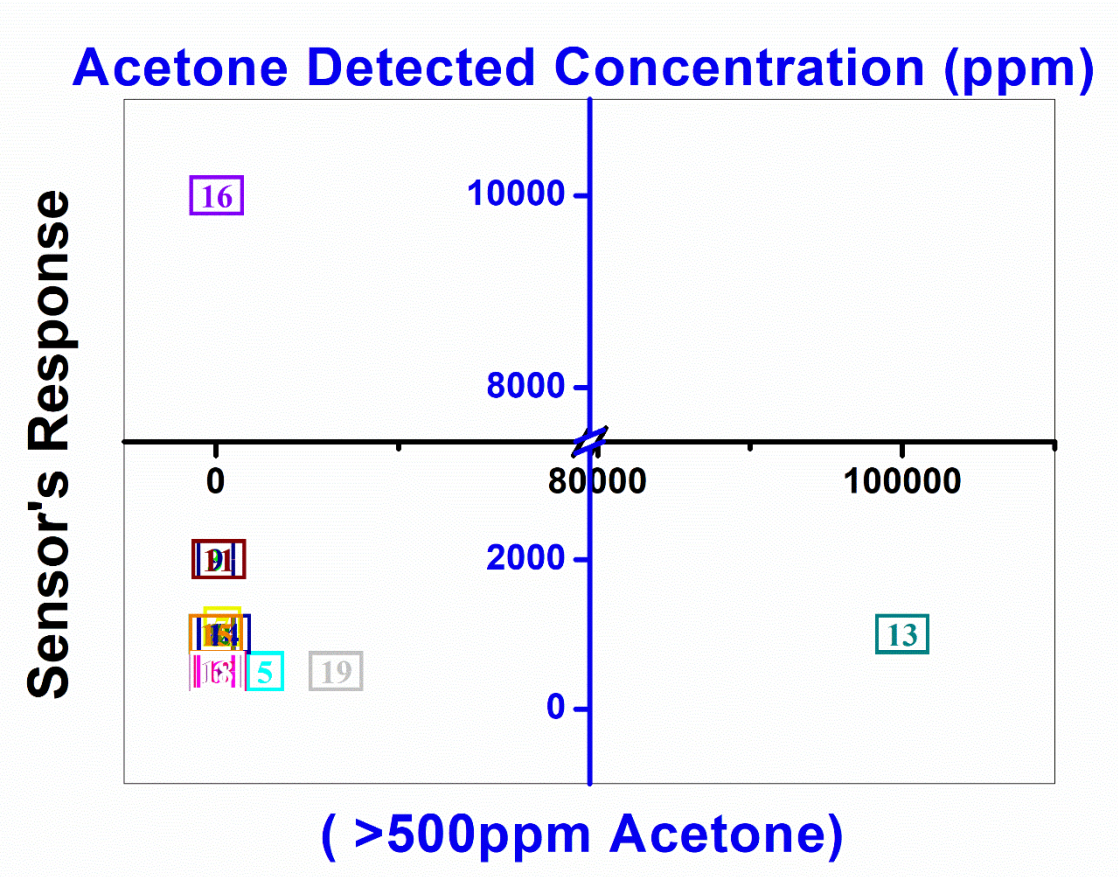

Figure 5. 15: Literature comparison of extremely high acetone responses of over higher concentrations above 500 ppm.

Table 5. 3: Reference List for Literature Survey – > 500 ppm ppm Acetone Concentrations.

Number	Sensor's response	Detected concentration	Operating temperature	references
1	0,5	1000	200	**[52]**
2	0,11	1000	25	**[53]**
3	0,87	2000	500	**[7]**
4	5	1000	350	**[4]**
5	270	500	320	**[3]**
6	0,77	500	25	**[54]**
7	36,5	1100	300	**[55]**

8	0,72	1000	250	**[56]**
9	0,57	2000	250	**[57]**
10	5,5	500	275	**[58]**
11	17,7	2000	225	**[59]**
12	0,19	1000	25	**[60]**
13	100000	1000	300	**[61]**
14	43	1000	300	**[62]**
15	3,3	1000	332	**[63]**
16	4,5	10000	215	**[64]**
17	19,3	500	240	**[65]**
18	8	500	240	**[66]**
19	657,7	500	140	**[67]**

Therefore, our sensor based on Ce-doped magnesium ferrite nanoparticles is suitable and can be recommended for acetone sensor device for commercialisation. However, further stability tests are in progress for at least long period of more than 6 months.

5.3 GAS SENSING PROPERTIES OF $MgCe_xFe_{2-x}O_4$ NANOFERRITES TOWARDS FLAMMABLE GASES

To investigate sensing capabilities of cerium doped magnesium ferrite ($MgCe_xFe_{2-x}O_4$) towards flammable gases, the KINOSTEC gas sensor testing system was used. Sensors of magnesium doped with different cerium composition (x= 0.0, 0.05, 0.1and 0.2) were exposed to various flammable gases such as methane, propane, butane, hydrogen, ammonia, and liquefied petroleum gas (LPG). The optimal operation temperature of 225℃ was used and bias voltage of 5V, while different ranges of concentrations for different gas analytes are according to the

recommended and detection exposure limits (REL/DEL) of the National Institute for Occupational Safety and Health (NIOSH) **[7, 68, 69]**.

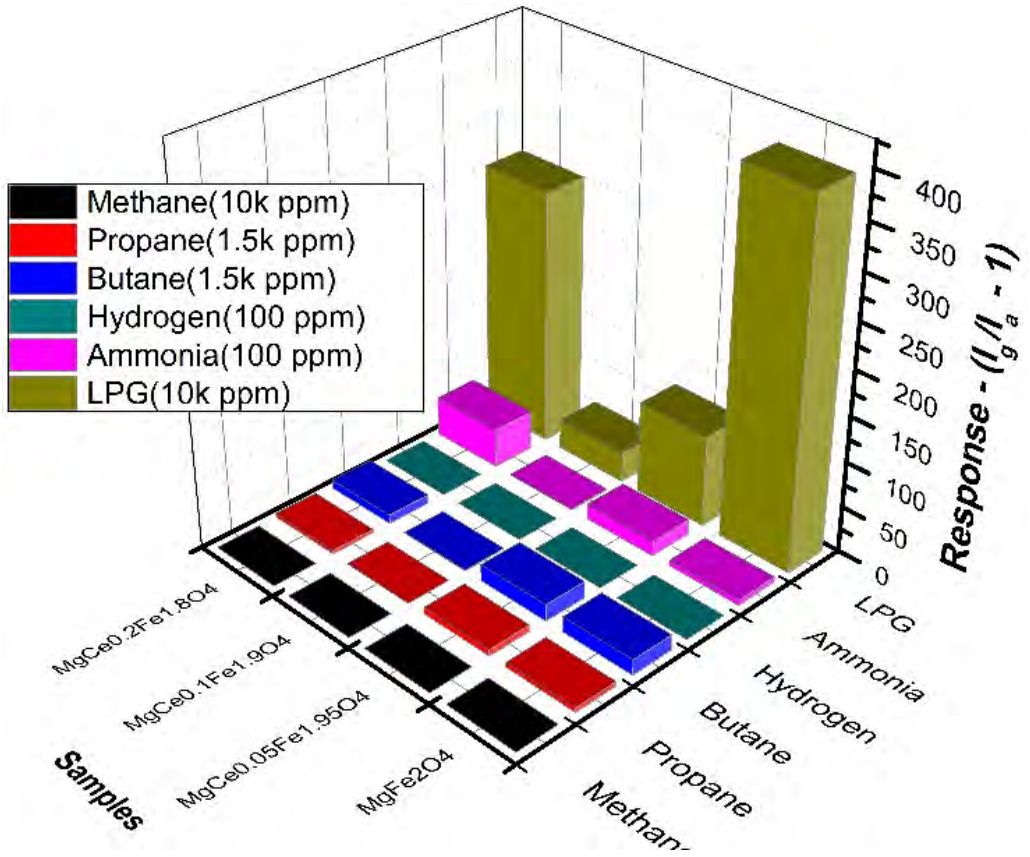

Figure 5. 16: Selectivity 3D plot of n-type $MgCe_xFe_{2-x}O_4$ spinel ferrites towards various flammable gases.

The 3D plot in **Fig. 5.16** depicts the gases response (S) of magnesium ferrites ($MgCe_xFe_{2-x}O_4$) doped with a rare-earth element, cerium (Ce). It is clear from **Fig. 5.16** that the liquefied petroleum gas (LPG) was substantially detected over a range of concentrations with the highest response **($S = I_g/I_a - 1$) of 395.47** at 225 °C operating temperature. It was also clear that the substitution of Ce into the magnesium ferrite octahedral sites is not really desirable as the response decreases with Ce ions increase. A slight increase in the response was observed for $MgCe_{0.2}Fe_{1.8}O4$ ferrite. This was attributed to the formation of secondary phases at this cerium content. It is noteworthy to mention that incorporating Ce as a dopant results in the formation of CeO_2 phase outside the original structure. The formed CeO_2 secondary phase becomes

predominant at x = 0.2, gradually replacing the Mg ferrite structure, as discussed earlier. The response at x = 0.2 (Ce) is now largely due to the CeO_2 phase which also possess an n-type characteristic.

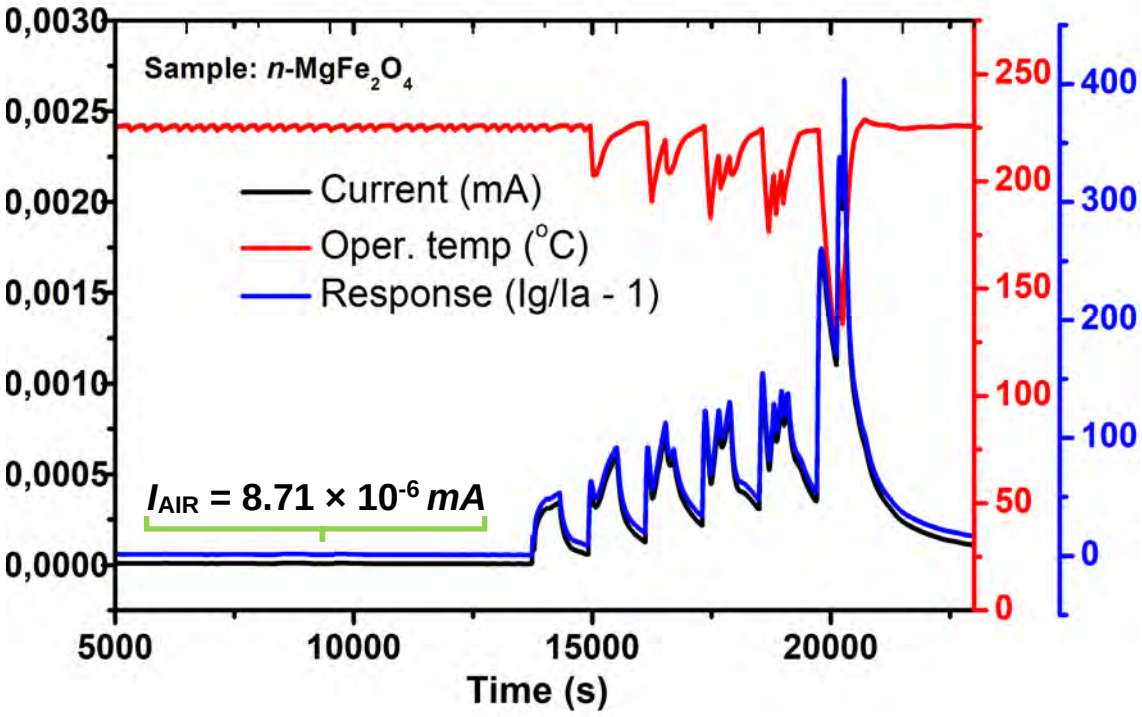

Figure 5. 17: Transient electrical current plot of $MgFe_2O_4$ towards different concentrations (1000 to 10 000 ppm) of selected LPG and oscillating operating temperature.

Fig. 5. 17 depicts the transient current of the best performing magnesium ferrite (i.e., the one with no cerium dopant) towards different concentrations of the LPG at 225 °C operating temperature. The steady current in air before gas was allowed into the chamber was $\boldsymbol{I_{air} = 8.71 \times 10^{-6}\ mA}$ ($\boldsymbol{R_{air} = 5.75 \times 10^{5}\ k\Omega}$). This value (**Fig. 5. 17**) was followed by the LPG dynamic response with concentration. There was also observed an interesting behaviour in the oscillating electrical current and fluctuating operating temperature during LPG sensing. However, these two quantities occurred in opposite directions to each other. It appears that the set operating temperature, 225 °C, drops subsequent to the oscillating electrical current during the gas analyte introduction into the chamber for a period of 10 min. It is noteworthy to mention that these fluctuations in operating temperature and oscillating current were only observed in

the presence of LPG analyte. Gumbi et al. **[69]** proposed a mechanism governing these processes. The authors did a series of experiments in an attempt to control these abnormal observations which they attributed to electronic and protonic conductions resulting from proton-transfer and formation of physisorbed self-dissociation water molecules on chemisorbed oxygen species on the sensor's grains' boundaries. **Table 5.4** depicts time-delays, *ß*, in the occurrence and observation of the oscillatory current and the fluctuating temperature.

Table 5. 4: The samples' responses, operating temperature drop during the 10 000 ppm LPG concentration and time delays between electrical current and operating temperature difference.

`	**Response, S**	**ΔT (ºC)**	**Time delay (β), s**	**$[S/\Delta T]_{avg}$**
$MgFe_2O_4$	395.47	101.4	53.44	3.37
$MgCe_{0.05}Fe_{1.95}O_4$	100.82	107.9	10.8	0.83
$MgCe_{0.1}Fe_{1.9}O_4$	33.14	105	35.63	0.19
$MgCe_{0.2}Fe_{1.8}O_4$	281.11	105	246.62	2.20

REL - 10 000 ppm LPG concentration temperature drop

The time delays for other concentrations lower than the 10 000 ppm are shown in **Table 5.5**. It is clear from these tables that there was a bigger temperature difference at higher gas concentrations than lower concentrations. However, there was no temperature fluctuation or difference when 1 000 ppm or lower concentrations were used (see **Fig. 5. 17**). It should also be noted that the operating temperature drop comes soon after the gas analyte was introduced inside the sensing chamber and then returns to 225 °C in dry air. But it always comes after the electric current. There was no conclusive order in the time-delays at different gas concentrations and in the various sensor materials. This physisorbed water molecule multi-layered phenomenon appears to occur within ten to hundreds of seconds. This is a rather slow process.

Table 5. 5: LPG concentrations 1000 – 10 000 ppm, time-delays, operating temperature difference, and responses corresponding to each gas concentration of the $MgCe_{0.2}Fe_{1.8}O_4$.

Concentration (ppm)	Time delay (β), s	ΔT (ºC)	Response, S	S/ΔT
1000			29.22	
2000	60.03	21.60	51.16	2.37
3000	31.67	34.30	65.36	1.91
4000	72.25	43.50	81.06	1.86
5000	41.57	50.50	110.49	2.19
10000	28.71	105.00	281.11	2.68

The relationship between the sensor's response and gas concentration has been well studied and clearly established in literature following the Freundlich adsorption isotherm **[70-73]**. This relationship is a linear one and is influenced by many parameters, such as size, morphology, surface area and surface defects of the semiconducting metal oxide (SMO) **[70-76]**. This is important to determine the lower detection limit of a sensor. **Fig. 5.18(a)** shows the responses of six sensors to different concentrations. They also show linear characteristics. It is clear that, the $MgFe_2O_4$ responded intensely toward increasing LPG concentration with a rate of 0.038 ppm^{-1} (R^2 – 0.96). This is followed by the $MgCe_{0.2}Fe_{1.8}O_4$, showing a rate of 0.028 ppm^{-1} (R^2 – 0.97). These two sensors showed the highest LPG responses. The response of sensors towards different gas concentrations follows the power law of SMOs with the adsorption coefficient **[73, 77]**. The sensor's conductance is proportional to the gas concentration species adsorbed on the sensor's surface.

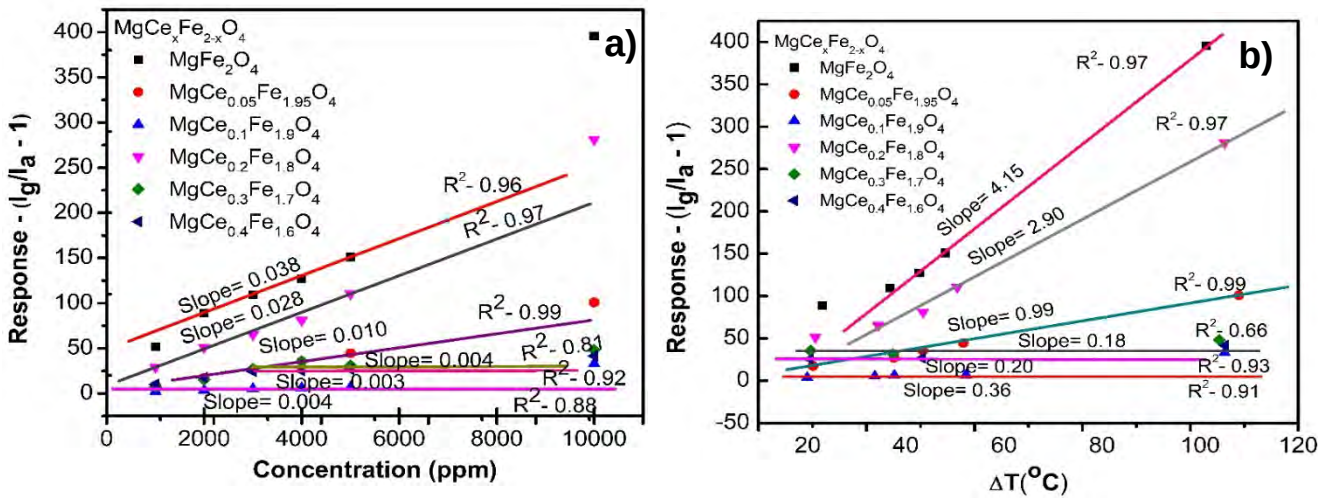

Figure 5. 18: (a) Linearity plot of the $MgFe_2O_4$ response (S) and the LPG concentration. **(b)** The operating temperature's differences during the LPG sensing and the gas response for the $MgFe_2O_4$ spinel.

This is described by Equation 5.5

$$S = K_f C^{1/n} \qquad \text{Eq.....5. 5}$$

where S is the sensor response, C is the gas analyte concentration, K_f is the Freundlich adsorption and n is the fitting parameter. Anand et al.**[73]** argued for a non-uniform behaviour of LPG concentration (50–1000 ppm) using Ag-doped In_2O_3 gas sensor, hence the Freundlich adsorption isotherm can explain this almost linear behaviour. In addition to this response-concentration relationship discussed above for the LPG and other gases, there is another established relationship between the response and the fluctuating operating temperature or temperature difference (ΔT) observed earlier in **Fig. 5.17**. **Figure 5.18(b)** shows a linear behaviour between response (S) and difference in the operating temperature (ΔT). It should be noted that, for all the samples, at 225 °C operating temperature the response to LPG was accompanied by this anomalous phenomenon within 10 min' gas exposure-time. A hypothesised mechanism was proposed by Gumbi et al. **[69]** on these ferrites and is also demonstrated in **Fig. 5.19**.

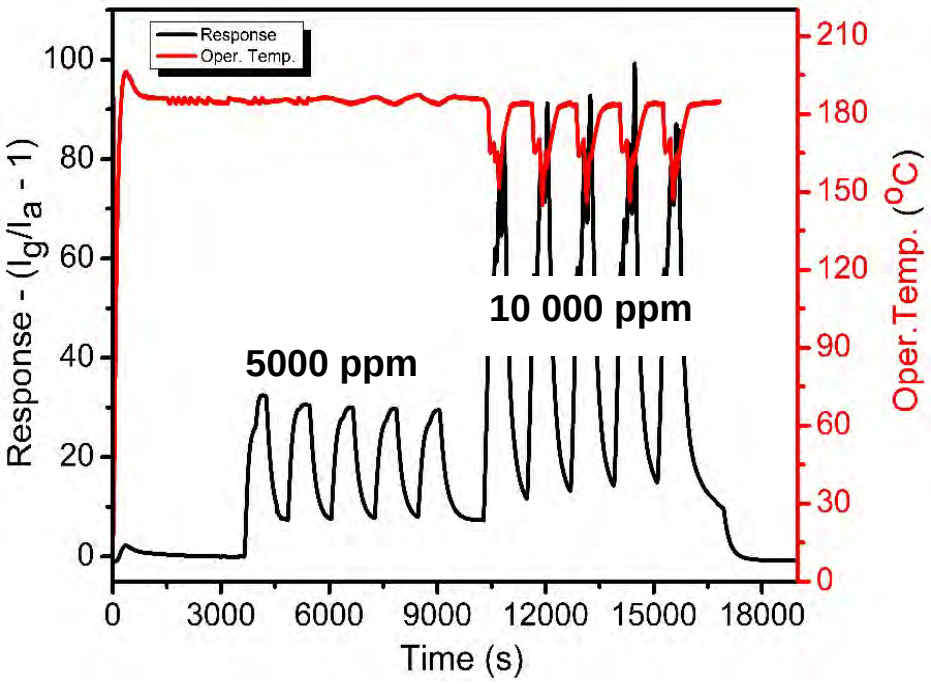

Figure 5. 19: Dry-air repeatability plot of 5 000 & 10 000 ppm LPG concentrations cycles for the $MgFe_2O_4$ at 185 ˚C.

In this case, it is assumed that the sensor response due to the oscillations (S_{OSC}) is directly proportional to the difference in the operating temperature.

$$S_{OSC} \alpha \Delta T \qquad \text{Eq.....5. 6}$$

where S is the sensor's response and $\Delta T = T_f - T_{225°C}$ is the difference in the operating temperature fluctuation in degrees Celsius. $T_{225°C}$ in this case is the optimum operating temperature and T_f is the final temperature from which it starts to increase again, following the sensor's response. There are clear heat transfer processes and rate of processes at play. These are also known as transport theory or kinetics. There are different modes of heat transfer, namely: radiation, convection, and conduction. In this case, we propose heat transfer by direct contact at the molecular level without defining each of the above mentioned processes. Our assumption of heat transfer by conduction is in line with the hypothesised mechanism proposed elsewhere **[71]**. Conduction can happen through gas, liquid or solid. In gas or liquid, the heat transfer happens through collisions of molecules. However, in solids, the lattice vibrations are

the medium of heat or energy transfer. In other special cases like metals, the electrons responsible for electrical conduction also tend to be good heat conductors. Regardless of the fundamental details of Thermal physics discussed, a mathematical law that governs these heat transfer and rate of heat transfer should not be hard to construct by carefully considering all parameters involved.

Imagine a temperature difference (ΔT) between the hot sensing surface and the multi-layered self-dissociation water molecules. There would be a heat transfer (Q) between the two surfaces in contact. Heat spontaneously flows from hot surfaces to cold surfaces. This suggests that there is energy (thermal) transfer until an equilibrium is reached, where $Q = 0$ or $\Delta T = 0$. The heat transfer is also directly proportional to the temperature difference. However, it should be mentioned that in this case, it would be difficult and unnecessary to talk about equilibrium because ΔT will not be equal to zero in the presence of LPG. The process will be in a transient state during the gas-in process. For the heat (Q) to be transferred between the two surfaces, a total surface area A should be considered through which this heat passes. Heat will be directly proportional to the sensor's total area, A, and to the time taken to pass through, Δt. However, the thickness of these multi-layered water molecules, Δx, which this heat must penetrate is inversely proportional to the heat. Putting together these quantities, we can express them in Equation 5.7 as

$$\Delta Q \; \alpha \; \frac{A \Delta t \Delta T}{\Delta x} \quad or \quad \frac{dQ}{dt} \alpha \; \frac{A dT}{dx} \qquad \text{Eq.....5. 7}$$

To have a complete expression of the situation, we need to have some proportionality constant which depends on the material through which the heat is transferred. This type of constant is called the thermal conductivity or coefficient of the material. Let's call it k_c (W/m·K). We can also put either a minus or a plus sign to distinguish that one object is losing heat to the other.

$$\frac{\Delta Q}{\Delta t} = -k_c A \frac{dT}{dx} \qquad \text{Eq.....5. 8}$$

This expression in **Eq. 5.8** should hold for heat transfer by conduction only. This equation is also known as the Fourier heat conduction law. The term $\Delta Q/\Delta t$ is the rate of heat flux not electrical current, *I*.

Fourier's law basically gives details regarding the rate of heat conduction that flows through another material in a right-angle geometry (1-D geometry). However, **Eq. 5.6** relates the sensor response (S or S_{OSC}) to the heat transfer or difference in the operating temperature. On the other hand, **Eq. 5.5** relates S_{OSC} to the gas concentration. It is possible to convert **Eq. 5.6** to the following expression:

$$S_{OSC} = K_c \Delta T \qquad \text{Eq.....5. 9}$$

where K_c in this case is a proportionality constant representing the thermal adsorption coefficient ($°C^{-1}$ or per unit Kelvin) of the sensor and is different from the constant of **Eq. 5.5**. Equating **Eqs ((5.5)** and **(5.9)),** allows us to estimate the proportionality constant, K_c, in **Eq. 5.9** with the fitting parameter $n = 1$ (for linear behaviour). In addition, **Fig 5.18(a)** shows the slopes for each sample.

It was interesting to note that these electrical oscillations and operating temperature fluctuations could also be controlled. At the same time, we conducted a reproducibility study towards both 5 000 and 10 000 ppm concentration of the LPG. **Fig. 5.19** shows these measurements done at 185 °C. It was clear that these oscillations and fluctuations were least eliminated at 5 000 ppm concentration and significantly reduced at 10 000 ppm concentration. At 225 °C, the operating temperature dropped to about 185°C and 115 °C at 5 000 and 10 000 ppm LPG concentrations, respectively. This was our only motivation for considering 185 °C as our new set temperature, to eliminate the oscillations and fluctuations especially when using 5 000 ppm concentrations. This proved to be effective, and it was clear that the operating temperature plays a crucial part in this observed oscillatory behaviour, although we could not conduct the experiment for 115 °C because the response (S) at this operating

temperature was low. Despite this, it would not be valid to conclude that these anomalies in current and operating temperature at 185 °C could never exist; delay may be implied. **Eq. 5.9** still holds even at lower temperatures, delay notwithstanding. Other very important parameters are the gas concentration (*C*) and the surface area (*A*) which the gas analyte covers. These are also proportional to the sensor response. Think about this: does it mean that our earlier established **Eq. 5.9** should be modified by introducing new parameters-gas exposure time, area of gas distribution and concentration, and thus generate **Eq. 5.10**?

$$S_{OSC} = \mp K_c AC\Delta t\Delta T. or\ . \frac{S_{OSC}}{\Delta t} = \mp K_c ACdT \qquad \text{Eq.....5. 10}$$

where Δt represents the time difference between the moment these anomalies are observed and gas-in. The S_{OSC} should be the sensor electrical oscillating response. In fact, this further suggests that **Eq. 5.5** containing the area of gas distribution would be more representative of the reality. The minus/plus signs in front of **Eq. 5.10** considers the whole complete process. Combining **Eqs. 5. 8** and **5 .10**, really should tell us that heat transfer (*Q*) is directly related to the sensor electrical oscillating response (S_{OSC}) or the sensor electrical conductivity with some coefficient product factor of concentration (*C*) and thickness (Δx).

These analyses and experimental observations clearly point out that the gas concentration (*C*) and the difference in the operating temperature (ΔT) are directly proportional to each other. **Table 5.6** shows these extracted parameters of response, concentration, and temperature difference. By fitting a linear progression on the first peaks of each concentration in **Fig 5. 17**, we find a slope or rate with units, °C/s. From this information, one can calculate the time difference (Δt) corresponding to each concentration. This information is also shown in **Table 5.6.**

Table 5. 6: The summary of the extracted S, k, ΔT, and Δt quantities.

LPG Concentration	Response	Slope k, (°C/s)	ΔT	Δt
1000	51.58	0.3259	19	58
2000	88.99	0.3763	23	61
3000	109.19	0.3404	36.8	108
4000	127.05	0.3354	42.8	128
5000	151.02	0.3300	48.1	146
10000	395.47	0.2707	101.3	374

In fact, this rate can be expressed as follows:

$$\frac{\Delta T}{\Delta t} = k_{-} \qquad \text{Eq.....5. 11}$$

where k_{-} is the rate in °C/s at which the temperature decreases. The minus subscript on the *k* signifies a temperature drop or decrease. In fact, **Eq. 5.11** is a simple heat equation. It should be noted that at 1000 ppm LPG concentration (see **Fig 5.17**), current oscillating and operating temperature fluctuation was not observed. Our argument was that these anomalies (at the 1000 ppm concentration) were delayed as 10 min' exposure-time was insufficient. Using the information given in **Table 5.6** to plot Δ*T* against *C*, a linear relationship is established with 0.0095 as a slope. From any two data points of quantity, Δ*T* and corresponding values of *C* (**Table 5.6**), one can calculate a temperature value corresponding to a particular concentration at which the temperature drop anomaly may occur. The estimated temperature differences at 1000 ppm concentration were: 10, 13, 15 or 18 °C. From these estimations, the temperature drop will be the difference between 225 °C and 215, 212 or 207 °C. This suggests that, given exposure time of more than 10 min towards the 1000 ppm LPG concentration, the oscillation in the current and fluctuation in the operating temperature will be observed. The temperature will drop to a value within the range 207-215 °C. The rate of heat transfer (Q/Δ*t*)

is related to the rate ($\Delta T/\Delta t$) in **Eq.5.11** by considering the heat (Q) transfer formula, $Q = mc\Delta T$, where m and C are mass and specific heat capacity constant. Now, dividing this heat formula by Δt on both sides, yields the following:

$$\frac{Q}{\Delta t} = mc\frac{\Delta T}{\Delta t} \; or \; \frac{Q}{\Delta t} = mck\_ \; or \; \frac{k_c A \Delta T}{\Delta x} = mck\_ \qquad \text{Eq.....5. 12}$$

The thermal conductivity or coefficient of the material constant, k_c, in Eq.5.8 has a unit of W/m·K. As mentioned earlier, the electrical conductance (G) of a material has unit of W/m^2·K. These two are also related by the following equation (**Eq.5.13**):

$$G = \frac{k_c}{\Delta x} \qquad \text{Eq.....5. 13}$$

Equation 5.13 really directly relates the heat transfer and electrical conductivity of the same material. This, therefore, yields the following:

$$\frac{\Delta Q}{\Delta t} = -GA\Delta T \qquad \text{Eq.....5. 14}$$

where G is the material electrical conductance, and A is the surface area. It is very interesting that these experimental observations of electrical current or resistance and the operating temperature fluctuations are directly connected and can be easily expressed mathematically. Resistance is the reciprocal of the conductance.

$$R = \frac{1}{G} = \frac{\Delta x}{k_c} = -\frac{A\Delta T}{\Delta Q/_{\Delta t}} = -\frac{A\Delta t \Delta T}{\Delta Q} \qquad \text{Eq.....5. 15}$$

Eq.5.15 basically suggests that the term $\Delta Q/\Delta t$ (heat transfer rate) is just different local internal resistances between any two layers of the built-up water molecules. These resistances are inversely proportional to each other.

On the repeatability or reproducibility results in **Fig. 5.19**, the sensor response was stable and consistent at 5 000 and 10 000 ppm concentrations.

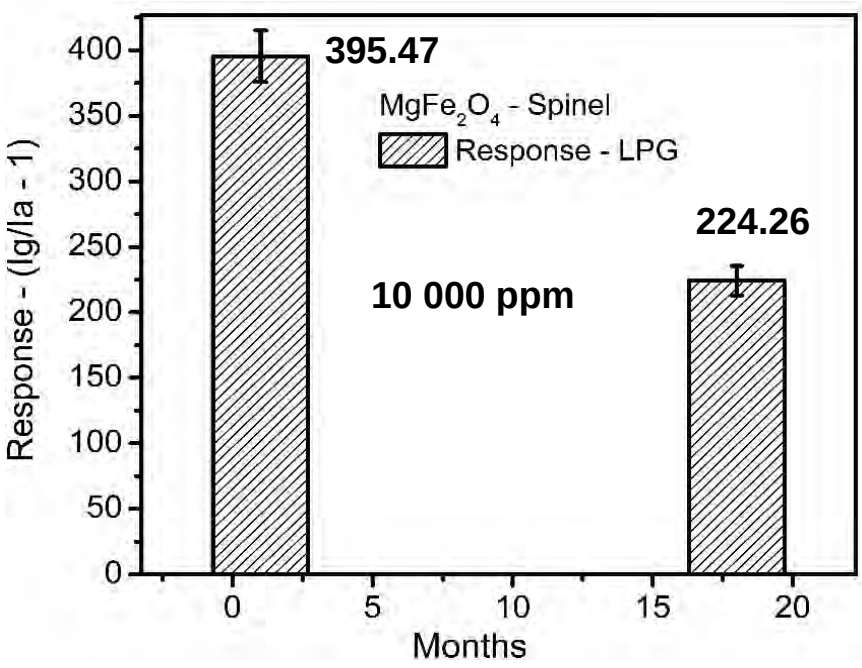

Figure 5. 20: long term stability in months of $MgFe_2O_4$ on LPG gas.

The long-term stability measurements (**Fig. 5.20)** demonstrate extremely stable sensor response over a period of 18 months. This was very good, more especially, in these SMOs type of sensors which rarely maintain their response for a few days or a month**[7, 68, 69]**. Our stability measurements shown in **Fig 5.20** surpassed any previously reported stability result.

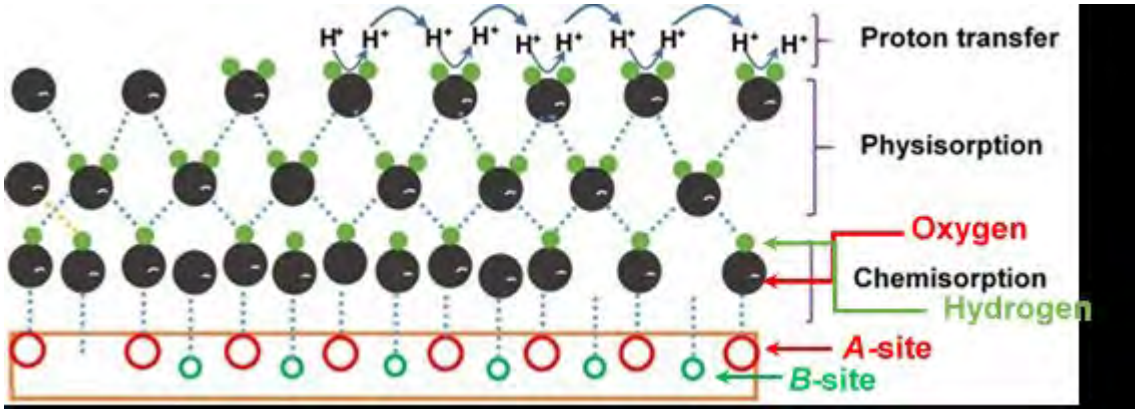

Figure 5. 21: Hypothesised mechanism for the self-dissociation physically adsorbed water molecules during sensing.

The hypothesised mechanism of the OH^--multi-layered build-up process in the sensor's surface is shown in **Fig. 5.21**. This model has been discussed elsewhere **[69]**. We believe that for these processes to take place, the chemisorbed oxygen molecules play a significant role. We designed an experiment to perform similar measurements (repeatability) at reduced oxygen ambient to observe and validate our proposed model in **Fig. 5.21**. Instead of using dry-air as carrier gas and for dilution, we opted for nitrogen and argon to create a reduced ambient. These two gases, with different atomic masses (Ar > N), are suitable for this experiment. **Fig. 5.22** shows the repeatability cycles of 5 000 and 10 000 ppm concentrations at 225 °C using nitrogen as a carrier-gas and for dilution of the LPG in the cylinder. Normally, for sensing to take place the surface or grain of the SMO sensor adsorbs different ionized oxygen species depending on the environment temperature. These chemically adsorbed oxygen species react with the target gas analyte, breaking it down to its components as by-products, hence an electrical signal in the form of current or resistance (chemiresistivity) is triggered. The detailed analysis of this process is discussed in the sensing mechanism section. Supposing one cuts the oxygen supply with an inert gas i.e., nitrogen or argon; it is clear from **Fig. 5.22** that the reduced oxygen available to initiate chemical reactions between those ionized oxygen species and the gas analyte could only produce a reduced response as compared to when air was used. The response dropped drastically to 5.4 towards 10 000 ppm concentration.

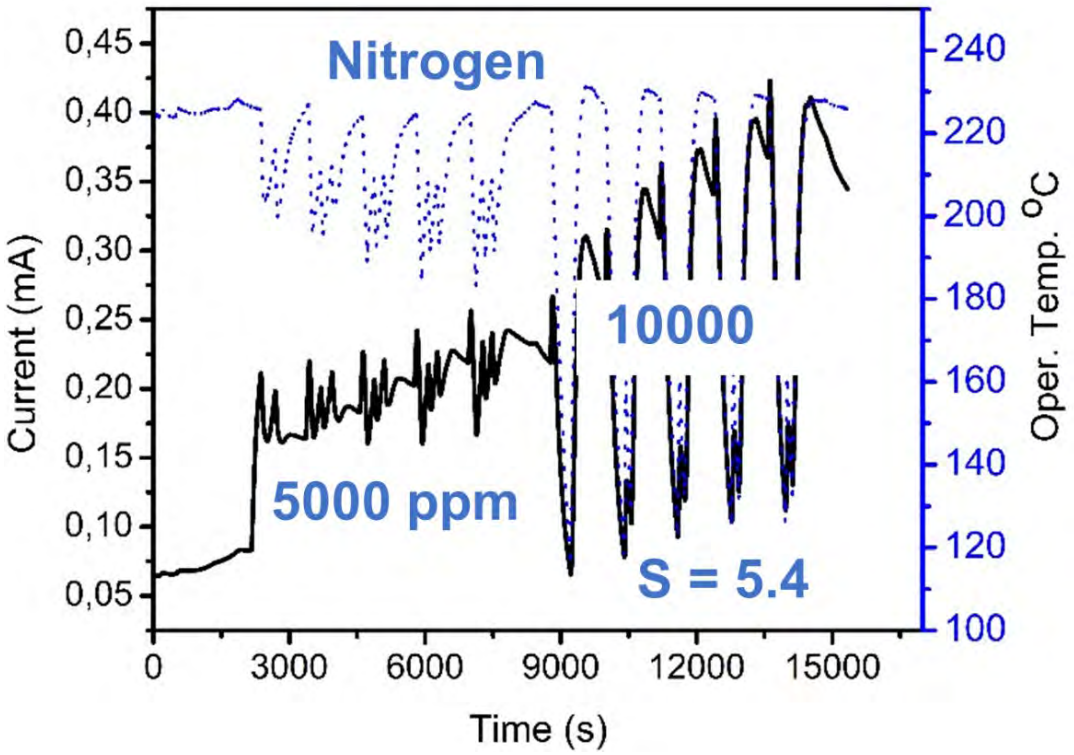

Figure 5. 22: Repeatability plot of 5 000 & 10 000 ppm LPG concentrations cycles (5) for the $MgFe_2O_4$ at 225 °C, with Nitrogen as carrier-gas.

It is interesting to note that those oscillations and fluctuation in the current and operating temperature were still present and observed. Also, the 10,000-ppm concentration-triggered current signal was reversed, decreasing instead of increasing as in dry-air. It was clear that at this point the surface structure has been changed to p-type because of deficiency in oxygen supply. This could only mean that the nitrogen employed as both carrier gas and to dilute the LPG somehow interacts chemically with these oxygen species, forming nitrogen oxides at the high temperature (225 °C). Both nitrogen and LPG gases compete for the available oxygen species. This is evident at the 5 000 ppm concentration. It was not clear whether the current wants to increase (up) or decrease (down) as it oscillates. The 1st 5 000 ppm concentration cycle seems to be clear (current 1st peak goes up) and as you go deeper in the cycles (3rd,4th, & 5th) the current peaks were alternating up at times and then down. This is due to the diminishing oxygen species, initially available on the sensor's surface, as more nitrogen molecules occupy the chamber. The fact that fluctuations in the operating temperature was still

observed without any hindrances was puzzling and interesting to note. Furthermore, using argon as carrier gas and for dilution should be analogous to our earlier explanation with minor details. **Fig 5.23.** demonstrates that argon was largely able to overcome oxygen species on the surface of the sensor and these oscillations and fluctuations in both current and operating temperature, respectively, were greatly reduced or eliminated.

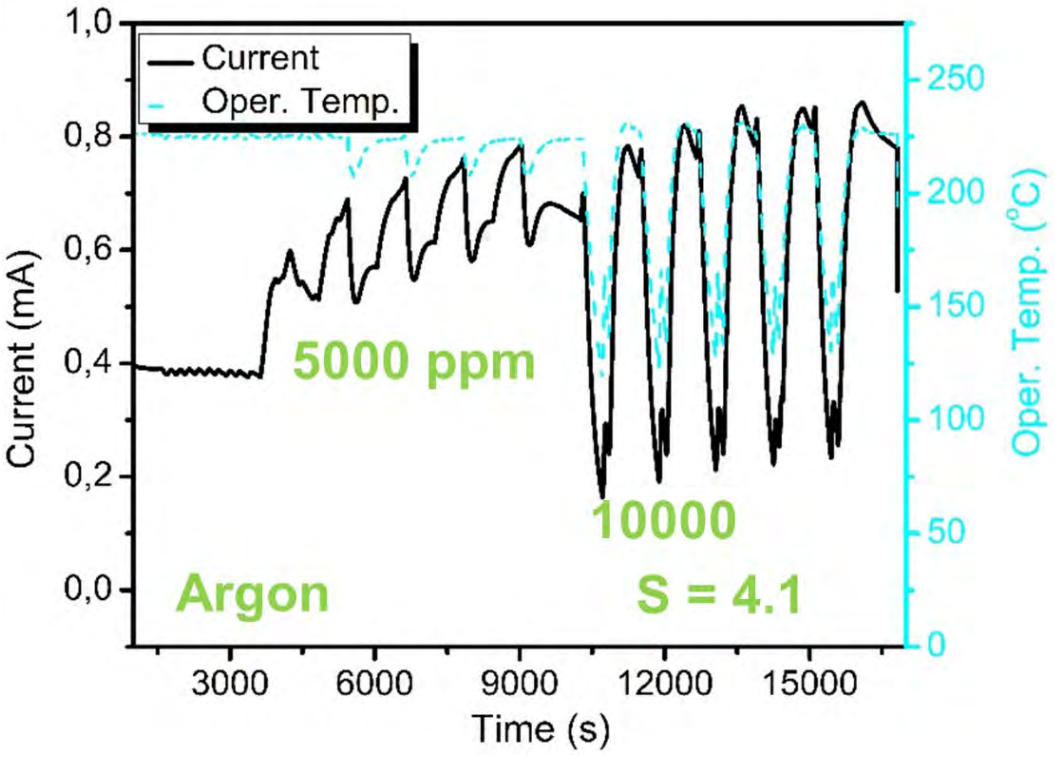

Figure 5. 23: Repeatability plot of 5 000 & 10 000 ppm LPG concentrations cycles (5) for the MgFe2O4 at 225 °C with Argon as carrier-gas.

However, the sensor response was reduced slightly to 4.1 towards the 10 000-ppm concentration. By comparing the responses at 5 000 ppm for both cases (nitrogen and argon), we discover that the response when using argon was better than when nitrogen was used as carrier gas. This can be attributed to the competition mentioned earlier between nitrogen and LPG interacting with oxygen. The 10 000 ppm concentration (**Fig 5.23**) triggered an inversion of sensor current upon gas introduction. This is a p-type sensor characteristic towards a reducing gas. These current reversal observed in both cases of nitrogen and argon as carriers for 10 000 ppm concentration can be explained by the adsorbed oxygen on the surface **[69]**.

The applicability of these inert ambient is important to understand the fundamental sensor behaviour in different environments that contain insufficient oxygen molecules.

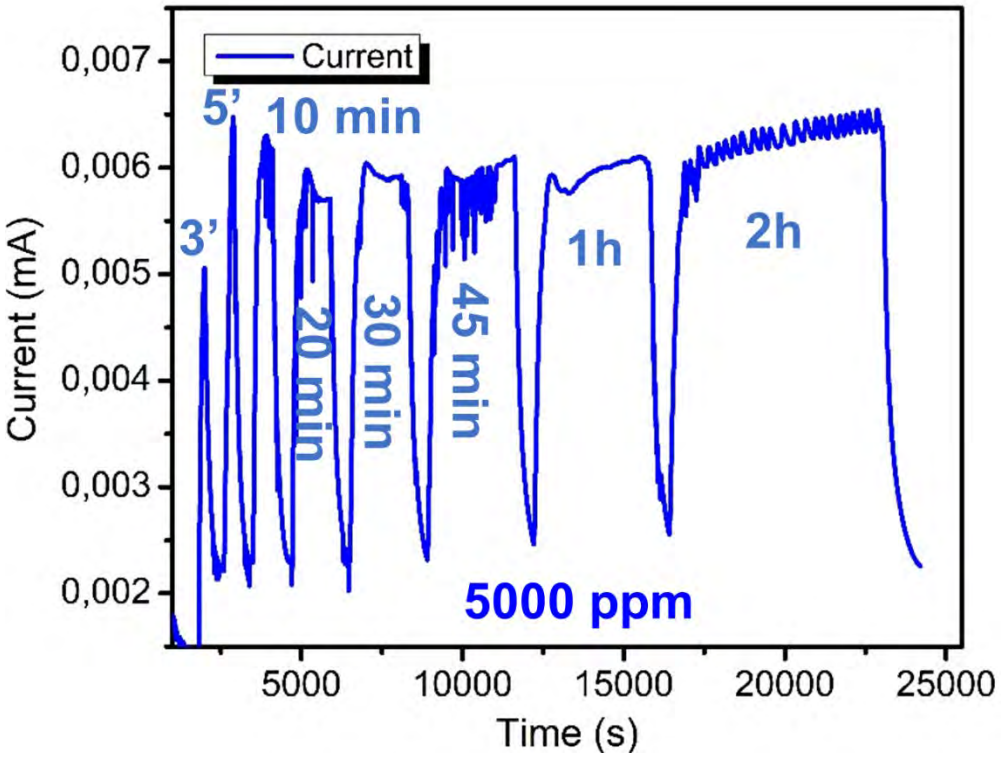

Figure 5. 24: long-term 5 000 ppm gas exposure at 185 °C. Note: The 3′ and 5′ represent 3 & 5 min (min).

Another very important aspect of gas sensing is the sensor's ability to detect and monitor our working and living environments. The World Health Organization (WHO) gives guidelines for air quality control – set limits on emissions and fuel combustion from heating stoves and cooking. **Fig. 5.24** shows the LPG detection and long-term monitoring measurements towards 5 000 ppm concentration at 185 °C. The LPG exposure times were 3, 5, 10, 20, 30, 45, 60, and 120 min. It was clear that the sensor was able to detect the flammable gas and maintain its steady state for the duration of the gas exposure time, i.e., 1 and 2 h. This part is often ignored by many researchers. It is crucial as many SMOs sensors degrade during continuous sensing, as shown elsewhere **[69]**. This steady-state balance in the current was due to the balance between the gas (5000 ppm) and dry-air supply.

Our earlier argument was that even at 1000 ppm concentration, these anomalies of current oscillation and operating temperature drop may occur, if given enough gas exposure time. Furthermore, using the information provided in **Table 5.6** we estimated how much the operating temperature could drop supposing enough exposure times are allowed towards the 1000 ppm concentration at the same temperature, 225 °C. We estimated the drop in the temperature to be between 207 and 215 °C. Now, conducting this experiment as shown in **Fig. 5.25** it shows transient currents towards the 1000 ppm LPG concentration. However, at different exposure times-two cycles, 10 min for each, a cycle for 30 min and a cycle for 60 min, it was clear, as expected, that in the first two cycles of 10 min, the anomalous phenomenon of current oscillation and operating temperature fluctuation did not occur at all. However, increasing the exposure time to 30 and 60 min, these anomalous current oscillations and fluctuating operating temperature were observed. The operating temperature dropped to 206 °C or by 19 °C. This observation concurs with our hypothesised proportion discussed earlier in the text.

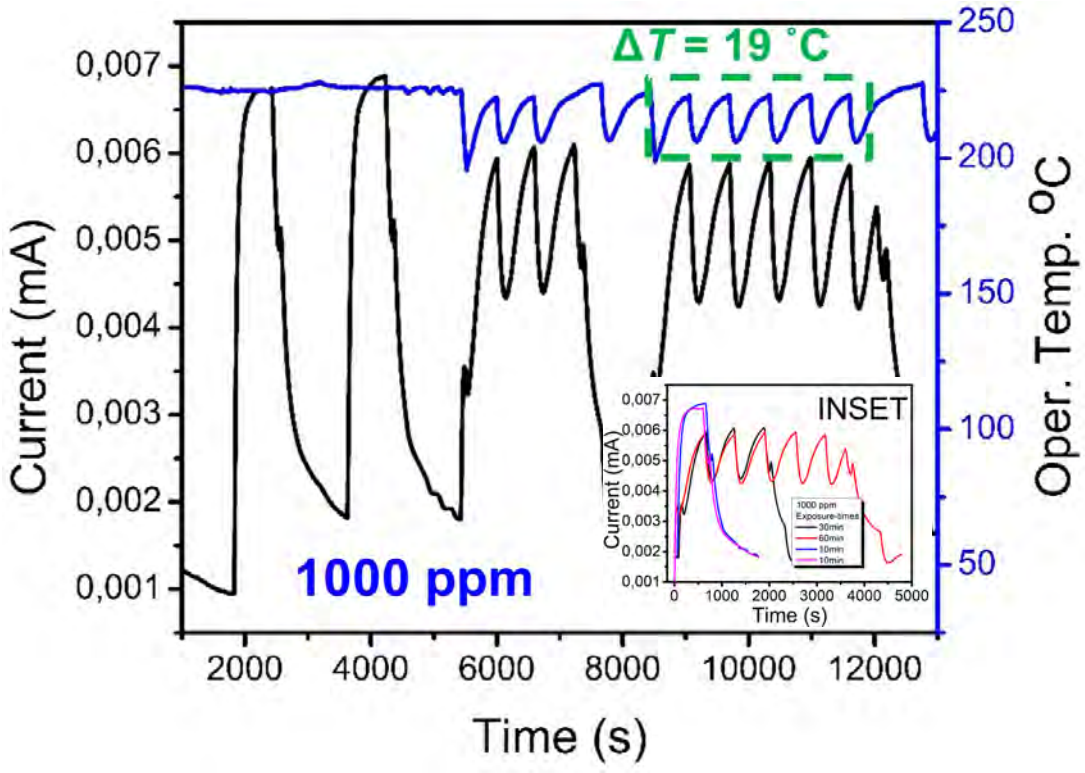

Figure 5. 25: Repeatability plot of 1 000 ppm concentration at 225 °C different exposure times, 2 cycles of 10 min each, 30 min and 60 min. **INSET**: All the graphs start at the same time.

However, something delusional was observed. It may appear as if these anomalies have a foresight at first by observing **Fig. 5. 25**. They seem to be appearing the moment current began to increase, especially for the long exposure time of gas. Meanwhile, at the short exposure time there was no oscillating current at all. This would suggest that these anomalous oscillations and fluctuations in current and temperature knew prior to the commencement of the experiment whether short or long exposure times were imposed. This suggests foresight. It is counter-intuitive and cannot be true. In fact, the inset of **Fig. 5.25** makes it clear by putting together all the plots of different exposure times. The plots have a common origin. In the first 10 min of the longer exposure times (30 and 60 min), current oscillation did not occur, it only began after 10 min of surface interaction. The sensor response for a short exposure time (S_{SE}) was less than for a long exposure time (S_{LE}), $S_{SE} > S_{LE}$.

Table 5. 7: Comparison of different sensor materials with respect to their operating temperatures and response to LPG.

Sensor Material	Concentration (ppm)	Operation Temperature(°C)	Response	Reference
Sn-$CuFe_2O_4$	20 000	25	78.78%	**[78]**
$NiFe_2O_4$	2000	27	2.1	**[79]**
$CoSm_{0.1}Fe_{1.9}O_4$	10 000	225	732	**[7]**
$Ni_{0.8}Cu_{0.2}Fe_2O_4$	2000	25	2.09	**[80]**
$MgFe_2O_4$	10 000	225	395.47	**This work[81]**

The troubling issue was the operating temperature fluctuations. They do not agree with our assertion that the oscillations appear later. The operating temperature drops appear a few

seconds after the gas was introduced into the chamber for the longer exposure times. This agreed with the foresight idea. It should be noted that these observations require extensive and rigorous experiments to confirm the many speculative ideas. **Table 5.7** shows the LPG sensitivity of our Mg-based ferrite sensor in comparison to some other spinel ferrites. It is obvious that $MgFe_2O_4$ possesses a high sensitivity towards LPG at 10 000 ppm concentration. This sensor also proved to be stable for over 15 months, as stated earlier.

5.4 CERIUM-DOPED MAGNESIUM FERRITE SENSING MECHANISM

It is a well iestablished fact that gas sensing happens at the surface of a semiconducting material containing oxygen species that are chemically adsorbed **[1-3, 12, 17, 27, 68, 82]**. The chemisorbed oxygen on the surface of the Ce-doped magnesium nanoferrites is ionized by capturing free electrons from the conduction band, thereby increasing the resistance (R_g) by creating a depletion layer. These oxygen species capture these free electrons to form adsorbed oxygen ions (O^{2-}, O^{-}, O^{-2}) and follow these reaction processes depending on the operating temperature **[17, 68]** :

$$O_{2(gas)} \rightarrow O_{2(ads)} \qquad \text{Eq.....5. 16}$$

$$O_{2(ads)} + e^{-} \xrightarrow{<100\,℃} O^{-}_{2(ads)} \qquad \text{Eq.....5. 17}$$

$$O^{-}_{2(ads)} + e^{-} \xrightarrow{100\,℃ < T < 300℃} 2O^{-}_{(ads)} \qquad \text{Eq.....5. 18}$$

$$O^{-}_{(ads)} + e^{-} \xrightarrow{>300℃} O^{-2}_{(ads)} \qquad \text{Eq.....5. 19}$$

In this work, the operating temperature was 225 °C, hence the dominant chemisorbed oxygen species are $O_{(ads)}^{-}$ (see **Eq. 5.18**). During the chemical gas sensing measurements the

magnesium ferrite based sensor was exposed to a reducing acetone vapour at 225 °C. Since this sensor is an n-type, the acetone reacts with the adsorbed oxygen ($O_{(ads)}^-$) to transfer electrons back to the magnesium ferrite conduction band:

$$C_3H_6O + 8O^-_{(ads)} \xrightarrow{225\,℃} 3CO_{2(gas)} + 3H_2O_{(vapour)} + 8e^- \qquad \text{Eq.....5. 20}$$

This reaction in **Eq. 5.20** will lead to a decrease in the depletion region thickness and a gain in the carrier concentration. Consequently, the electrical resistance (Rg) decreases during acetone exposure.

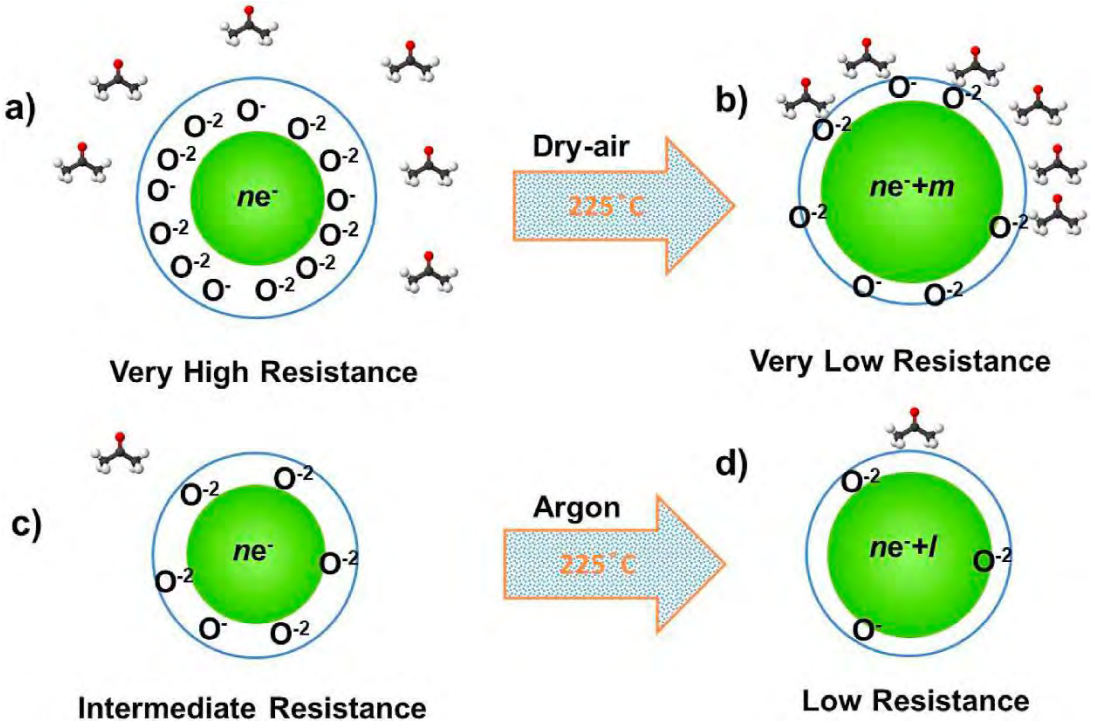

Figure 5. 26: A schematic diagram of the sensor's ($MgCe_{0.2}Fe_{1.8}O_4$) grain **(a)** before and **(b)** after the chemisorption of acetone gas using dry-air as carrier gas and for dilution, **(c)** in a reduced oxygen ambient environment using argon gas as carrier and for dilution before and **(d)** after the chemisorption of acetone.

Fig 5.26 illustrates the process leading to the redox reaction between acetone and the chemisorbed oxygen species on the surface of the sensor using dry-air as both carrier gas and for dilution. As mentioned before, the electrical current is very small, characteristic of very

high resistance in air, $\mathbf{R_{air} = 3.8 \times 10^9\ \Omega}$ and a typical of a semiconductor. The expectations are that there is greater band bending of the energy diagram in air and higher concentration of O^- species layer on the surface of the semiconductor. However, during the acetone chemical sensing the resistance reduces significantly by two orders of magnitude to, $\mathbf{R_{gas} = 1.5\times 10^7\ \Omega}$.

It should be noted that ne^- represents the number of electrons available in the conduction band. During the acetone sensing, these electrons' population is increased by a factor, *m*. **Fig. 5.26 (c and d)** exhibits similar processes described earlier of the redox reaction now using inert gas (argon) to create an oxygen deficient environment. Now, the processes described by **Eqs. 5.16** to **5.20** are greatly compromised. The depletion layer is small and lower potential barrier. Allowing acetone inside the chamber will lead to insignificant chemical reaction between the least available chemisorbed oxygen species and the gas. In this case, the released electrons' population by a factor l is minimised due to the nature of environment, inert ambient. The factor l < *m*,The electrical resistance ($\mathbf{R_{Ar} = 4.0 \times 10^6\ \Omega}$) in argon decreased as compared to dry-air ($\mathbf{R_{air} = 3.8 \times 10^9\ \Omega}$). This suggests a characteristic of a metal or towards a metallic behaviour. The resistance in the presence of acetone is $\mathbf{R_{Ar} = 2.8 \times 10^5\ \Omega}$. Hence, the response in the presence of acetone was low as compared to when dry-air was used. The number of electrons transferred back to the $MgCe_{0.2}Fe_{1.8}O_4$ sensor is less when using argon as compared to dry-air. This is simply because of the low adsorption–desorption kinetics. The presence of argon or inert gas discourages the process described in **Eq. 5.20**. The order of the resistance in dry-air to acetone and to argon is $R_{air} > R_{acet\text{-}dryair} > R_{Ar} > R_{acet\text{-}Ar}$. It is incomprehensible that the resistances in the presence of acetone followed the dry-air and argon, respectively, are not the same, $R_{acet\text{-}dryair} > R_{acet\text{-}Ar}$. One would expect them to be approximately equal because they are both in the presence of the gas analyte. This, therefore, suggests that the process leading to the gas exposure is important for how the sensor will behave in the presence of a gas analyte.

The Magnesium-Cerium doped nanoferrites sensor was also tested on LPG at 225℃, hence the dominant chemisorbed oxygen species were $O_{(ads)}^-$ as described in **Eq. 5.16** to **Eq. 5.19.** When

the LPG is introduced into the chamber, the reducing gas reacts with the adsorbed oxygen species (anions), a complex series of reactions take place, ultimately oxidising the LPG gas according to the following equations:

$$C_nH_{2n+2} + O_2^- \xrightarrow{@225℃} C_nH_{2n}{:}O_{2(gas)} + e^- + H_2O_{ads} \rightarrow CO_{2gas} + H_2O_{gas/moisture} \quad \text{Eq.....5. 21}$$

$$C_3H_8 + 5O_2^- \xrightarrow{n=3} 3CO_{2gas} + 4H_2O_{gas} + 5e^- \quad \text{Eq.....5. 22}$$

$$C_4H_{10} + {}^{13}/_{2}\, O_2^- \xrightarrow{n=4} 4CO_{2gas} + 5H_2O_{gas/moisture} + {}^{13}/_{2}\, e^- \quad \text{Eq.....5. 23}$$

The LPG is mainly composed of both propane and butane, hence, C_nH_{2n+2} is a fair representative of the gas compositions, where *n* is the number of elements and can take any integer. The number of element(*n*) is 3 and 4 in this case for propane and butane respectively. These reactions **(Eqs (5.21), (5.22), (5.23))** release a large population of free electrons, increasing the negative charge carriers on the surface.

5. 6. REFERENCES

[1] Hai-Jun Zhang, Li-Zhu Liu, Xiao-Rui Zhang, Shuang Zhang, F.-N. Meng, Microwave-assisted solvothermal synthesis of shape-controlled CoFe2O4 nanoparticles for acetone sensor., Journal of Alloys and Compounds 788 (2019) 1103-1112.

[2] N. Tammanoon, A. Wisitsoraat, D. Phokharatkul, A. Tuantranont, S. Phanichphant, V. Yordsri, C. Liewhiran, Highly sensitive acetone sensors based on flame-spray-made La2O3-doped SnO2 nanoparticulate thick films, Sensors and Actuators B: Chemical 262 (2018) 245-262.

[3] Run Zhang, Yan Wang, Zhanying Zhang, J. Cao, Highly Sensitive Acetone Gas Sensor Based on g-C3N4 Decorated MgFe2O4 Porous Microspheres Composites., Sensors 18 (2018) 2211.

[4] N. Van Hoang, C.M. Hung, N.D. Hoa, N. Van Duy, I. Park, N. Van Hieu, Excellent detection of H2S gas at ppb concentrations using ZnFe2O4 nanofibers loaded with reduced graphene oxide, Sensors and Actuators B: Chemical 282 (2019) 876-884.

[5] X. Liu, J. Hu, B. Cheng, H. Qin, M. Jiang, Acetone gas sensing properties of SmFe1−xMgxO3 perovskite oxides, Sensors and Actuators B: Chemical 134 (2008) 483-487.

[6] M. Yang, L. Huo, H. Zhao, S. Gao, Z. Rong, Electrical properties and acetone-sensing characteristics of LaNi1−xTixO3 perovskite system prepared by amorphous citrate decomposition, Sensors and Actuators B: Chemical 143 (2009) 111-118.

[7] N.N. Shozi, I. Kortidis, P.S. Mkwae, N.P. Chonco, N. Leshabane, M. Jozela, R.E. Kroon, H.C. Swart, S.S. Nkosi, Extremely sensitive and selective flammable liquefied hydrocarbon gas sensing and inter-dependence of fluctuating operating temperature and resistance: Perspective of rare-earth doped cobalt nanoferrites, Journal of Alloys and Compounds 859 (2021).pages?

[8] T.P. Mokoena, K.T. Hillie, H.C. Swart, N. Leshabane, J. Tshilongo, D.E. Motaung, Fabrication of a propanol gas sensor using p-type nickel oxide nanostructures: The effect of

ramping rate towards luminescence and gas sensing characteristics, Materials Chemistry and Physics 253 (2020).pages?

[9] J.-H. Kim, J.-H. Lee, Y. Park, J.-Y. Kim, A. Mirzaei, H.W. Kim, S.S. Kim, Toluene- and benzene-selective gas sensors based on Pt- and Pd-functionalized ZnO nanowires in self-heating mode, Sensors and Actuators B: Chemical 294 (2019) 78-88.

[10] P.S. Mkwae, I. Kortidis, R.E. Kroon, N. Leshabane, M. Jozela, H.C. Swart, S.S. Nkosi, Insightful acetone gas sensing behaviour of Ce substituted MgFe2O4 spinel nano-ferrites, Journal of Materials Research and Technology 9 (2020) 16252-16269.

[11] S. Deepapriya, S.L. Devi, P.A. Vinosha, J.D. Rodney, C.J. Raj, J.E. Jose, S.J. Das, Estimating the ionicity of an inverse spinel ferrite and the cation distribution of La-doped NiFe2O4 nanocrystals for gas sensing properties, Applied Physics A 125 (2019).pages?

[12] Sonam Chakraborty, M. Pal, Highly selective and stable acetone sensor based on chemically prepared bismuth ferrite nanoparticles., Journal of Alloys and Compounds 787 (2019) 1204-1211. Check the original title.

[13] X.-F. Wang, W. Ma, F. Jiang, E.-S. Cao, K.-M. Sun, L. Cheng, X.-Z. Song, Prussian Blue analogue derived porous NiFe2O4 nanocubes for low-concentration acetone sensing at low working temperature, Chemical Engineering Journal 338 (2018) 504-512.

[14] Y. Zhang, H. Xu, S. Dong, R. Han, X. Liu, Y. Wang, S. Li, Q. Bu, X. Li, J. Xiang, A fast response & recovery acetone gas sensor based on BiFeO3 nanomaterials with high sensitivity and low detection limit, Journal of Materials Science: Materials in Electronics 29 (2017) 2193-2200.

[15] Panpan Zhang, W.L. Hongwei Qin, Heng Zhang, Jifan Hu, Gas sensors based on ytterbium ferrites nanocrystalline powders for detecting acetone with low concentrations, Sensors and Actuators B 246 (2017) 9-19.

[16] M. Karmakar, P. Das, M. Pal, B. Mondal, S.B. Majumder, K. Mukherjee, Acetone and ethanol sensing characteristics of magnesium zinc ferrite nano-particulate chemi-resistive sensor, Journal of Materials Science 49 (2014) 5766-5771.

[17] N. Zahmouli, M. Hjiri, S.G. Leonardi, L. El Mir, G. Neri, D. Iannazzo, C. Espro, M.S. Aida, High performance Gd-doped γ-Fe2O3 based acetone sensor, Materials Science in Semiconductor Processing 116 (2020).pages?

[18] Y. Xu, Y. Fan, X. Tian, Q. Liang, X. Liu, Y. Sun, p-p heterojunction composite of NiFe2O4 nanoparticles-decorated NiO nanosheets for acetone gas detection, Materials Letters 270 (2020).pages?

[19] H. Zhang, H. Qin, P. Zhang, Y. Chen, J. Hu, Low concentration acetone gas sensing properties of 3 wt% Pd-doped SmCoxFe1-xO3 nanocrystalline powders under UV light illumination, Sensors and Actuators B: Chemical 260 (2018) 33-41.

[20] C. Su, C. Liu, L. Liu, M. Ni, H. Li, X. Bo, L. Liu, X. Chi, Excellent acetone sensing properties of Sm-doped α-Fe 2 O 3, Applied Surface Science 314 (2014) 931-935.

[21] H. Shan, C. Liu, L. Liu, S. Li, L. Wang, X. Zhang, X. Bo, X. Chi, Highly sensitive acetone sensors based on La-doped α-Fe2O3 nanotubes, Sensors and Actuators B: Chemical 184 (2013) 243-247.

[22] H. Zhang, H. Qin, P. Zhang, J. Hu, High Sensing Properties of 3 wt % Pd-Doped SmFe1-xMg xO3 Nanocrystalline Powders to Acetone Vapor with Ultralow Concentrations under Light Illumination, ACS Appl Matter Interfaces 10 (2018) 15558-15564.

[23] M. Šetka, F.A. Bahos, O. Chmela, D. Matatagui, I. Gràcia, J. Drbohlavová, S. Vallejos, Cadmium telluride/polypyrrole nanocomposite based Love wave sensors highly sensitive to acetone at room temperature, Sensors and Actuators B: Chemical 321 (2020).pages?

[24] L. Lv, Y. Wang, P. Cheng, B. Zhang, F. Dang, L. Xu, Ultrasonic spray pyrolysis synthesis of three-dimensional ZnFe2O4-based macroporous spheres for excellent sensitive acetone gas sensor, Sensors and Actuators B: Chemical 297 (2019).pages?

[25] K.M. Zhu, S.Y. Ma, S.T. Pei, Y. Tie, Q.X. Zhang, W.Q. Wang, X.L. Xu, Preparation, characterizaton and formaldehyde gas sensing properties of walnut-shaped BiFeO3 microspheres, Materials Letters 246 (2019) 107-110.

[26] P. Tarttelin Hernández, M.V. Kuznetsov, I.G. Morozov, I.P. Parkin, Application of levitation-jet synthesized nickel-based nanoparticles for gas sensing, Materials Science and Engineering: B 244 (2019) 81-92.

[27] Chao Zhang, Qingdan Wu, Bingbing Zheng, Jiajun You, Y. Luo, Synthesis and acetone gas sensing properties of Ag activated hollow sphere structured ZnFe2O4., Ceramic International 44 (2018) 20700-20707.

[28] S.D. Raut, V.V. Awasarmol, B.G. Ghule, S.F. Shaikh, S.K. Gore, R.P. Sharma, P.P. Pawar, R.S. Mane, Enhancement in room-temperature ammonia sensor activity of size-reduced cobalt ferrite nanoparticles on γ-irradiation, Materials Research Express 5 (2018).pages?

[29] C. Zhao, W. Lan, H. Gong, J. Bai, R. Ramachandran, S. Liu, F. Wang, Highly sensitive acetone-sensing properties of Pt-decorated CuFe2O4 nanotubes prepared by electrospinning, Ceramics International 44 (2018) 2856-2863.

[30] Y. Ma, Y. Lu, H. Gou, W. Zhang, S. Yan, X. Xu, Octahedral NiFe2O4 for high-performance gas sensor with low working temperature, Ceramics International 44 (2018) 2620-2625.

[31] T. Zhou, T. Zhang, Y. Zeng, R. Zhang, Z. Lou, J. Deng, L. Wang, Structure-driven efficient NiFe2O4 materials for ultra-fast response electronic sensing platform, Sensors and Actuators B: Chemical 255 (2018) 1436-1444.

[32] L. Ma, S.Y. Ma, X.F. Shen, T.T. Wang, X.H. Jiang, Q. Chen, Z. Qiang, H.M. Yang, H. Chen, PrFeO3 hollow nanofibers as a highly efficient gas sensor for acetone detection, Sensors and Actuators B: Chemical 255 (2018) 2546-2554.

[33] J. You, X. Chen, B. Zheng, X. Geng, C. Zhang, Suspension Plasma-Sprayed ZnFe2O4 Nanostructured Coatings for ppm-Level Acetone Detection, Journal of Thermal Spray Technology 26 (2017) 728-734.

[34] Hamid Reza Ebrahimi, Mohammad Parish, Gholam Reza Amiri, Behzad Bahraminejad, S. Fatahian, Synthesis, characterization and gas sensitivity investigation of Ni0.5Zn0.5Fe2O4 nanoparticles., Journal of Magnetism and Magnetic Material 44 (2016) 55-58.

[35] S. Sen, P. Anand, M. Narjinary, S.K.M. Mursalin, R. Manna, Ethanol sensing evaluation of sol–gel barium calcium ferrite, Ceramics International 42 (2016) 12581-12585.

[36] J. Zhang, J.-M. Song, H.-L. Niu, C.-J. Mao, S.-Y. Zhang, Y.-H. Shen, ZnFe2O4 nanoparticles: Synthesis, characterization, and enhanced gas sensing property for acetone, Sensors and Actuators B: Chemical 221 (2015) 55-62.

[37] M. Maharajan, M.D. Mursalin, M. Narjinary, P. Rana, S. Sen, A. Sen, Synthesis, Characterization and Vapour Sensing Properties of Nanosized ZnFe2O4, Transactions of the Indian Ceramic Society 73 (2014) 102-104.

[38] M. Karmakar, B. Mondal, M. Pal, K. Mukherjee, Acetone and ethanol sensing of barium hexaferrite particles: A case study considering the possibilities of non-conventional hexaferrite sensor, Sensors and Actuators B: Chemical 190 (2014) 627-633.

[39] M.S. Khandekar, N.L. Tarwal, J.Y. Patil, F.I. Shaikh, I.S. Mulla, S.S. Suryavanshi, Liquefied petroleum gas sensing performance of cerium doped copper ferrite, Ceramics International 39 (2013) 5901-5907.

[40] J.Y. Patil, I.S. Mulla, S.S. Suryavanshi, Gas response properties of citrate gel synthesized nanocrystalline MgFe2O4: Effect of sintering temperature, Materials Research Bulletin 48 (2013) 778-784.

[41] N. Rezlescu, E. Rezlescu, F. Tudorache, P.D. Popa, Gas sensing properties of porous cu-, cd- and zn- ferrites, Romanian Reports in Physics 61 (2009) 223-234.

[42] G. Zhang, C. Li, F. Cheng, J. Chen, ZnFe2O4 tubes: Synthesis and application to gas sensors with high sensitivity and low-energy consumption, Sensors and Actuators B: Chemical 120 (2007) 403-410.

[43] X. Liu, H. Ji, Y. Gu, M. Xu, Preparation and acetone sensitive characteristics of nano-LaFeO3 semiconductor thin films by polymerization complex method, Materials Science and Engineering: B 133 (2006) 98-101.

[44] Z. Zhang, Z. Wen, Z. Ye, L. Zhu, Gas sensors based on ultrathin porous Co3O4 nanosheets to detect acetone at low temperature, RSC Advances 5 (2015) 59976-59982.

[45] T. Chen, Z. Zhou, Y. Wang, Surfactant CATB-assisted generation and gas-sensing characteristics of LnFeO3 (Ln=La, Sm, Eu) materials, Sensors and Actuators B: Chemical 143 (2009) 124-131.

[46] L. Zhang, H. Qin, P. Song, J. Hu, M. Jiang, Electric properties and acetone-sensing characteristics of La1−xPbxFeO3 perovskite system, Materials Chemistry and Physics 98 (2006) 358-362.

[47] Z. Wang, K. Zhang, T. Fei, F. Gu, D. Han, α-Fe2O3/NiO heterojunction nanorods with enhanced gas sensing performance for acetone, Sensors and Actuators B: Chemical 318 (2020).

[48] X. Kou, F. Meng, K. Chen, T. Wang, P. Sun, F. Liu, X. Yan, Y. Sun, F. Liu, K. Shimanoe, G. Lu, High-performance acetone gas sensor based on Ru-doped SnO2 nanofibers, Sensors and Actuators B: Chemical 320 (2020).pages?

[49] B. Sharma, A.A. Kadam, J.-S. Sung, J.-h. Myung, Surface tuning of halloysite nanotubes with Fe3O4 and 3-D MnO2 nanoflakes for highly selective and sensitive acetone gas sensing, Ceramics International 46 (2020) 21292-21303.

[50] A.B. Mugutkar, S.K. Gore, R.S. Mane, S.M. Patange, S.S. Jadhav, S.F. Shaikh, A.M. Al-Enizi, A. Nafady, B.M. Thamer, M. Ubaidullah, Structural modifications in Co–Zn nanoferrites by Gd substitution triggering to dielectric and gas sensing applications, Journal of Alloys and Compounds 844 (2020) 156178.

[51] L. Van Duy, N. Van Duy, C.M. Hung, N.D. Hoa, N.Q. Dich, Urea mediated synthesis and acetone-sensing properties of ultrathin porous ZnO nanoplates, Materials Today Communications 25 (2020) 101445.

[52] C. Srinivas, E. Ranjith Kumar, B.V. Tirupanyam, S. Singh Meena, P. Bhatt, C.L. Prajapat, T.V. Chandrasekhar Rao, D.L. Sastry, Study of magnetic behavior in co-precipitated Ni–Zn ferrite nanoparticles and their potential use for gas sensor applications, Journal of Magnetism and Magnetic Materials 502 (2020).pages?

[53] P. Durga Prasad, J. Hemalatha, Enhanced magnetic properties of highly crystalline cobalt ferrite fibers and their application as gas sensors, Journal of Magnetism and Magnetic Materials 484 (2019) 225-233.

[54] C. Mukherjee, R. Mondal, S. Dey, S. Kumar, J. Das, Nanocrystalline CopperNickelZinc Ferrite: Efficient Sensing Materials for Ethanol and Acetone at Room Temperature, IEEE Sensors Journal 17 (2017) 2662-2669.

[55] R. Sahoo, S. Santra, C. Ray, A. Pal, Y. Negishi, S.K. Ray, T. Pal, Hierarchical growth of ZnFe2O4 for sensing applications, New J. Chem. 40 (2016) 1861-1871.

[56] Y. Zohrabi, M. E. Ghazi, M. Izadifard, The Gas-Sensing Properties of Ni-Zn Ferrite (Ni0:6Zn0:4Fe2O4) Nanoparticles Prepared by the Microwave Method, Chinese Journal of Physics 53 (2015).pages?

[57] J.Y. Patil, D.Y. Nadargi, J.L. Gurav, I.S. Mulla, S.S. Suryavanshi, Glycine combusted ZnFe2O4 gas sensor: Evaluation of structural, morphological and gas response properties, Ceramics International 40 (2014) 10607-10613.

[58] A. Sutka, R. Pärna, G. Mezinskis, V. Kisand, Effects of Co ion addition and annealing conditions on nickel ferrite gas response, Sensors and Actuators B: Chemical 192 (2014) 173-180.

[59] M.S. Khandekar, N.L. Tarwal, I.S. Mulla, S.S. Suryavanshi, Nanocrystalline Ce doped CoFe2O4 as an acetone gas sensor, Ceramics International 40 (2014) 447-452.

[60] Y. Köseoğlu, İ. Aldemir, F. Bayansal, S. Kahraman, H.A. Çetinkara, Synthesis, characterization and humidity sensing properties of Mn0.2Ni0.8Fe2O4 nanoparticles, Materials Chemistry and Physics 139 (2013) 789-793.

[61] S.S. Karpova, V.A. Moshnikov, S.V. Mjakin, E.S. Kolovangina, Surface functional composition and sensor properties of ZnO, Fe2O3, and ZnFe2O4, Semiconductors 47 (2013) 392-395.

[62] W.-l. Jiao, L. Zhang, Preparation and gas sensing properties for acetone of amorphous Ag modified NiFe2O4 sensor, Transactions of Nonferrous Metals Society of China 22 (2012) 1127-1132.

[63] Z. Sun, L. Liu, D.z. Jia, W. Pan, Simple synthesis of CuFe2O4 nanoparticles as gas-sensing materials, Sensors and Actuators B: Chemical 125 (2007) 144-148.

[64] N. Rezlescu, N. Iftimie, E. Rezlescu, C. Doroftei, P.D. Popa, Semiconducting gas sensor for acetone based on the fine grained nickel ferrite, Sensors and Actuators B: Chemical 114 (2006) 427-432.

[65] P. Song, H. Zhang, D. Han, J. Li, Z. Yang, Q. Wang, Preparation of biomorphic porous LaFeO3 by sorghum straw biotemplate method and its acetone sensing properties, Sensors and Actuators B: Chemical 196 (2014) 140-146.

[66] K. Fan, H. Qin, Z. Zhang, L. Sun, L. Sun, J. Hu, Gas sensing properties of nanocrystalline La0.75Ba0.25FeO3 thick-film sensors, Sensors and Actuators B: Chemical 171-172 (2012) 302-308.

[67] Z.-l. Wu, R. Zhang, M. Zhao, S.-m. Fang, Z.-x. Han, J.-f. Hu, K.-y. Wang, Effect of Pd doping on the acetone-sensing properties of NdFeO3, International Journal of Minerals, Metallurgy, and Materials 19 (2012) 141-145.

[68] S.S. Nkosi, I. Kortidis, D.E. Motaung, R.E. Kroon, N. Leshabane, J. Tshilongo, O.M. Ndwandwe, The effect of stabilized ZnO nanostructures green luminescence towards LPG sensing capabilities, Materials Chemistry and Physics 242 (2020).pages?

[69] S.W. Gumbi, P.S. Mkwae, I. Kortidis, R.E. Kroon, H.C. Swart, T. Moyo, S.S. Nkosi, Electronic and Simple Oscillatory Conduction in Ferrite Gas Sensors: Gas-Sensing Mechanisms, Long-Term Gas Monitoring, Heat Transfer, and Other Anomalies, ACS Applied Materials & Interfaces 12 (2020) 43231-43249.

[70] C. Xu, J. Tamaki, N. Miura, N. Yamazoe, Grain size effects on gas sensitivity of porous SnO2-based elements, Sensors and Actuators B: Chemical 3 (1991) 147-155.

[71] P. Rai, W.-K. Kwak, Y.-T. Yu, Solvothermal Synthesis of ZnO Nanostructures and Their Morphology-Dependent Gas-Sensing Properties, ACS Applied Materials & Interfaces 5 (2013) 3026-3032.

[72] W.-Y. Yan, Q. Zhou, X. Chen, X.-J. Huang, Y.-C. Wu, C-doped and N-doped reduced graphene oxide/TiO2 composites with exposed (001) and (101) facets controllably synthesized by a hydrothermal route and their gas sensing characteristics, Sensors and Actuators B: Chemical 230 (2016) 761-772.

[73] K. Anand, J. Kaur, R.C. Singh, R. Thangaraj, Preparation and characterization of Ag-doped In2O3 nanoparticles gas sensor, Chemical Physics Letters 682 (2017) 140-146.

[74] V. Saasa, Y. Lemmer, T. Malwela, A. Akande, M. Beukes, B. Mwakikunga, Effect of varying ethanol and water compositions on the acetone sensing properties of WO₃ for application in diabetes mellitus monitoring, Materials Research Express 7 (2020) 035905.

[75] J. Walker, P. Karnati, D.R. Miller, M. Al-Hashem, S.A. Akbar, P.A. Morris, A new open-access online database for resistive-type gas sensor properties and performance, Sensors and Actuators B: Chemical 321 (2020) 128591.

[76] Z.P. Tshabalala, H.C. Swart, D.E. Motaung, Fabrication of TiO2 nanofibers based sensors for enhanced CH4 performance induced by notable surface area and acid treatment, Vacuum 187 (2021) 110102.

[77] V.B. Kamble, A.M. Umarji, Effect of Pt doping on the gas sensing properties of porous chromium oxide films through a kinetic response analysis approach, RSC Advances 5 (2015) 27509-27516.

[78] V. Manikandan, M. Singh, B.C. Yadav, R.S. Mane, S. Vigneselvan, A. Mirzaei, J. Chandrasekaran, Room temperature LPG sensing properties of tin substituted copper ferrite (Sn−CuFe2O4) thin film, Materials Chemistry and Physics 240 (2020).pages?

[79] A. Singh, A. Singh, S. Singh, P. Tandon, B.C. Yadav, Preparation and characterization of nanocrystalline nickel ferrite thin films for development of a gas sensor at room temperature, Journal of Materials Science: Materials in Electronics 27 (2016) 8047-8054.

[80] A. Singh, A. Singh, S. Singh, P. Tandon, R.R. Yadav, Synthesis, Characterization and Gas Sensing Capability of NixCu1−xFe2O4 ($0.0 \leq x \leq 0.8$) Nanostructures Prepared via Sol–Gel Method, Journal of Inorganic and Organometallic Polymers and Materials 26 (2016) 1392-1403.

[81] P.S. Mkwae, S.A. Ogundipe, M. Jozela, N. Revaprasadu, S.S. Nkosi, The heat rate kinetics on the liquefied hydrocarbon gases sensing and food quality control detecting strategy, Materials Chemistry and Physics 277 (2022) 125550. Please check the original. This is not grammatical.

[82] A. Mirzaei, S.G. Leonardi, G. Neri, Detection of hazardous volatile organic compounds (VOCs) by metal oxide nanostructures-based gas sensors, Ceramic International 42 (2016) 15119-15141.

CHAPTER 6

POSSIBLE APPLICATION OF $MGCE_XFE_{2-X}O_4$ NANOFERRITES IN THE HEALTH AND FOOD INDUSTRIES

6.1 INTRODUCTION

This chapter explores the possible application of Magnesium-Cerium doped nanoferrites in the health and food industries. It has been established that in people suffering from diseases such as lung cancer, diabetes, and intestinal diseases, their breath tends to consist of gases like toluene, acetone, and hydrogen or methane respectively **[1]**. A similar thing happens to plants, when they are ready for harvesting a certain gas is released in abundance.

6.2 POSSIBLE APPLICATION IN BIOMARKERS

An innovative and promising way of assessing diabetic humans is analysis of the acetone concentration in their breath using a rapid chemoresistive sensor **[2-4]**. **Fig 6.1** shows different gases that are released by patients suffering from different diseases. The presence of acetone can indicate the ketotic state of diabetes relating to the levels of lipolysis by which fats are broken down **[3, 4]**. Insulin-patients have ketosis and will thereby release higher concentrations of acetone of more than 1.8 ppm in their breath **[3]**, whereas healthy human breath contains an acetone concentration of about 0.9 ppm **[5-7]**. However, human breath also contains relative high humidity, i.e., 90 % or more **[6, 7]**. This opens up the opportunity to fabricate extremely sensitive chemoresistive gas sensors for potential application for diabetes and other illnesses to detect volatile organic compounds (VOCs) like acetone, but also requiring selectivity to the

target. The currently available techniques of breath analysis require analytical instruments which are cumbersome, expensive, and generally only available in laboratories. Of the many acetone-based sensors, spinel ferrites present great promise and potential for use in the medical field to detect low levels of acetone. Acetone is a toxic and harmful VOC commonly used as a solvent in various laboratories and industries. Its high level of inhalation and ingestion can cause low, acute, and chronic poisoning **[2, 3]**. This therefore suggests that it is one of the most important air pollutants that require constant detection and monitoring **[2-4]** as part of routine rapid air quality testing.

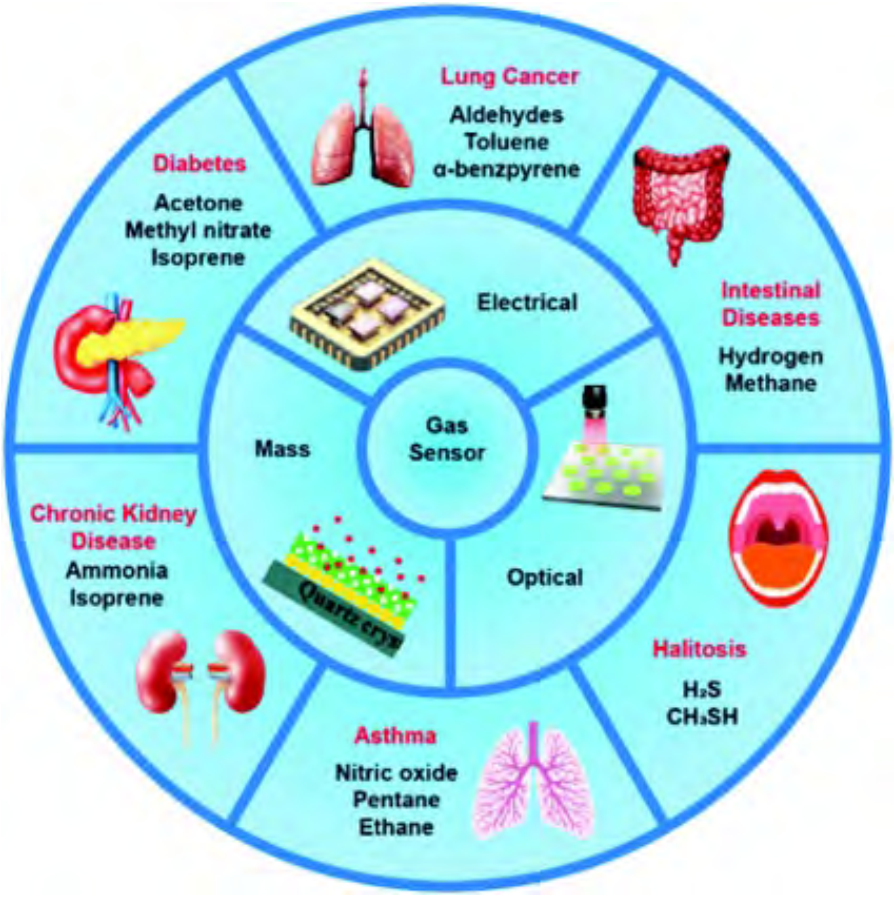

Figure 6. 1: Illustration of gases exhaled due to certain diseases**[1]**.

To mimic the actual scenarios of exhaled biomarkers for diabetic patients and reproducibility, the potential sensor was tested at lower acetone concentrations and in the presence of relative humidity. The Ce-doped magnesium based ferrite was tested for five cycles of 5 ppm acetone

at 225 °C operating temperature in a dry environment, in the presence of relative humidity (RH), and again in a dry environment.

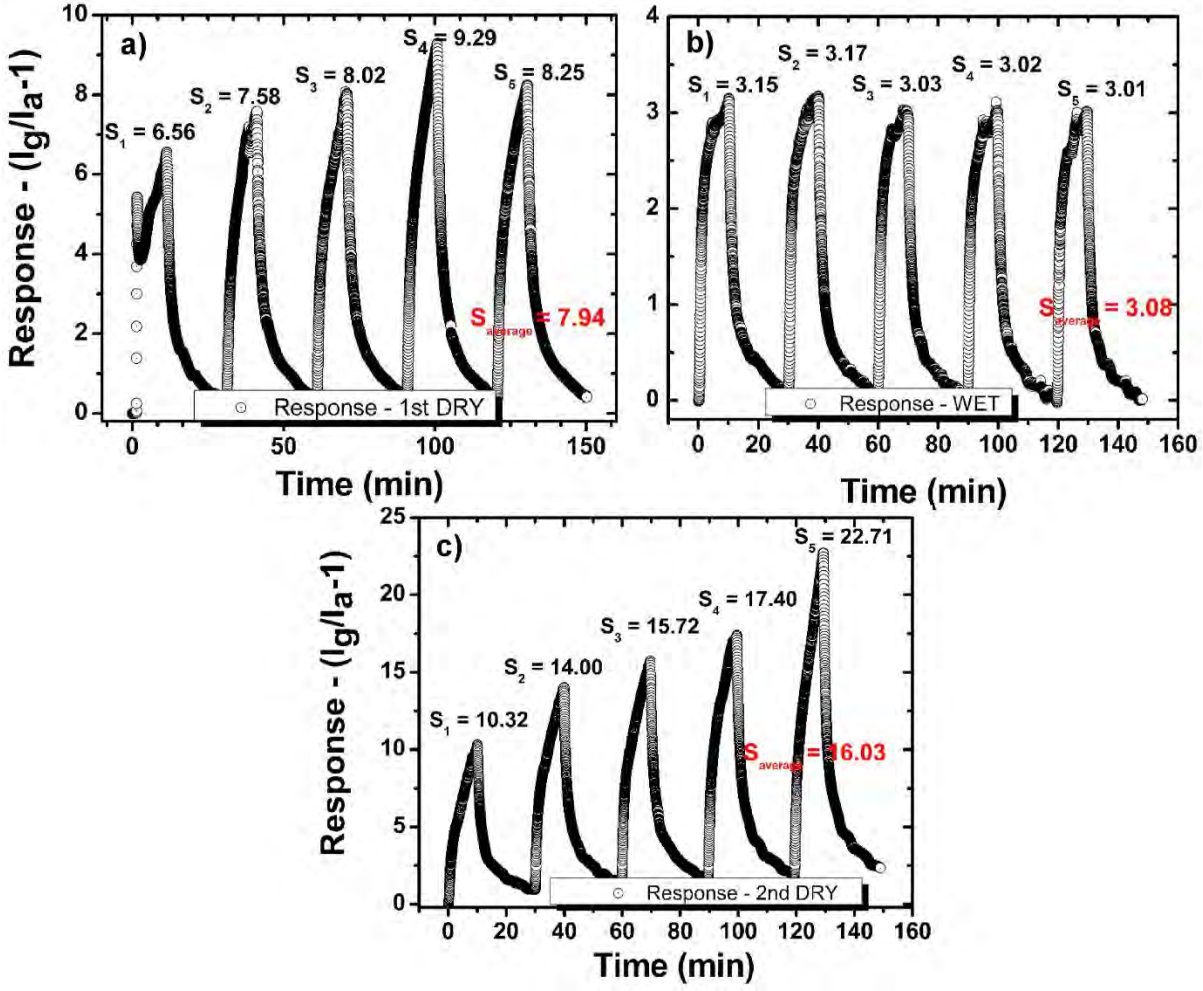

Figure 6. 2: (a) The five cycles of 5 ppm of acetone at 225 °C in dry-air of the $MgCe_{0.2}Fe_{1.8}O_4$, **(b)** in the presence of 20% RH (set RH was 90% at 225 °C), and **(c)** again in dry-air.

Fig. 6.2 (a–c) demonstrates the repeatability of 5 ppm concentration in dry environment, 20% relative humidity and again in dry environment to test the sensor's initial memory after having been exposed to the humidity. It can be seen that the sensor recorded a varying response to the same concentration (5 ppm) of acetone as shown in **Fig. 6.2(a)** but average to S = 7.9. The set RH was 90% at 225 °C. The achievable relative humidity was 20% RH due to the high operating temperature of 225 °C. **Fig. 6.2(b)** shows the five cycles of 5 ppm concentration of acetone in the presence of the relative humidity. The sensor's response still shows small

variation, averaging to S = 3.1. This clearly suggests that the presence of the 20% RH destroyed the response. This further suggests that acetone sensing is based on the chemically adsorbed oxygen species on the sensor's surface. Now that, we introduce the relative humidity which consists of hydroxylic group physically attaching to the surface and competing with the chemisorbed oxygen species, leaving fewer active sites **[8, 9]**. It is very interesting to observe that the reproducibility after the sensor was exposed to 20% RH was surprisingly changing as shown in **Fig. 6.2(c)**. The reproducibility of five (5) cycles of 5 ppm concentration of acetone contain ascending order of the response of 10.2, 14.0, 15.7, 17.4, and 22.7. It is clear that the exposure of the sensor to the relative humidity somehow re-invigorated the surfaces to become more active sites. The response on the 2nd dry-air was relatively high (about double) and showing increasing trend This shows possible application in diabetes biomarkers, although achieving high humidity of about 90% is still a challenge, so further studies need to be done.

6.3 FOOD QUALITY SENSING STRATEGY: PRELIMINARY WORK

Many indicators point to the fact that ethylene (C_2H_4) gas in plant or fruit hormone is given off by harvested plants and climacteric fruits during ripening **[10-13]**. Therefore, ethylene concentration during plant growth and soon after harvesting, provides critical information to control the growth and development of plant and fruit formation. Such information is indispensable to smart farming and profit maximisation for farmers.

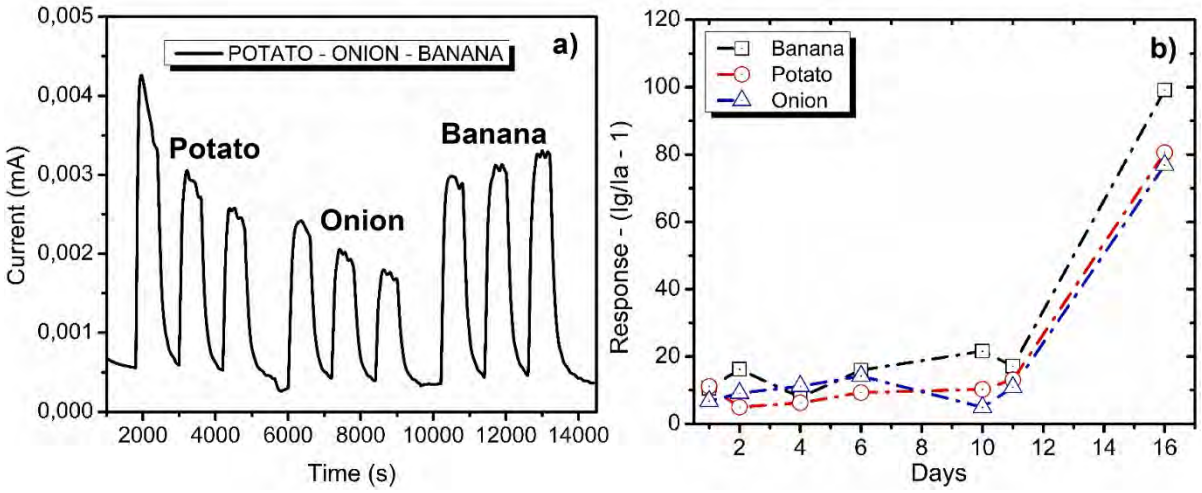

Figure 6. 3: Gas sensing characteristics of $MgFe_2O_4$ operated at 220 °C towards potato and onion (vegetables) and banana (fruit) each measured for **(a)** 3 cycles of 10 min. **(b)** Plants and climacteric fruit and their corresponding responses.

Fig. 6.3 shows the gas sensing measurements of a potato, onion and banana measured on different days to evaluate $MgFe_2O_4$ potential to examine plant and fruit freshness. It is expected that emitted ethylene odour will increase in concentration as these plants and fruits undergo a process of ripening. Prior to the sensing measurements, these vegetables and fruit were stored at room temperature (21°C) in open air with relative humidity of about 40% without any treatment. The banana ripening could be monitored and measured by observing the change in its peel colour during the maturation process, but the potato and onion maintained their initial colour for more than 15 days. Each vegetable (110 g) and fruit (100 g) were kept for 10 min at different times in a stainless steel chamber with dimensions of 25 cm by 30 cm by 26 cm. In each measurement, dry-air was introduced inside the sensing chamber until a stable electric current was maintained before connecting the separate stainless steel chamber to the sensing chamber through the dry-air to push the odour into the sensing chamber. Upon introducing the fruit and vegetable odour (separately) inside the sensing chamber, the sensor's current increased dramatically, as shown in **Fig. 6.3(a)** and dropped to its original value when the odour inlet was closed. It is clear from this figure (**Fig. 6.3a**) that, the response- and recovery-times are short, indicating a good sensing performance toward plant-hormone ethylene. The time-dependent

responses of the selected vegetables and fruit are shown in **Fig. 6.3(b)**. Initial responses to this plant hormone ethylene were: 11.59, 6.73 and 10.59 for a potato, anonion, and a banana, respectively. The sudden increase in the banana's response due to increased ethylene concentration after 14 days was expected. Banana can be physiologically categorised as a climacteric fruit and its ethylene emission increases significantly during natural ripening **[14-16]**. Besides, other studies on ethylene claimed that this rate of increase of ethylene production is in fact logarithmic **[17, 18]**.

The increase in electric current during exposure to banana was not unexpected, as it is obvious that an increasing concentration of plant-hormone ethylene is given off during banana maturation and ripening **[10]**. However, the cause of the increase in the electric current due to exposure of the n-type sensor to potato and onion odour was not clearly understood, but it was clear that the gas emitted from these vegetables was also a reducing analyte i.e., ethylene. However, there is evidence that these plants, either non-climacteric or climacteric, undergo similar pathways in ambient atmospheres during their growth **[15, 19]**. In fact, Paul et al. **[12]** claimed that there are no distinctions between the classical patterns of ripening in climacteric and non-climacteric fruit. Therefore, the assumption would be that the same gas is emitted in potato and onion and they both undergo similar pathways of ripening as in the climacteric fruit (in this case, banana). The gas concentrations were not known in these cases, but in all cases these concentrations increased during these plants' growth processes i.e., cell division, cell enlargement, ripening and senescence **[15]**.

It was noticed that the electric current cycles resulting from ethylene detection in the vegetables showed a descending order from 1st to 3rd cycle, whereas it was an ascending order in the case of the banana. These orders were maintained in all the measurements for days. Therefore, this preliminary work presents the possibility that ferrites can be used to determine plants' freshness. It is often the case that people choose fruit based on the colour, scent, gloss, and hardness. However, other fruit such as the non-climacteric Citrus fruit, berries, grapes, and

pineapples) do not show significant colour change during their respiration. They quietly undergo a ripening or maturation process instead. Another example is a potato that undergoes a change in respiration rate during growth. A potato often damages other potatoes in a bag once it starts to deteriorate in an ambient atmosphere. This can be avoided using quantitative measurements of ethylene to facilitate high-quality plant selection.

6.4 REFERENCES

[1] X. Zhou, Z. Xue, X. Chen, C. Huang, W. Bai, Z. Lu, T. Wang, Nanomaterial-based gas sensors used for breath diagnosis, Journal of Materials Chemistry B 8 (2020) 3231-3248.

[2] A. Mirzaei, S.G. Leonardi, G. Neri, Detection of hazardous volatile organic compounds (VOCs) by metal oxide nanostructures-based gas sensors., Ceramic International 42 (2016) 15119-15141.

[3] N. Tammanoon, A. Wisitsoraat, D. Phokharatkul, A. Tuantranont, S. Phanichphant, V. Yordsri, C. Liewhiran, Highly sensitive acetone sensors based on flame-spray-made La2O3-doped SnO2 nanoparticulate thick films, Sensors and Actuators B: Chemical 262 (2018) 245-262.

[4] Run Zhang, Yan Wang, Zhanying Zhang, J. Cao, Highly Sensitive Acetone Gas Sensor Based on g-C3N4 Decorated MgFe2O4 Porous Microspheres Composites., Sensors 18 (2018).pages

[5] Chao Zhang, Qingdan Wu, Bingbing Zheng, Jiajun You, Y. Luo, Synthesis and acetone gas sensing properties of Ag activated hollow sphere structured ZnFe2O4., Ceramic International 44 (2018) 20700-20707.

[6] Sonam Chakraborty, M. Pal, Highly selective and stable acetone sensor based on chemically prepared bismuth ferrite nanoparticles., Journal of Alloys and Compounds 787 (2019) 1204-1211.

[7] Panpan Zhang, W.L. Hongwei Qin, Heng Zhang, Jifan Hu, Gas sensors based on ytterbium ferrites nanocrystalline powders for detecting acetone with low concentrations, Sensors and Actuators B 246 (2017) 9-19.

[8] N. Van Hoang, C.M. Hung, N.D. Hoa, N. Van Duy, I. Park, N. Van Hieu, Excellent detection of H2S gas at ppb concentrations using ZnFe2O4 nanofibers loaded with reduced graphene oxide, Sensors and Actuators B: Chemical 282 (2019) 876-884.

[9] F. Qu, N. Zhang, S. Zhang, R. Zhao, D. Yao, S. Ruan, M. Yang, Construction of Co3O4/CoWO4 core-shell urchin-like microspheres through ion-exchange method for high-performance acetone gas sensing performance, Sensors and Actuators B: Chemical 309 (2020) 127711.

[10] S.P. Burg, E.A. Burg, Molecular Requirements for the Biological Activity of Ethylene 1, Plant Physiology 42 (1967) 144-152.

[11] Y.-C. Han, J.-F. Kuang, J.-Y. Chen, X.-C. Liu, Y.-Y. Xiao, C.-C. Fu, J.-N. Wang, K.-Q. Wu, W.-J. Lu, Banana Transcription Factor MaERF11 Recruits Histone Deacetylase MaHDA1 and Represses the Expression of MaACO1 and Expansins during Fruit Ripening, Plant Physiology 171 (2016) 1070-1084.

[12] V. Paul, R. Pandey, G.C. Srivastava, The fading distinctions between classical patterns of ripening in climacteric and non-climacteric fruit and the ubiquity of ethylene—An overview, Journal of Food Science and Technology 49 (2012) 1-21.

[13] K.S. Varghese, M.C. Pandey, K. Radhakrishna, A.S. Bawa, Technology, applications and modelling of ohmic heating: a review, Journal of Food Science and Technology 51 (2014) 2304-2317.

[14] S.-Y. Jeong, Y.K. Moon, T.-H. Kim, S.-W. Park, K.B. Kim, Y.C. Kang, J.-H. Lee, A New Strategy for Detecting Plant Hormone Ethylene Using Oxide Semiconductor Chemiresistors: Exceptional Gas Selectivity and Response Tailored by Nanoscale Cr2O3 Catalytic Overlayer, Advanced Science 7 (2020) 1903093.

[15] S.P. Burg, E.A. Burg, Role of Ethylene in Fruit Ripening 12, Plant Physiology 37 (1962) 179-189.

[16] S.P. Burg, E.A. Burg, Relationship between Ethylene Production and Ripening in Bananas, Botanical Gazette 126 (1965) 200-204.

[17] C. Périn, M. Gomez-Jimenez, L. Hagen, C. Dogimont, J.-C. Pech, A. Latché, M. Pitrat, J.-M. Lelièvre, Molecular and Genetic Characterization of a Non-Climacteric Phenotype in

Melon Reveals Two Loci Conferring Altered Ethylene Response in Fruit, Plant Physiology 129 (2002) 300-309.

[18] R. Wills, W. McGlasson, D. Graham, D. Joyce, Physiology and biochemistry, Postharvest: An introduction to the physiology and handling of fruit, vegetables and ornamentals (2007) 28-51. Check this ref.

[19] C.S. Barry, J.J. Giovannoni, Ethylene and fruit ripening, Journal of Plant Growth Regulation 26 (2007) 143-159.

CHAPTER 7

CONCLUSION AND FUTURE WORK

In conclusion, we presented a successful synthesis of $MgCe_xFe_{2-x}O_4$ ($0 \leq x \leq 0.2$) by a glyco-thermal procedure. The effect of cerium substitution into the octahedral sites of the cubic magnesium ferrite was investigated, considering sensing of organic volatile compounds and magnetic properties. The HR-TEM images present fine nanoparticles with few crystallite sizes of between 2.2 – 15.3 nm. The XRD spectra confirmed the cubic spinel ferrite structure at low cerium concentration ($x < 0.2$) although the formation of secondary phases occurred when $x = 0.2$. The magnetic properties suggested superparamagnetic to disordered characteristics with the increase of Ce content. The variation of magnetic parameters such as saturation magnetisation as a function of Ce concentration were also reported. ^{57}Fe Mössbauer effect spectra showed a transformation from ordered to paramagnetic spin state with an increase in Ce concentration. The broad peaks in the spectrum of the $MgFe_2O_4$ powder changed to a well resolved Zeeman splitting with increasing Ce content. The XPS analysis revealed high percentages of oxygen vacancies attributed to the reduction of Fe^{3+} to Fe^{2+}, evident in the high-resolution of Fe 2p spin-orbits doublets. The nano-ferrites were tested over a range of VOCs including acetone, methanol, p-xylene, ethylbenzene, toluene, and benzene at a temperature of 225 °C. The formation of secondary phases seems to be favourable for gas sensing, with an extremely high acetone sensing response (**S = 529@100 ppm**) and selectivity. These Ce-doped magnesium ferrites had n-type characteristics. This high sensitivity and selectivity compared very well to other acetone sensors in the literature. Additionally, the Ce-doped magnesium sensor possessed reliable reproducibility, reversibility and remained highly sensitive even after

120 days. The various exposure-time testing for both the detection and monitoring qualified this sensor as suitable and reliable for both capabilities of high acetone response and to maintain this response over a long-time exposure to acetone. Furthermore, this sensor was tested in a reduced oxygen environment, using argon gas for dilution and as carrier gas. The responses were significantly reduced but possessed clear sensing signals with comparable response.

The addition of a relatively high content of Ce to the magnesium ferrite was favourable to high acetone sensitivity. Does the formation of secondary phases also favour sensing of flammable and toxic gases besides the VOCs? To answer the question, these magnesium ferrite sensors were tested towards different flammable gases, namely, ammonia, methane, propane, butane, hydrogen, and liquefied petroleum gas (LPG). The optimal operating temperature was 225 ◦C. The undoped magnesium ferrite ($MgFe_2O_4$) proved to be highly sensitive and selective to LPG with a response of S = 357.41. Some interesting patterns of anomaly were observed during the sensing of LPG. Oscillatory behaviour in the electric current, accompanied by a fluctuation of operating temperature in reverse order to the current was observed. These anomalies were attributed to heat transfer kinetics between the sensor's ($MgFe_2O_4$) surface and the physisorbed self-dissociated water molecules. We derived new mathematical expressions, following Fourier's conduction law, to explain these processes. This ends up with a direct connection between heat conduction and the sensor's electric current/resistance. To further test and attempt to control these two anomalies in the sensor's current and operating temperature, we created an oxygen reduced environment or inert ambient by using argon and nitrogen instead of the synthetic air or dry- air as a carrier gas and for dilution of the LPG. It has been shown that the use of argon instead of synthetic air to create a reduced oxygen environment or inert ambient eliminated these oscillatory behaviour and temperature fluctuations. However, using nitrogen instead of either synthetic air or argon did not eliminate these anomalies. In addition, creating inert ambient was observed to significantly reduce the sensor response, $S_{Air} \gg S_{argon} \approx S_{nitrogen}$. Temperature, concentration, and exposure-time seem to play a role in the control of these anomalies. Repeatability and stability of the sensors were also investigated. The sample was

also stable when exposed to LPG for a long exposure time. It clearly produced a stable steady-state current for up to 2 h. In addition to the investigated anomalies, we tested our $MgFe_2O_4$ sensor for 'off-shelf plants freshness' determination. The tested plants were climacteric fruit (banana) and vegetable (Potatoes and onion). The test was conducted for a period of 16 days. The interaction between our n-type sensor and the plants' hormone suggests that this emitted gas is a reducing type. This gas is believed to be ethylene, based on the literature. The unknown concentration of this emitted gas increased over a period of 16 days. This detection strategy provides a unique, precise, and quantitative means of controlling plant hormone during plants' developmental growth and will be beneficial for profit maximisation in agricultural sectors.

Besides the in-depth investigations carried out in this work, more fundamental questions that deserve further understanding still exist. What triggers these current oscillations and temperature fluctuations in the sensor surface? Is there any other way to control these fluctuations in temperature when losing or re-gaining the surface heat? How can we really explore these temperature fluctuations for better understanding of the gas sensing mechanism? What other gases trigger these anomalies? Could these anomalies be due to the type of sensor material? What is the role of other plant hormone interactions with ethylene? As future work the author will work towards answering the questions.